Università degli Studi di Roma
"Tor Vergata"

Facoltà di Scienze Matematiche, Fisiche e Naturali

Triple-GEM detectors for the innermost region of the muon apparatus at the LHCb experiment

Doctoral Thesis in Physics

Marco Poli Lener

Tutor

Dott. G. Bencivenni

Coordinator

Prof. P. Picozza

Roma 2005

”Eliminato l’impossibile,
quello che resta,
per quanto improbabile,
deve essere la verità.”

Arthur Conan Doyle

Contents

Abstract

The LHCb experiment will take place at the future LHC accelerator at CERN and will start in 2007. It is a single arm spectrometer dedicated to precision measurements of $\mathcal{CP}$ violation and rare decays in the b quark sector. Recent experimental results have shown that $\mathcal{CP}$ violation is large in this sector.
LHCb is designed with a robust and flexible trigger in order to extensively gain access to a wide spread of different physical processes involving the *beauty* particles. This will allow to over-constrain the Standard Model predictions about $\mathcal{CP}$ violation, and to discover any possible inconsistency, which would reveal the presence of "New Physics".
The work presented in this thesis has two main parts: the development of a charged particle detector based on Gas Electron Multiplication (GEM) and the study of luminosity measurements with the physical channels $Z^0 \rightarrow \mu^+\mu^-$ and $W^{\pm} \rightarrow \mu^{\pm}\nu$.

At the "Laboratori Nazionali di Frascati", in collaboration with a group of the "Università degli Studi di Cagliari", we developed a triple-GEM detector in order to equip the inner region (R1) of the first muon station (M1) of the LHCb experiment.
The use of a triple-GEM detector as a triggering device is certainly a novelty in the field of high energy physics. The first application of GEM detectors in high energy physics is the COMPASS experiment, where they are currently used as a tracking device.
A little interest has been devoted so far to the optimization of the time response of GEM detectors, while at LHC a critical issue is the high efficiency in the bunch-crossing identification, which requires a high detector time resolution.
Since the time resolution of a triple-GEM detector operated with an Ar/CO_2 (70/30) gas mixture is about 10 ns (r.m.s.), an intense R&D activity on GEM detectors for the Level 0 LHCb muon trigger has been performed by our group. The use of fast CF_4 and isobutane based gas mixtures, together with an optimization of the geometry and the electric fields of

Abstract

the detector, has allowed to improve the time resolution of the single detector down to 5 ns (r.m.s.), largely fulfilling the requirements of the experiment ($\sigma_t \leq 3$ ns is achieved by two OR-ed detectors, as foreseen in the muon station of LHCb).
In addition we have demonstrated that the detector is robust from the point of view of both discharges and ageing processes, and can tolerate the radiation dose foreseen in 10 years of operation in the region M1R1 of the LHCb experiment.

In the second part of the thesis is reported a complete study of the processes $pp \to Z^0 \to \mu^+\mu^-$ and $pp \to W^\pm \to \mu^\pm\nu$ in order to perform an on-line luminosity measurement during the data taking of LHCb. These physical channels, marginal respect to the main LHCb physics program, have recently gained interest due to the increased theoretical accuracy in the calculation of their production cross-sections. A particular focus has been put on the detection performances of LHCb, on off-line and on-line event selections, as well as on the time needed to perform an absolute luminosity measurement with a high accuracy.

Chapter 1

The LHCb experiment at LHC

1.1 The LHC machine

To explore physics up to the TeV scale, the next generation of experiments at CERN is under development within the LHC project. Given that most of the interesting physics require high interaction rates, the construction of a proton-proton collider at a center of mass energy $\sqrt{s}$ = 14 TeV with a design luminosity of 10^{34} cm^{-2}s^{-1} is under way and should be commissioned in 2007. The project will benefit from the existing infrastructure, namely the 27 km long circular underground tunnel used for LEP, and its versatile and well-know accelerator injection complex. So, it profits in term of know-how and cost saving.
The proton beams are accelerated in a linear accelerator (Linac) up to 50 MeV. Then two circular accelerator boost them to 1.4 GeV in the Proton Synchrotron Booster (PSB) and to 25 GeV in the Proton Synchrotron (PS), before they enter in the Super Proton Synchrotron (SPS). There they reach the energy of 450 GeV and enter the LHC via two tunnels (Fig. 1.1). The main design parameters of the LHC machine is reported in Tab. 1.1 [1].

The basic layout of the machine mirrors is the same of the LEP, with eight straight sections each approximately 538 m long, available for experimental insertions or utilities. Four of these sections will have the beam crossing from one ring to the other and are therefore dedicated to experimental sites, two of which will also host the injection system. Two insertions will contain collimation systems using only classical robust magnets (betatron and momentum cleaning). One inserting will contain the RF system and the last straight section will contain the beam dump insertion to remove the beam safely from the collider at the end

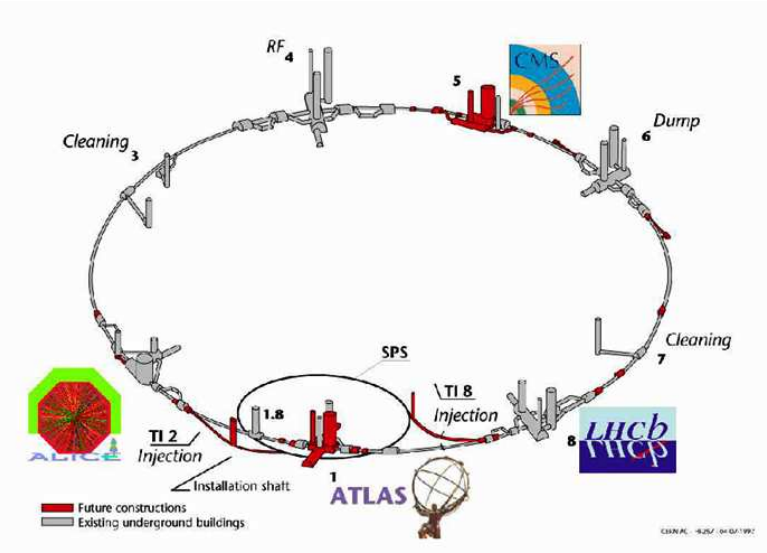

Figure 1.1: The LHC complex.

of a physics run, when the luminosity has degraded.
After the commissioning period in 2007, the LHC will deliver beams for physics with a starting luminosity of 5×10^{32} cm^{-2}s^{-1} to be steadily increased to its nominal value of 10^{34} cm^{-2}s^{-1} over the first three years of operation.

The choice for a proton accelerator was driven by the fact the losses by synchrotron radiation for electrons of the same energy are prohibitive, as illustrated by LEP run II. Indeed, the beam energy was been forced to the limit of $\simeq$ 104 GeV (intermittent) despite of a full use of superconducting technology. The huge RF power was then consumed just to compensate for the losses.
Two identical proton beams have been chosen to satisfy the high luminosity requirement. An antiproton beam would have simplified the technical conception but, given the low efficiency to produce it, the resulting luminosity would have been too small. As a consequence and in order to manage with the room in the existing tunnel, the magnet configuration is unusual as shown in Fig. 1.2. Two coil assemblies surrounding the two beam pipes are enclosed in the same iron yoke and cryostat. Given the radius of curvature of the orbit, the required huge operation field of 8.4 Tesla can only be obtained at acceptable cost by cooling the magnets to 1.9 Kelvin. There will be about 1200 of such 14 m long dipole magnets in the main arcs (Fig. 1.3).

Machine circumference	26659 m
Beam energy	7 TeV
Luminosity	10^{34} cm^{-2}s^{-1}
Luminosity lifetime	10 h
Number of bunches	2835
Particle per bunch	10^{11}
Bunch spacing	25 ns
Energy loss per turn	6.7 keV
Crossing angle	300 μrad
r.m.s. IP beam radius	16 μm
r.m.s. IP beam length	5.3 cm
Dipole field	8.4 T

Table 1.1: The LHC machine parameters [1].

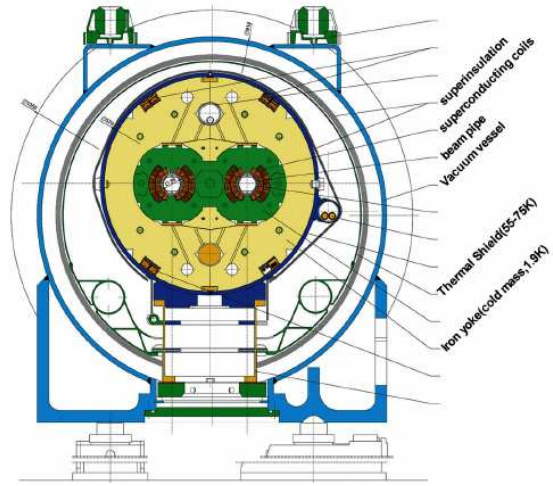

Figure 1.2: Cross section of a LHC dipole magnet. The inner coil keeps the two separated beams in orbit by using a 8.4 TeV T field. The coil is encapsulated in a cryogenic system, keeping the magnet at temperature of 1.9 K.

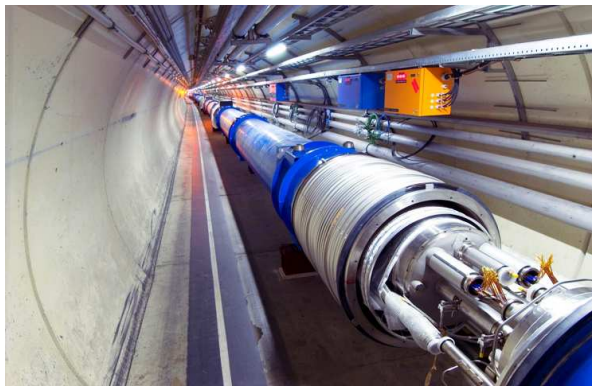

Figure 1.3: Picture of the LHC dipole magnet during the machine assembly.

The synchrotron energy loss per turn amounts to 6.7 keV . In terms of RF power load, this loss is insignificant for 7 TeV protons beams. Otherwise, the emitted power of 3.7 kW can not be neglected. Indeed, it has to be absorbed by the beam pipe, that work at cryogenic temperature, thus it could affect the power of refrigeration system. An additional issue is the release of absorbed gas molecules, when the synchrotron light impinges on the beam pipe (hard UV photons), which increases the residual gas pressure.
Let's mentioned the 10^{-7} of the stored beam intensity is enough to quench a magnet and consequently abort the run. This shows how is demanding the design of this new machine.

Five experiments will make use of LHC. The ATLAS and CMS experiments located in new caverns built at IP1 and IP5 are multi-purpose central detectors. Their main (but not unique task) is to find the Higgs boson, using the full LHC potential by running at the very high design luminosity $\mathcal{L}$ = 10^{34} cm^{-2}s^{-1}. The ALICE experiment at IP2 will study the quark-gluon plasma in dedicated runs for heavy ions (*Pb-Pb*) collisions. TOTEM is a very small detector studying very forward QCD processes at IP5. It will measure the total cross section at LHC, which is very important for the other experiments, for instance to measure absolute luminosity. Finally, the LHCb experiment in IP8 is dedicated to b-quark physics and will described in detail in Sec. 1.2.

1.1.1 The proton-proton interaction

Already at the startup of the collider, LHC will be a high-rate charm, beauty and top quark factories, as shown in Tab. 1.2. The inelastic cross section σ_{in} is extrapolated basing UA1, CDF and D0 [2] data but affected by large uncertainties.

Total	σ_{tot} = 100 mb
Inelastic	σ_{in} = 80 mb
$c\bar{c}$	$\sigma_{c\bar{c}}$ = 3.5 mb
$b\bar{b}$	$\sigma_{b\bar{b}}$ = 500 μb
$t\bar{t}$	$\sigma_{t\bar{t}}$ = 0.8 nb

Table 1.2: Cross sections at LHC.

The total inelastic cross section defines the average number of interactions per bunch

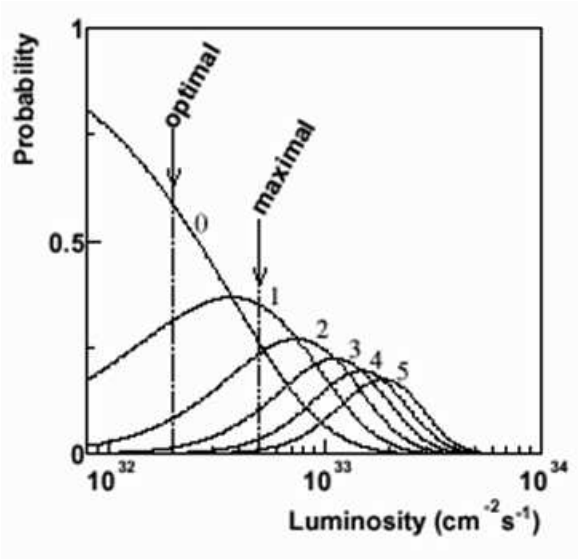

Figure 1.4: Probability distribution of the number of interaction per bunch crossing as a function of the luminosity. Although LHCb plans to operate at 2×10^{34} cm^{-2}s^{-1} ("optimal $\mathcal{L}$"), the LCHb subdetectors and data acquisition system are designed to cope up to 5×10^{34} cm^{-2}s^{-1} ("maximal $\mathcal{L}$").

crossing:

$$< N_{pp} >= \frac{\mathcal{L} \cdot \sigma_{in}}{f_{LHC} \cdot f_{ne}}$$

where $\mathcal{L}$ is the integrated luminosity, f_{LHC} is the 40 MHz bunch crossing frequency of the LHC machine and f_{ne} = 0.744 is the fraction of non-empty bunches crossing [1].
The average number of inelastic pp-interactions per bunch-crossing is $\sim$ 23 at the maximal luminosity $\mathcal{L}$ = 10^{34} cm^{-2}s^{-1} and 0.37 for LHCb, that will work at a lower average luminosity $\mathcal{L}$ = 2×10^{34} cm^{-2}s^{-1}, in order to avoid multiple pp interaction in the same event. At this luminosity there are interaction in the 30% of the bunch crossing, as can seen in Fig. 1.4, and the effective interaction rate is thus about 15 MHz.

The b quark production

The cross-section $\sigma_{b\bar{b}}$ will be between 175 and 950 μb depending on the value of badly known parameters. The value of 500 μb is a mean assumed as a reference by all LHC experiments. It will be known more precisely after the start of LHC. The dominant $b\bar{b}$ production mechanism

[1] Empty bunches arise due to a no-integer ratio of the PS, SPS and LHC revolution frequency.

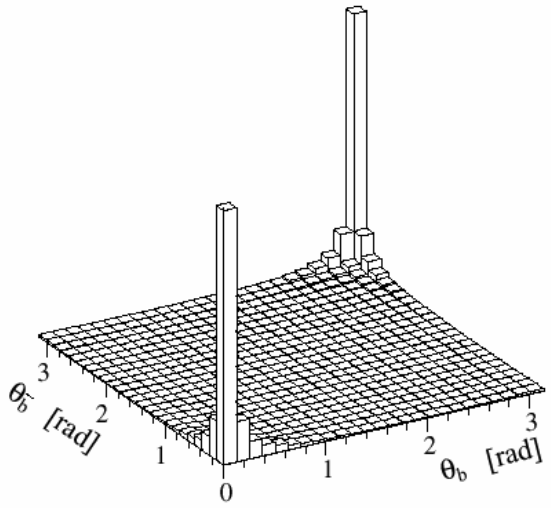

Figure 1.5: Polar angle θ of b and $\bar{b}$ hadron directions.

in pp collisions is the fusion of two or more gluons radiated from the constituent quarks of the protons. This leads to an approximately flat distribution in rapidity and hence an angular distribution peaked at low polar angles. The directions of the two b hadrons are very correlated as shown in Fig. 1.5. The two peaks correspond to $b\bar{b}$ pair flying in either directions of the beam axis. Consequently a dedicated b-physics experiment should cover low polar angles.

1.2 The LHCb experiment

The LHCb detector [3], [4] is a single-arm spectrometer dedicated to the study of CP violation and other rare phenomena in the decay of Beauty particles. Its main features are:

- a precise particle identification to access a wide range of multi-particle final states;
- a high resolution of the vertex detector to identify secondary vertices and to measure precise proper-time;
- a fast and versatile trigger system to select the interesting events among the huge number of *minimum bias* events ($\sigma_{b\bar{b}}/\sigma_{in}$ = 0.6%).

The LHCb detector design looks like a fixed target experiment (i.e. HERA-B) because of the very forward peaked b-quark distribution at LHC. It will be located at IP8 in the pit where the Delphi experiment used to be. To avoid any civil engineering the detector has to fit in the present cavern, which constraints the total length of the detector to 20 m and require a displacement of the interaction point by 11 m.
The geometrical acceptance of the detector, as defined by the aperture of the magnet, is 300 mrad in the horizontal plane (*bending plane*) and 250 mrad in the vertical plane. With this acceptance and the foreseen performance, the LHCb could detect the decay of both b hadron for about 20% of the whole $b\bar{b}$ events produced in 4π. The B-hadrons have an average momentum of 80 GeV/c, which corresponds to a mean decay length of about 7 mm.
The choice of the "optimal luminosity", $\mathcal{L}$ = 2×10^{32} cm^{-2}s^{-1}, is the result of a compromise between the maximization of having one interaction per bunch crossing and the need to keep low the radiation damages.

The experimental apparatus is shown in Fig. 1.6 and consists of five main sub-detector:

- the vertex system;
- the tracking system;
- the ring cherenkov detectors;
- the electromagnetic and hadronic calorimeters;
- the muon system.

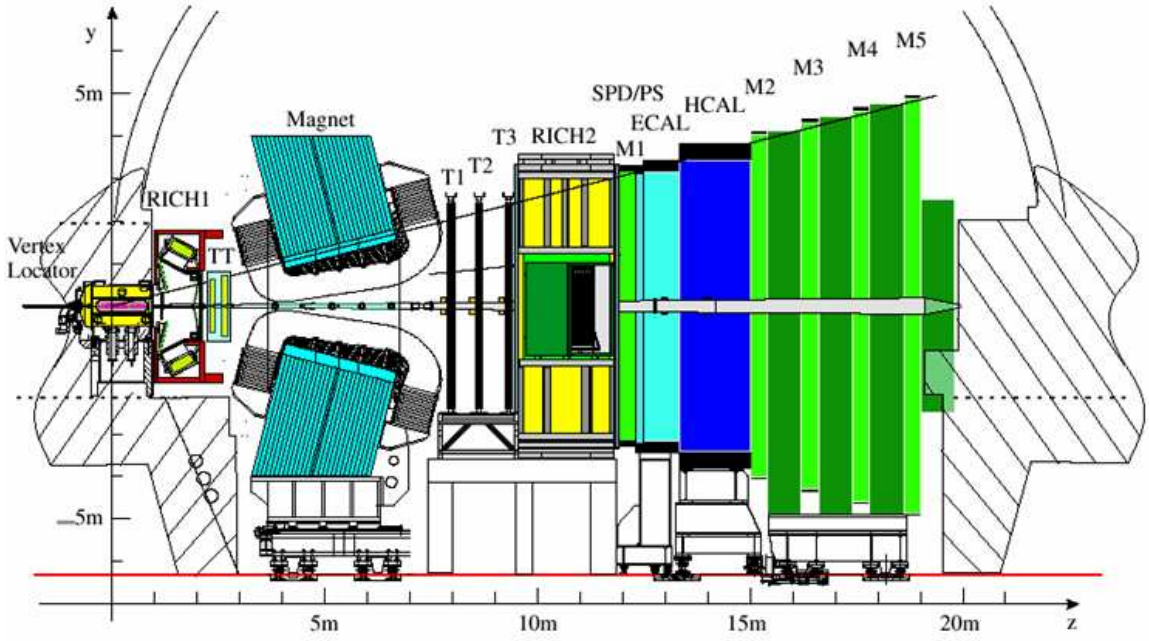

Figure 1.6: Cross section of the LHCb spectrometer.

1.2.1 The vertex detector system

The Vertex Locator (VELO) [5] provides precise informations about charged particles close to the interaction point. Its fine segmentation allows for a precise primary vertex reconstruction and search for detached secondary vertices. As it surrounds the interaction region it also allows some knowledge about the backward side of the event, which helps disentangling multiple primary vertices.
The detector is composed of 21 parallel disk-shaped silicon strips, with a $r-\phi$ segmentation geometry, and distributed over 1 m along the beam axis around the interaction point. They will be mounted perpendicular to that axis on Roman pots inside a vacuum tank and will be retracted from the beams during injection (Fig. 1.7).

The position resolution of the primary vertex is 40 μm in z and 8 μm in x and y. For secondary vertices it varies from 150 to 300 μm (in z) depending on the number of tracks. This corresponds to less than 40 fs resolution on the B proper time of flight.
The VELO is used for the Level-1 trigger which enriches the B event content by finding high impact parameter tracks and secondary vertices.

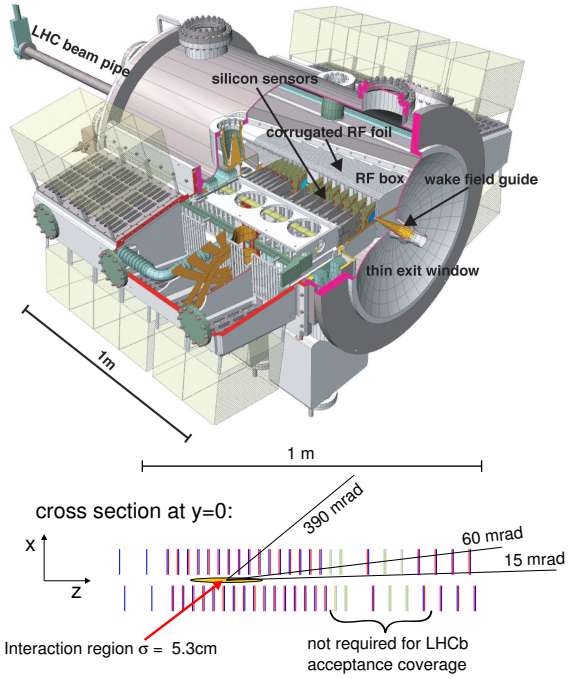

Figure 1.7: Up: The VELO vacuum vessel with the silicon sensor, RF box, and wakefield guides and exit window; Bottom: The station set-up.

1.2.2 The RICH detectors

The two Ring-Imaging Cherenkov detectors [6] use the Cerenkov effect to identify charged particles. Their main task is to allow the separation of kaons from pions over the full momentum range accessible from LHCb.

For the K-π separation the benchmark is the distinct between the $B \to K\pi$, $B \to \pi\pi$ and $B \to KK$ channels. The RICH achieves a K-π separation above 3σ for tracks in the range 1-150 GeV/c with an efficiency of $\sim 90\%$. It also crucial to tag the flavor of the reconstructed B hadron using the kaon from the $b \to c \to s$ decay chain from the other b-hadron.

The RICHs detect the ring images formed by Cherenkov photons around the particle traversing the detector. The photons are detected by cylindrical pixelated Hybrid photodiode (HPD) tubes. These detectors are sensitive to magnetic fields, which impose that RICH detectors are located outside of the bending area. Because of this requirement and the request to cover

a wide momentum range, a system consisting of two Ring Imaging Cherenkov has been design.
The first RICH (RICH-1) is placed upstream of the magnet and uses the silica aerogel (refractive index *n*=1.03) and C_4F_{10} (*n*=1.0014) as radiators. It is designed for low momentum (1-70 GeV/c) and high angle (30-300 mrad) tracks.
The second RICH (RICH-2) is located downstream the magnet and the T1-T3 trackers, and uses only the CF_4 (*n*=1.0005) as radiator. The RICH-2 covers high momentum (12-150 GeV/c) and low angle (15-120 mrad) tracks .

1.2.3 The magnet

The dipole magnet [7] is located close to the interaction point in order to keep it small, but downstream an iron shielding wall which protect the VELO and RICH1 from the magnetic field. The field is oriented vertically which makes the track to bend in the horizontal $x - z$ plane. It has a maximum intensity of 1.1 T and a total integral of 4 Tm on average. Charged particle passing through the magnet will receive a p_T kick of $\sim$ 1 GeV/c.
Its aperture is 300 mrad in the bending plane and 250 mrad in the vertical one. The magnet

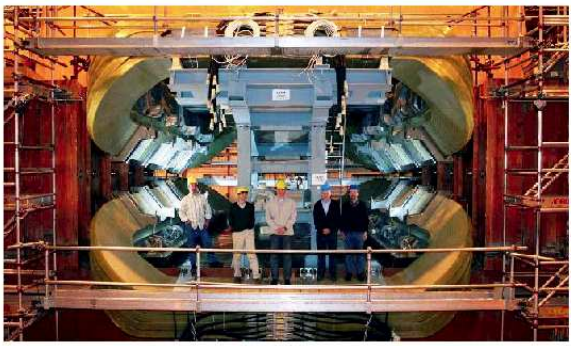

Figure 1.8: Photo of the LHCb magnet.

is made of 50 tons of aluminum conducting wires and of 120 kt steel plate yoke. It dissipates $\sim$ 4.2 MW.
To compensate a possible left-right asymmetries in the detector, the polarity of the magnet field can be reverse. This requirement and a detailed cost analysis have lead to the choice of a warm magnet rather than a superconducting magnet.

1.2.4 The tracking system

The tracking system consists of four stations: the Trigger Tracker (TT), located downstream the RICH1 and in front of the entrance of the magnet, and the three stations (T1,T2, and T3), located between the magnet and the RICH2.

The trigger tracker

The Trigger Tracker [4] has designed to fulfill two purposes. It will be used in the Level-1 trigger to assign a rough transverse momentum ($\sim$ 30%) to the large impact parameter tracks. This is done matching the tracks reconstructed in the VELO with the clusters in the TT station. It will be also used in the off-line analysis to reconstruct the trajectories of long lived neutral particles, which decay outside the VELO, and of low momentum particle, which are bent out of the acceptance of the experiment before reaching the tracking stations T1-T3.
The station is composed of four layers in order to readout the x, the y and the stereo (u and v) [2] coordinates. The layers are covered entirely by 300 μm thick silicon microstrip detectors with strip pitch of 200 μm and strip lengths of up to 33 cm. This allows to reach a spatial resolution of about 70 μm.

The T1-T3 trackers

The T1-T3 stations provide the momentum measurement of charged particles and link the tracks founded in the VELO to the hits in the TT station, in the calorimeters and in the muon detector. They also provide the seeding information for the RICH counters. A mass resolution requirement of 10 MeV in high-multiplicity decays such as $B_s^0 \rightarrow D_s K$ translate to a momentum resolution requirement of δp/p $\leq$ 0.4%.
To reduce particle occupancy, the T1-T3 stations are segmented in a Inner Tracker, located close to the beam pipe, and a Outer Tracker, which covers the remaining 98% of the area.
The Inner Tracker [8] has been design with the same technology of the Trigger Tracker, while the Outer Tracker [9] is made of drift cells called straw tubes.
These have a 5 mm diameter and 75 μm thick walls. To reach an average resolution on the momentum of δp/p $\leq$ 0.4%, the tracking precision has be optimal in the $x - z$ magnet bending plane. Therefore, the Out Tracker stations have two planes with wires in the vertical

[2] These layers are rotated $\pm$ 5 ^{o}5 respect to x one.

direction and two stereo planes with wires in the horizontal direction. The drift gas is an Ar/CO_2/CF_4 mixture which optimizes the spatial resolution ($\sim$ 200 μm) and the drift velocity. The total drift time, convolution of amplification and transmission time, is kept slightly below 50 ns. This time represents the delay between two LHC bunch crossing and it can be happen that two events are pile-up in the outer tracker. For this reason, the T1-T3 tracker can not be used in the trigger filters but only in the off-line.

1.2.5 The Calorimeters system

The calorimeter system [10] identifies hadrons, electrons and photons and measures their energy and position. These informations are used as input to the Level-0 trigger.
As for the VELO, the calorimeter design is motivated by fast triggering requirements. Thus the detector description is a compromise between a small number of read-out channels and low occupancy with a reasonable energy and position resolution.
The calorimeter system is placed downstream the RICH-2 and the first muon station (M1) and consists of an electromagnetic and a hadronic calorimeter (Fig. 1.9).

(a) The Electromagnetic Calorimeter.

(b) The Hadron Calorimeter.

Figure 1.9: Pictures of the Calorimeter system during the assembly phase.

The Electromagnetic Calorimeter and the Preshower

The electronmagnetic calorimeter (ECAL) detects electrons and photons via shovers of e^+e^- pairs and photons. Its total radiation length is 25 X_0. It is segmented in two parts.
The Preshower consists of 12 mm of lead followed by 15 mm of scintillators. It allows the separation of photons and electrons by the shapes of the electromagnetic shower induced in the ECAL. The electromagnetic calorimeter uses the Shashlik technology with lead as absorber material. It is segmented in three resolution zones in order to optimize the π^0 reconstruction.
The energy resolution of the ECAL is:

$$\frac{\sigma(E)}{E} = \frac{10\%}{\sqrt{E}} \oplus 1.5\%$$

The Hadronic Calorimeter

The hadronic calorimeter (HCAL) identifies hadrons ($\pi^{\pm}$, $K^{\pm}$, K^0_L, p, n, Λ) via inelastic interactions with the detector material. The product of the interaction are mainly π which are detected in the scintillator (the π^0 via the electromagnetic shower of the γ).
The HCAL is made of 16 mm thick iron and 4 mm thick scintillating tiles, parallel to the beam. The light is collected at the end of the tile by wavelength shifting fibers (WLS).
The energy resolution of the HCAL is:

$$\frac{\sigma(E)}{E} = \frac{80\%}{\sqrt{E}} \oplus 5\%$$

1.2.6 The Muon system

The Muon system [11] identifies muons, the only charged particle able to transverse the calorimeters without interacting. As high p_T muons are mainly produced in B decays, the muon detector is an essential component of the Level-0 trigger. It also used in the muon identification which is a basic ingredient of the search for rare semileptonic decays.
The detector consists of five tracking stations and of a muon shield (composed of the ECAL, the HCAL and three layers of iron). It will be discussed in more detail in the second chapter.

1.3 The LHCb trigger

The trigger is a vital component of the LHCb experiment and it is the major challenge. Most sub-detectors designs are motivated by triggering considerations. The high interaction rate, the low b cross-section compared to the total cross-section and the high-multiplicity environment make arduous to efficiently select interesting B-decays.
The bunch-crossing frequency is 40 MHz. Every 25 ns a pp event can occur. At $\mathcal{L}$ =2$\times$10^{32} cm^{-2}s^{-1} an inelastic pp interaction (called *minimum bias*) happens at an average rate of about 15 MHz. The ratio of the inelastic *minimum bias* and $b\bar{b}$ cross-section is about 100. The $b\bar{b}$ production rate is thus about 150 kHz.
Essentially rare B^0 decays - $\mathcal{O}(10^{-3})$ or less - are of the interest for $\mathcal{CP}$ violation studies. Adding up all the physics channels (listed in [3]) one gets 120 physics events per second. Requiring that all tracks are detected one ends with about 10 B events per second which can be used for physics analysis.
For every B event of interest there are thus 10^6 background events. The reduction to 2 thousand events that will be written to storage per second is achieved in a three level trigger scheme [12]. The step of the trigger algorithm are described below and summarized in Tab. 1.3.

Level	Selects	Input rate	Reduction	Latency
Level-0	High p_T tracks	15 MHz	15	4 μs
Level-1	Secondary vertices	1 MHz	25	$\sim$ 1 ms
HLT	Reconstructed B events	40 kHz	20	
Events written on the tape		2 kHz		

Table 1.3: Summary of the trigger scheme.

1.3.1 The Level-0 trigger

The Level-0 trigger (L0) exploits the high mass of the B-meson, resulting in decay products with high transverse momentum (p_T). High p_T photons, electrons, hadrons and muons are reconstructed in the electromagnetic, hadronic calorimeter and the muon system respectively.
The Pile-Up system, consisting of two VELO disks upstream the interaction region, identi-

fies multiple interactions and is used to suppress events with multiple vertices or with large hit multiplicity. The Pile-Up information, together with the highest p_T photons, electrons, hadrons and the two highest p_T muons, are passed to the L0 decision unit, which forms the final decision. The particles which pass the L0 filter are called L0 candidates.
The fully synchronous L0 trigger has a fixed latency of 4 μs and is implemented in custom boards. The rate at the L0 output is reduced to 1 MHz. Efficiencies of 60%, 50% and 90% are achieved for events with hadrons, electrons and muons respectively [13].
The relative weight of each trigger can be tuned by changing the single cuts, depending on the type of the physics one want to favor. The optimization of the cuts for the precise measurements of $\mathcal{CP}$-violating parameters leads a bandwidth of 70% for the hadron trigger, 28% for the electron and photon trigger, 16% for the muon trigger.

1.3.2 The Level-1 trigger

The Level-1 trigger (L1) reduces the rate further to 40 kHz, combining the informations from the VELO, the TT station and the L0 candidates.
The algorithm will be implemented on a commodity processor farm, that will be shared with the High Level Trigger (HLT) and the off-line reconstruction. The available time at L1 is on average $\sim$ 1 ms, with a maximum latency of 52 ms given by the L1 buffer size.
Large impact parameter tracks are reconstructed in the VELO and matched to the clusters in the TT station. The fringe field between the VELO and the TT is sufficient to obtain momentum information with a precision of $\sim$ 30%. In addition the tracks are matched to muon and calorimeter candidate from L0, enhancing mainly the performance for channels containing muons and electrons. Using two high impact parameter tracks with the highest p_T, efficiencies between 50% and 80% are achieved [14].

1.3.3 The High Level Trigger

The full detector information is available at the High Level Trigger (HLT) [3]. The tracking stations (T1-T3) provide a more precise momentum information (δ/p $\sim$ 0.4%), with which the L1 decision can be confirmed within 4 ms, reducing the rate by a factor 20, while retaining signal efficiency above 95%. The remaining time ($\sim$ 14 ms) is used to select the

[3] The RICH information is not currently used by the HLT

individual channels with an output rate of $\sim$ 10 Hz per channel [15]. The maximum total output rate of HLT will be fixed to 2 kHz.

1.4 B-physics performances and sensitivity

Compared to other accelerators that are in operation, LHC will be the most copious source of B mesons due to both the high $b\bar{b}$ cross section and the high luminosity. Tab. 1.4 summarizes the features of the different colliders together with the B production.

	PEP-II	Tevatron	LHC
beam	e^+e^-	$p\bar{p}$	pp
center of mass energy $\sqrt{s}$	10.6 GeV	2 TeV	14 TeV
$\mathcal{L}$ [cm^{-2}s^{-1}]	3×10^{33}	2×10^{32}	10^{32}-10^{34}
$b\bar{b}$ pairs/years	3×10^{7}	2×10^{11}	10^{12}-10^{13}
σ_b	1.1 nb	100 μb	500 μb
σ_{in}	0.24 nb	50 mb	80 mb
ratio σ_b/σ_{in}	0.22	2×10^{-3}	6×10^{-3}
$B^+/B^0/B_s^0/B_c, \Lambda_b$ mixture	50/50/0/0	40/40/12/8	40/40/12/8

Table 1.4: Features of the different colliders compared to the LHC machine. The B physics is also reported.

In general, the advantage of the experiments on e^+e^- machine is to have the better signal to background ratio ($\sim$ 0.22), but in absolute the statistics is limited (10^7 $b\bar{b}$/years) compared to hadron machine.
Furthermore at $\Upsilon(4s)$ center of mass energy only the two lightest B-mesons, B_u and B_d in equal proportion, are produced, while at LHC a variety of b-hadrons will be produced: B_u (40%), B_d (10%), B_s (10%) and B_c/b baryons (10%).

The asymmetric e^+e^- B factories, with their detector Babar (SLAC) and Belle (KEK), have measured $\mathcal{CP}$ violation in the B_d^0 system with a very high accuracy. From the decay $B^0 \rightarrow J/\psi K_s^0$, BaBar and Belle have measured the angle β, sin2β = 0.687 $\pm$ 0.032 [17], with a high precision and in excellent agreement with the indirect measurement of V_{ub}/V_{cb} and Δm_d from semi-leptonic B^0 decays, and $B - \overline{B}$ oscillation [16].

On the other hand, the measurements of the angles α, coming from $B^0 \to \pi\pi$, $B^0 \to \pi\rho$ and $B^0 \to \rho\rho$ decays, and γ, coming from $B^+ \to D^0 K^+$, are limited by the low statistics. Presently the measurements of these angle are [17]: sin2α = -0.50 $\pm$ 0.12 and γ = 65 $\pm$ 18. In Tab. 1.5 the current experimental results on the B physics are summarized, while in Fig. 1.10 the present status on the Unitary Triangle taken from the UTFIT homepage is shown [17].

Channel	Physics Observable	Measurement (@95% C.L.)	Experiment
$B \to J/\psi K^0_s$	sin2β	0.687$\pm$ 0.032	BaBar/Belle
$B \to J/\psi K^0_s$	cos2β	1.9$\pm$1.3	Babar/Belle
$B \to \pi^+\pi^-$	sin2α	-0.50$\pm$0.12	BaBar/Belle
$B \to \pi^+\pi^-$	cos2α	-0.37$\pm$0.10	Babar/Belle
$B \to DK$	γ	(68$\pm$ 17)^o	BaBar/Belle
$B^0 \to D^0\pi, D\rho$	$2\beta + \gamma$	($\pm$90 $\pm$ 46)^o	BaBar/Belle
$B^0_d - \overline{B}^0_d$ oscillation	Δm_d	(0.494 $\pm$ 0.007) ps^{-1}	CDF/CLEO/LEP/BaBar/Belle
$B^0_s - \overline{B}^0_s$ oscillation	Δm_s	$>$ 14.5 ps^{-1}	CDF/D0/LEP/SLD
B.R. ($B^0_s \to \mu^+\mu^-$)	Rare Decay	$< 3.5\times10^{-9}$	D0

Table 1.5: Current results on the B physics taken from the UTFIT homepage [17].

At the LHC energy, the high number of B_s-$\overline{B_s}$ pairs per years ($\sim 10^{11}$) will enable to measure the γ and $\delta\gamma$ angles and the triangle side opposite to γ angle (corresponding to $|V_{td}/V_{cb}|$) with a very high accuracy. Moreover, the physics potential of B^0_s and the relative rare decays, which are absent at the tree level in the Standard Model (SM), will provide a very fertile testing ground for the SM picture of flavour physics as well as the fulfillment of the studies of $\mathcal{CP}$ violation and will allow for interesting probes for new physics.

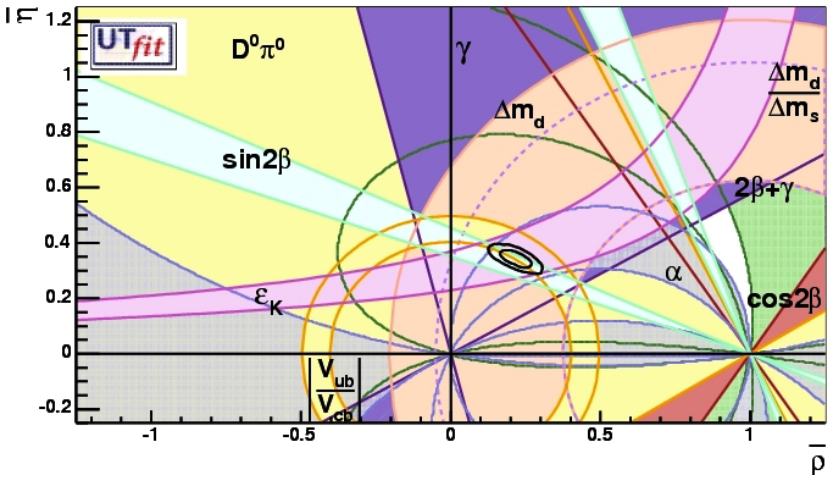

Figure 1.10: Allowed regions for ($\overline{\rho}$-$\overline{\eta}$). The closed contours at 68% and 95% probability are shown. The full lines correspond to 95% probability regions for the constraints, given by the measurements of $|V_{ub}|/|V_{cb}|$, ϵ_K, Δm_d, Δm_s, sin2β, α, and γ. The dotted curve corresponds to the 95% upper limit obtained from the experimental study of B_s^0 oscillations [17].

1.4.1 B-physics at LHC

At the LHC, B-physics will be studied with two general purpose detectors ATLAS [18] and CMS [19], and the dedicate B-physics experiment, LHCb (Tab. 1.6). The former two are designed for high luminosity running and provide hermetic coverage, which is essential for Higgs and SUSY discover, while LHCb have a detector geometry optimized for the requirements of the B-physics. In fact, at the LHC energy, the $b - \bar{b}$ pairs are preferentially emitted under a small angle relative to the beam direction.

The phase coverage of these experiments is shown in Fig. 1.11.

	LHCb	ATLAS/CMS
Detector configuration	Single-arm forward	Central detector
Running luminosity [cm^{-2}s^{-1}]	2×10^{32}	3×10^{34}
pseudo-rapidity range (η)	1.9 ÷ 4.9	-2.5 ÷ 2.5
$<$ interactions/crossing $>$	$\sim$0.4 ($\sim$ 30% single int.)	$\sim$ 23
$b\bar{b}$ pairs/years(integrated in the η range)	10^{12}	5×10^{13}

Table 1.6: Comparison of the LHC experiment parameters.

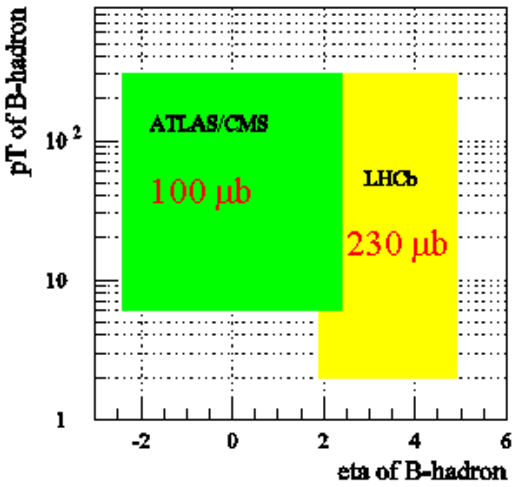

Figure 1.11: Phase space coverage of the LHC experiments for B-physics.

LHCb can measure down to p_T = 2 GeV/c and thereby, despite its small angular coverage $1.9 < \eta < 4.9$, has access to a visible b-cross section of about 230 μb. On the other hand, ATLAS and CMS, covering the central range $|\eta| < 2.5$ and operating at higher luminosity, have to raise the p_T-threshold to values around 10 GeV/c in order to achieve sufficient background reduction.
In addition, the presence of RICH detectors in LHCb allows to study with an high efficiency pure hadronic decays due to the high K-π separation (3σ) in a wide momentum range (1-150 GeV/c). On the contrary, ATLAS and CMS have no a dedicated hadronic particle identification detectors. For example, the Transition Radiation Detector (TRD) of ATLAS provides a dE/dx measurement giving a K/π separation of about 0.8σ, precluding most of the hadronic B decays.

Completely different is the case of the rare B decays, such as $B_s^0 \rightarrow \mu^+\mu^-$ where the foreseen SM branching ratio is about 3.5×10^{-9} [20]. The high p_T dimuon triggers running at high luminosity (1×10^{34} cm^{-2}s^{-1}) gives a distinctive advantage over the forward detector. With its excellent muon detection capability, CMS can observe an estimated 26 signal events with 6.4 events background for 100 fb^{-1} of running.

In Tab. 1.7 the sensitivity of LHCb and ATLAS/CMS are summarized for a selection of benchmark channels for one years of running, corresponding to an integrated luminosity of 2 fb^{-1} and 100 fb^{-1} respectively.

Channel	Physics Observable	LHCb	ATLAS	CMS
$B_d^0 \to J/\psi K_s^0$	β	0.3÷0.5 ^{o}	0.6 ^{o}	0.7 ^{o}
$B_d^0 \to \pi\pi$	α	2÷10 ^{o}	3 ^{o}	5 ^{o}
$B_d^0 \to \rho\pi$	α	5÷15 ^{o}	-	-
$B_d^0 \to D^0 K$	γ	4÷18 ^{o}	-	-
$B_d^0 \to D^*\pi$,3π	2β+γ	$< 7^o$	-	-
$B_s^0 \to J/\psi\Phi$	$\delta\gamma$	0.6^o	0.9 ^{o}	-
$B_s^0 \to D_s K$	$\gamma - 2\delta\gamma$	3÷16 ^{o}	-	-
$B_s^0 \to \mu^+\mu^-$	Rare decay	4.4σ S.M.	4.3σ S.M.	10σ S.M.

Table 1.7: Performance of the LHC experiments in a selection of benchmark channels for one year of operation at the relative luminosity. The quoted numbers are the errors on parameter in question. A dash for an entry means that no significant measurement can be made [21].

Chapter 2

The Muon System

2.1 Introduction

Muon triggering and off-line muon identification are fundamental requirements of the LHCb experiment. Muons are present in the final states of many $\mathcal{CP}$-sensitive B decays, in particular the two "gold-plated" decays, $B_d^0 \rightarrow$J/$\psi(\mu^+\mu^-)$K$_s^0$ and $B_s^0 \rightarrow$J/$\psi(\mu^+\mu^-)\Phi$. Moreover, muons from semi-leptonic b decays provide a tag of the initial state flavour of accompanying neutral B mesons. In addition, the study of rare B decays such as the Flavour Changing Neutral Current decay, B$_s^0 \rightarrow \mu^+\mu^-$ may reveal new physics beyond the Standard Model.
The LHCb muon detector uses the penetrative power of muons to provide a robust muon trigger. The heavy-flavour content of triggered events is enhanced by requiring the candidate muons to have high transverse momentum, p_T. The same unique properties are utilized off-line, to accurately identify muons reconstructed in the tracking system and to provide a powerful B-meson flavour tag.

2.2 Physics requirements

The main requirement for the muon detector is to provide a high-p_T muon trigger at the earliest trigger level (Level-0). The effective LHCb Level-0 input rate is about 15 MHz on average at $\mathcal{L}$ = 2$\times$10^{32} cm^{-2} s^{-1}, assuming an inelastic pp cross-section of 80 mb. This input rate must be reduced to 1 MHz within a latency of 4.0μs, while retaining good efficiency for events containing interesting B decays. The muon trigger provides between 10% and 30%

of this trigger rate. In addition, the muon trigger must unambiguously identify the bunch crossing, requiring a time resolution better than 25 ns.
The muon system must also provide offline muon identification. Muons reconstructed in the high precision tracking detectors with momenta down to 3 GeV/c must be correctly identified with an efficiency of above 90%, while keeping the pion misidentification probability below 1%. Efficient muon identification with low contamination is required both for tagging and for the clean reconstruction of muonic final state B decays.
The muon trigger is based on a muon track reconstruction and p_T measurement with a resolution of $\sim$ 20%. Hits in the first two stations are used to calculate the p_T of the candidate muon.

2.3 General detector structure

The muon detector consists of five muon tracking stations placed along the beam axis.
The first station (M1) is placed in front of the calorimeter preshower, at 12.1 m from the interaction point, and is important for the transverse-momentum measurement of the muon track used in the Level-0 muon trigger. Therefore, the M1 position requires a radiation length of the detector materials below 10% of X_0 on average, in order to not degraded the electromagnetic and hadron energies.
The remaining four stations are embedded within the muon shield at mean positions of 15.2 m (M2), 16.4 m (M3), 17.6 m (M4) and 18.8 m (M5). The shield is comprised of the electromagnetic and hadronic calorimeters and three iron filters and has a total absorbtion-length of 20 nuclear interaction-lengths. The minimum momentum requested to traverse the 5 muon stations is 8 GeV/c. The positions of the muon stations can be seen in Fig. 2.1, which shows a side view.

The chambers within the filter are allocated about 40 cm of space and are separated by three shields of 80 cm thickness. The angular acceptances of the muon system is from 20 to 306 mrad in the bending plane and from 16 to 256 mrad in the non-bending plane, similar to that of the tracking system. This provides a geometrical acceptance of about 20 % of muons from b decays relative to the full solid angle. The total detector area is about 435 m^2.

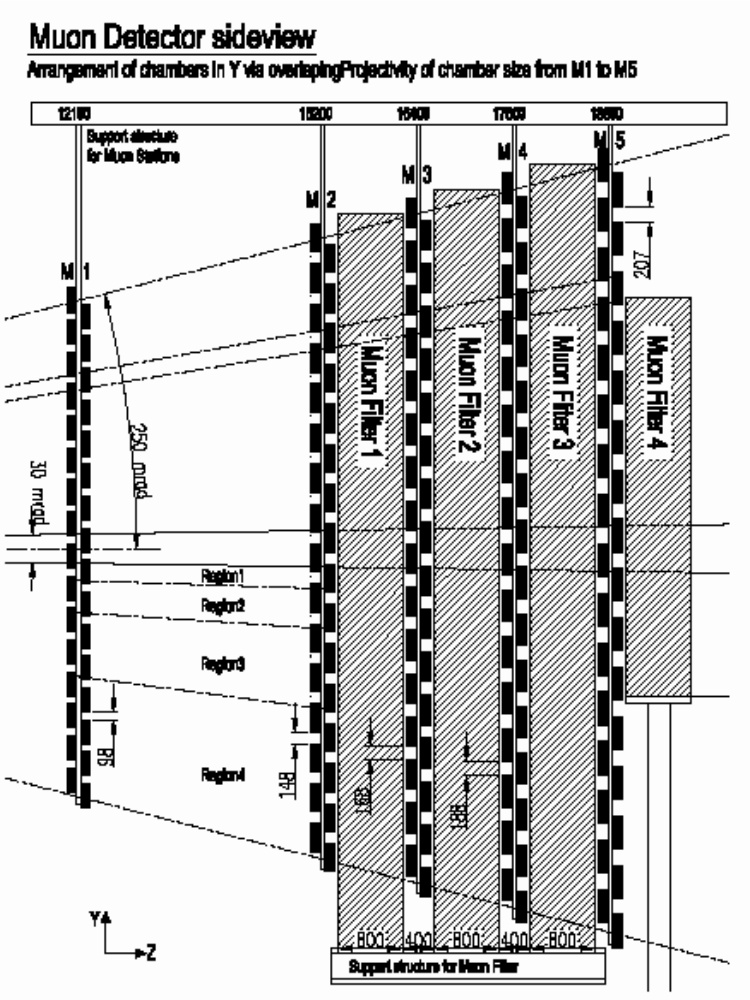

Figure 2.1: Side view of the muon system.

2.4 Logical layout

The Muon system provides a digital information about the $x - y$ spatial coordinates of the muon tracks. The spatial resolution is given by the dimension of a logical pad, whose structure across the detector represents the logical layout. The logical layout describes the x and y granularity in each region of each muon station, as seen by the muon trigger and off-line reconstruction.
Since the polar angle and momentum of particles are correlated, high momentum tracks tend to be closer to the beam axis. Therefore multiple scattering in the absorber increases with the distance from the beam axis, limiting the spatial resolution of the detector. The granularity of the logical pads varies accordingly and have been chosen such that its contribution to the p_T resolution is approximately equal to the multiple-scattering contribution. The various contributions to the p_T resolution are shown in Fig. 2.2.

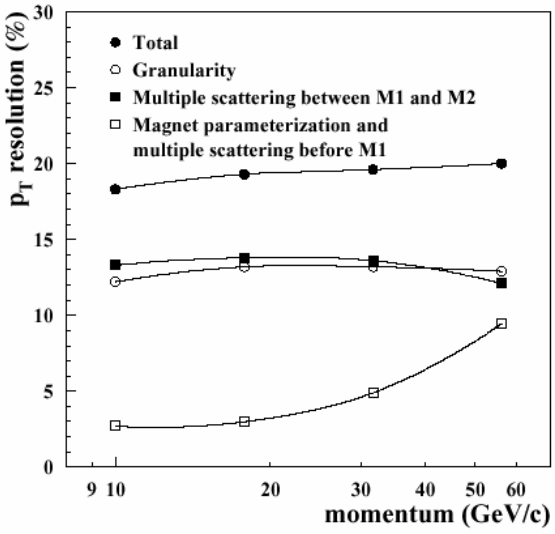

Figure 2.2: Contributions to the transverse momentum resolution of the muon system as a function of the muon momentum, averaged over the full acceptance. The p_T resolution is defined as $|p_{\mathrm{T}}^{rec} - p_{\mathrm{T}}^{true}|/p_{\mathrm{T}}^{true}$, and is shown for muons from semi-leptonic b decay having a reconstructed p_T close to the trigger threshold, between 1 and 2 GeV/c.

Given the different granularity and the large variation in particle flux from the central part, close to the beam axis, to the detector border, each station is subdivided into four regions with

different logical pad dimensions. Region and pad sizes scale by a factor two from one region to the next.

In the y plane all the tracks appear to straight lines, as they are not bent by the magnet, thus the required granularity is broader, and the logical pads are wide, as appear in Fig. 2.3. The y dimension is determinate principally by the rejection of background events which do not point to the interaction region.

Otherwise the x dimensions of the logical pads are determined primarily by the required precision to obtain a good muon p_T resolution for the Level-0 trigger.

The resulting y/x aspect ratios are 2.5 in station M1 and 5 for stations M2 and M3. Stations M4 and M5, which are used to confirm the presence of penetrating muons, have aspect ratios of 1.25. The total number of logical pads in the muon system is about 55 thousand.

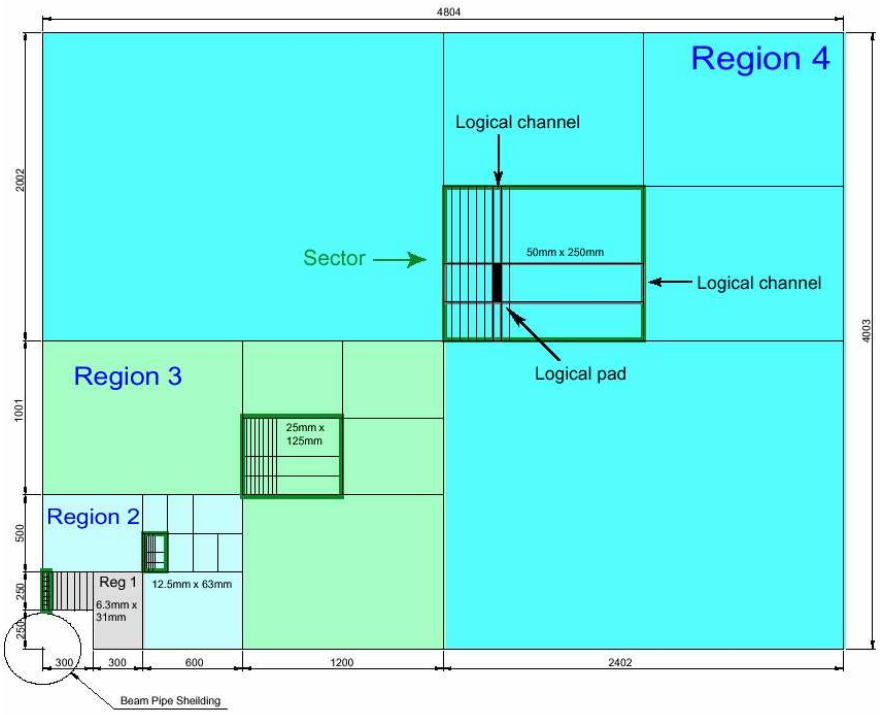

Figure 2.3: Front view of one quadrant of muon station 2, showing the dimensions of the regions. Inside each region is shown a sector, defined by the size of the horizontal and vertical strips. The intersection of the horizontal and vertical strips, corresponding to the logical channels, are logical pads. The region and channel dimensions scale by a factor two from one region to the next.

Each logical pad may group one or more physical pads, whose dimension are limited by occupancy and capacitance considerations, according to the detector technology. The Muon system has been designed in a flexible way, such that the required logical layout can be achieved in several ways and is independent from the detector used (Fig. 2.4).

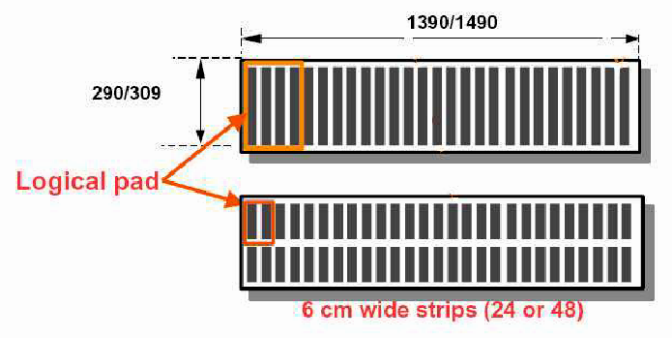

Figure 2.4: Logical pads and physical pads in Region 4 (top) and Region 2 (bottom) for Stations M4 and M5. In the former case the x dimension is that of 4 chamber strips and the y dimension is the same of the chamber itself. In the latter case more granularity is required and both x and y have half dimensions.

2.5 Detector Specifications

The basic function of the LHCb Muon system is to identify and trigger muons produced in the decay of b hadrons every bunch crossing. Therefore, the muon system design is motivated by fast triggering requirement.

The muon level-0 trigger (L0) is designed in such a way that information from all five muon stations is required, and looking for muon tracks with a large transverse momentum, p_T. The track finding is performed on the logical pad layout and the scheme shown in Fig. 2.5 is adopted. Starting from each hit in M3, called *track seed*, a straight-line is extrapolated forward the interaction point and backward up to the station M5. In M2, M4 and M5, hits are looked for a regions, the so-called field of interest (FOI), centered in the intersections between the station and the straight-line. If at least one hit is found in M2, M4, M5 FOIs, the track is flagged as a muon candidate. A second straight-line passing through the hit in M2 and the track seed, is extrapolated to M1 to define the center of the FOI. If at least one hit is found in the M1 FOI, the track is definitely flagged as a muon.
Since the logical layout is projective, there is a one-to-one mapping from pads in M3 to pads in M2, M4 and M5. There is also a one-to-one mapping from pairs of pads in M2 and M3 to pads in M1. This allows the track-finding algorithm to be implemented using only logical operations.
Once track finding is completed, an evaluation of p_T is performed for muon tracks. The p_T is determined from the track hits in M1 and M2. Because of the distance between M1 and M2 (3.1 m) and the high granularity of M1, a good resolution of the p_T measurement, $\sim$ 20%, is obtained. The momentum measurement assumes a particle from the interaction point and a single kick from the magnet.

A first consequence of this scheme is that the L0 trigger efficiency is highly affected by the single station efficiency, as follows:

$$\epsilon_{trigger} = (\epsilon_{station})^5$$

In order to improve the single station efficiency in 20 ns time window, providing also some redundancy, the M2-M5 stations consist of four independent detector layers, which are read-out as two double layers and then logically OR-ed. Only two detector layers are foreseen for the M1 station in order to reduce the material budget in front of the calorimeters.

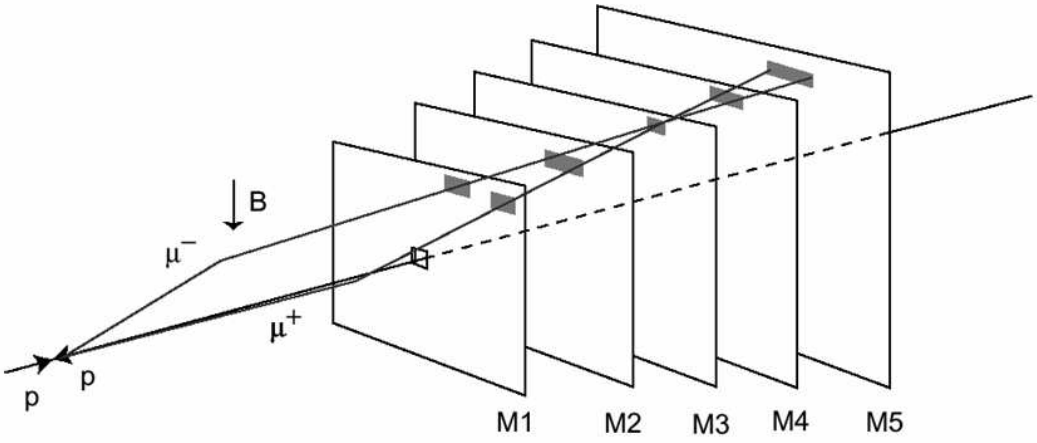

Figure 2.5: Track finding by the muon trigger. In the example shown, μ^+ and μ^- cross the same pad in M3. The highlighted in the various station represent the field of interest where the hits are searched.

The efficiency for M2-M5 stations must be $> 99\%$, and $> 96\%$ for the M1 station, where only two detector layers are foreseen.
As result of such stations efficiency requirement, the L0 trigger efficiency comes out to be higher than 92%.

On the other hand, the detector efficiency is mainly limited by the intense flux of charged and neutral particles in the angular coverage of the LHCb experiment. These flux levels exceed those experienced by the ATLAS [18] and CMS [19] muon spectrometers and pose a different challenge.

2.5.1 Background environment

High particle fluxes in the muon system impose stringent requirements on the instrumentation. These requirements include the rate capability of the chambers, the long radiation damages, the so-called ageing, and redundancy of the trigger instrumentation. The high hit rates in the chamber also effect the muon transverse momentum resolution due to incorrect hit association. Four classes of backgrounds relevant to the B$\rightarrow \mu$X detection can be distinguished:

1. *Decay muons:* The large number of π/K mesons produced in the $p - p$ collisions contribute mainly to the background in the muon system through decays in flight. Such

decay muons form the main background for the L0 muon trigger.

2. *Shower particles:* Photons from π^0 decays can interact in the area around the beam pipe and generate electromagnetic showers penetrating into the muon system. Hadrons emerging from the primary collision can interact late in the calorimeters and contribute to the background in the muon system through shower muons or hadron punch-through.

3. *Low-energy background:* Another important background is associated with low-energy neutrons produced in hadronic cascades in the calorimeters, the muon shield or in accelerator components. They create low-energy radiative electrons via nuclear n-γ processes and subsequent Compton-scattering or via the photo-electric effect in the detector material of the muon chambers. The photons have a probability of a few per mil to generate detectable electrons via these effects, which are in general only affecting a single detector layer. Moreover, the hits due to the low energy background occur up to a few 100 ns after the primary collision.

4. *Beam halo muons:* The charged-particle flux associated with the beam halo in the accelerator tunnel contains muons of a rather wide energy spectrum and the largest flux at small radii. In particular those halo muons traversing the detector in the same direction as particles from the interaction point can cause a L0 muon trigger.

Background caused by real muons traversing the detector is well simulated with the available Monte Carlo packages [22], [23]. An estimate for the rate in the various regions of the muon system has been obtained from a detailed study [24], [25], whose results are summarized in Tab. 2.1.

The nominal rates are calculated for a luminosity of $\mathcal{L} = 5\times10^{32}$ cm^{-2} s^{-1}. The maximal rates are then obtained applying a safety factor of 5 in the stations M2–M5 and a safety factor of 2 in the station M1, which is positioned in front of the calorimeters and therefore is less affected by the uncertainties in the showering processes in the absorber material. The rate rises from a few hundred Hz/cm^2 in the outer regions of stations M4 and M5 to a few hundred Hz/cm^2 in the innermost part of station M1.

	Station 1	Station 2	Station 3	Station 4	Station 5
Region 1	230 kHz/cm^2	7.5 kHz/cm^2	2 kHz/cm^2	2.3 kHz/cm^2	880 kHz/cm^2
	460 kHz/cm^2	37.5 kHz/cm^2	10 kHz/cm^2	6.5 kHz/cm^2	4.4 kHz/cm^2
Region 2	93 kHz/cm^2	5.3 kHz/cm^2	650 Hz/cm^2	430 Hz/cm^2	350 Hz/cm^2
	186 kHz/cm^2	26.5 kHz/cm^2	3.3 kHz/cm^2	2.2 kHz/cm^2	1.8 kHz/cm^2
Region 3	40 kHz/cm^2	1.3 kHz/cm^2	200 Hz/cm^2	150 Hz/cm^2	130 Hz/cm^2
	80 kHz/cm^2	6.5 kHz/cm^2	1.0 kHz/cm^2	750 Hz/cm^2	650 Hz/cm^2
Region 4	12.5 kHz/cm^2	230 Hz/cm^2	83 Hz/cm^2	50 Hz/cm^2	45 Hz/cm^2
	25 kHz/cm^2	1.2 kHz/cm^2	415 Hz/cm^2	250 Hz/cm^2	225 Hz/cm^2

Table 2.1: Particle rates in the muon system.The first row gives the calculated rate at a luminosity of $\mathcal{L}$ = 5×10^{32} cm^{-2} s^{-1} assuming a total $p-p$ cross-section of σ=102.4 mb; in the second row the rate includes the safety factors.

2.6 Muon system technologies

The combination of physics goals and background conditions have determined the choice of detector technologies for the various stations and regions. The following parameters particularly affects the technology choice:

1. *Rate capability:* The selected technologies must tolerate the expected particle rate without efficiency losses;

2. *Ageing:* The detector must tolerate, without damages or performance losses, the integrated charge accumulated in 10 years of operation;

3. *Time resolution:* The muon system must provide unambiguous bunch crossing identification with high efficiency. The requirement is at least 99% efficiency within 20 ns window for M2-M5 stations.
   For M1 station, as previously discussed, this efficiency is less stringent ($>$ 96%);

4. *Spatial resolution:* A good spatial resolution is required, especially in M1 and M2, in order to obtain an accurate p_T evaluation ($\sim$ 20%). Therefore it is important to reduce as much as possible the probability of having more than one pad fired by a crossing track. This effect is described as geometrical pad cluster size. Depending on the average crossing angle of the track, the pad size and the layer separation, the geometrical pad

cluster size varies between 1.1 in the outer part and 1.2 to the inner part of the muon system;

Based on the above considerations, the $\sim$ 99% of the area of the Muon system will be equipped with Multi Wire Proportional Chamber (MWPC) [26]. The innermost region (R1) of the first station (M1), where a particle flux up to $\sim$ 500 kHz/cm^2 is expected, will be instrumented with triple-GEM detectors (Gas Electron Multiplier) [27]. It should be stressed that the M1R1 region, of about $\sim$ 0.6 m^2 area, will trigger about 20% of the muons.

The technical specifications and the performances of the MWPC detectors are summarized in the following section, while the performances of a triple-GEM detector, which represents the object of my thesis, will be discussed in detail in the following two chapters.

2.6.1 MWPC detectors

The MWPC chambers for the station M2-M5 are composed by four symmetric gas gaps, each of them with a plane of anode wires in between of two cathode planes. The gap is 5 mm wide and the anode-cathode distance is 2.5 mm. The wires are made of gold-plated tungsten with a diameter of 30 μm and a pitch of 2 mm. A schematic view is given in Fig. 2.6, while in Tab. 2.2 are summarized the main parameters of the MWPC detectors.

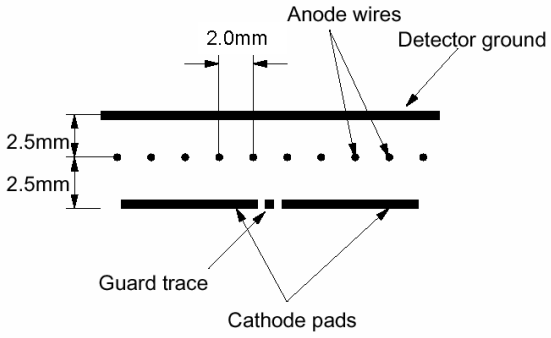

Figure 2.6: Schematic view of one sensitive gap in a MWPC.

Parameter	Design value
No. of gaps	4
Gap size	5 mm
Anode-Cathode distance	2.5 mm
Wire Diameter	30 μm
Wire pitch	2 mm
Wire tension	70 g
Gas mixture	$Ar/CO_2/CF_4$ (40/50/10)
Primary ionisation	$\simeq 10\,e^-$/mm
Gas Gain	$\simeq 10^5$
Threshold	> 5 fC

Table 2.2: Main LHCb MWPC parameters.

Chambers are readout in different way, depending on their position in the muon system:

- In region R4 of all the five stations, the chambers have anode-wire readout through decoupling capacitors;
- In region R3 of all the five stations and in regions R1 and R2 of stations M4 and M5 cathode pads are readout;
- In regions R1 of stations M2 and M3 and in regions R2 of stations M1 – M3 a combined readout of wire and cathode pads is used.

Anode wires are grouped into vertical strips to measure x whereas the y coordinates are provided by the granularity of the horizontal cathode pads.
Wires are grouped in pads of 4 to 42 to match the required granularity, varying from 6 mm in region R1 of station M2 to 62 mm in region R2 of station M5. The Muon system requires 864 MWPC chambers, with $\simeq 2.5\times10^6$ wires and about 80,000 front-end channels.

Five centers are foreseen to produce the whole MWPC chambers: one in S.Petersburg's Nuclear Physics Institute (PNPI), three in Italy (Ferrara, Firenze and Laboratori Nazionali di Frascati) and one at CERN. These centers have been equipped with similar tools, which are automated in order to speed up the construction and to achieved the required mechanical precision and tolerance. The details of the MWPC construction is reported in Ref. [26].

MWPC performances

An intensive programme of development work has been undertaken. Several MWPC prototypes have been constructed according to the different read-out requirement and the relative performances have been measured in various tests beam and in laboratory.
For completeness, I report some results obtained on the full size prototype with cathode-pad readout for Region 3 of Station 3 (M3R3). The chamber prototype have been built in the Laboratori Nazionali di Frascati with the final design, material and construction procedure.
The measurement have been performed at the T11 beam line at CERN PS with 3.6 GeV/c pions. In Fig. 2.7 is shown the efficiency in 20 ns window and the pad cluster size as function of the high voltages for a MWPC station. A wide working region, defined as the HV range between the onset of efficiency plateau (99%) and the HV at which the pad cluster size is under 1.2., of about $\sim$ 200 Volt, is obtained for an electronics threshold of 7 fC.

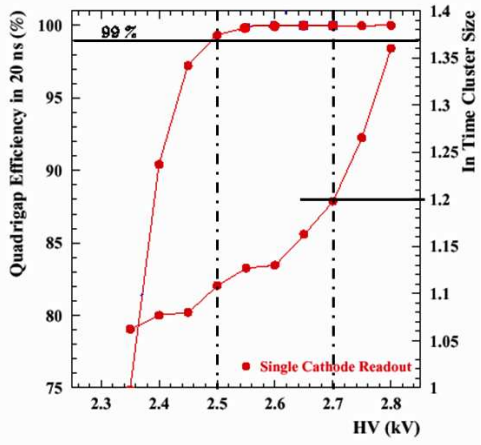

Figure 2.7: Efficiency in 20 ns time window and in-time pad cluster size as a function of the high voltage (HV) for a MWPC station [28].

Global ageing tests have been performed at the ENEA-Casaccia in the Calliope gamma facility with a ^{60}Co source. The test has been performed together with our full size triple-GEM detectors and it will be discussed in Sec. 4.4.1.
During this test the MWPC integrated $\sim$ 500 mC/cm of wire equivalent to $\sim$ 5 years of operation at LHCb experiment [29].

2.7 Electronics

The muon system front-end (FE) electronics has to prepare the information required by the L0 muon trigger as quickly as possible and must be confirm to the overall LHCb readout specifications [30]. The readout electronics chain comprises the following elements :

- *FE boards* on the chambers with amplifier, shaper, discriminator CARIOCA chips, and a CARDIAC chip to combine the output signals of the CARIOCA to form logical channels;

- *Intermediate (IM)boards* on the side of the muon system, to generate logical channels for those regions where this has not been possible on the chambers, because the logical channels are made of physical channels belonging to different chambers;

- *Off-Detector Electronics (ODE) boards*, also located on the side of the detector, where the data is synchronised and dispatched to the L0 trigger. It comprises also the L0-pipelines, L1-buffers and the DAQ interface.

Several stringent requirements must be satisfied by the FE electronics, in particular by the CARIOCA chips [31], which requirements are summarized in Table 2.3.

Parameter	Specification
Maximum signal rate	1 MHz
Maximum total dose	1 MRad
Peaking time	$\sim$ 15 ns (C_{det}=250 pF)
Input resistance	$< 50\,\Omega$
Average pulse width	< 50 ns (CARIOCA output)
ENC (r.m.s) for the positive amplifier	1880e^-+45$e^-\times C_{det}$ (pF)
ENC (r.m.s) for the negative amplifier	2240e^-+42$e^-\times C_{det}$ (pF)
Sensitivity	$\sim$ 16 mV/fC

Table 2.3: Front-end CARIOCA chip parameters [31].

Chapter 3

The Gas Electron Multiplier

3.1 Introduction

Forty years ago, the invention of the Multi-Wire Proportional Chamber (MWPC) by Charpak [32] radically changed the particle detectors field. With its good position accuracy and rate capability, and the possibility to electronically record signals generated by the transition of the particle in the detection medium, the MWPC became the ”ancestor” of many other modern gaseous particle detectors, such as drift and time projection chambers used as trackers in high energy experiments. Moreover, their use has been extended from high energy particle physics into several fields, such as astro-particle physics and medical applications.

Nevertheless, with the coming of new high luminosity colliders, the MWPC has shown some limitations concerning the capacity to tolerate the very high radiation fluxes foreseen.

The rate capability in wire detectors is due to the low drift of ions from the anode wire towards the cathode. In fact at high particle flux the ion cloud, generated around the wire, creates a positive space charge that reduces the electric field near the wire, with a consequent rate dependent gain drop, leading to an efficiency loss. For a MWPC the maximum rate capability, depending on the detector geometry (wire pitch, anode-cathode wire distance), is generally below 1 MHz/cm^2 [33].

To improve the rate capability, that is to drain ions, the anode wire spacing and/or the anode-cathode gap can be reduced, thus avoiding the space charge buildup around the anode wires. However, below 1 mm wire spacing and below 2 mm anode-cathode gap, the MWPC becomes difficult to operate because of electrostatic instabilities arising from the mechanical

tolerances.

The micro-pattern detectors, a new class of gas detectors, where the distance between anode and cathode is typically of the order of 100 μm or less, allow to overcome the rate capability problem of the MWPC.
The first example of the micro-pattern detector was the Micro-Strip Gas Chamber (MSGC) [34], introduced by Oed in 1988 and extensively developed by other authors in the following years [35]. The new device improved the rate capability and the position accuracy by more than one order of magnitude. The detector geometry is shown in Fig. 3.1: the anode and the

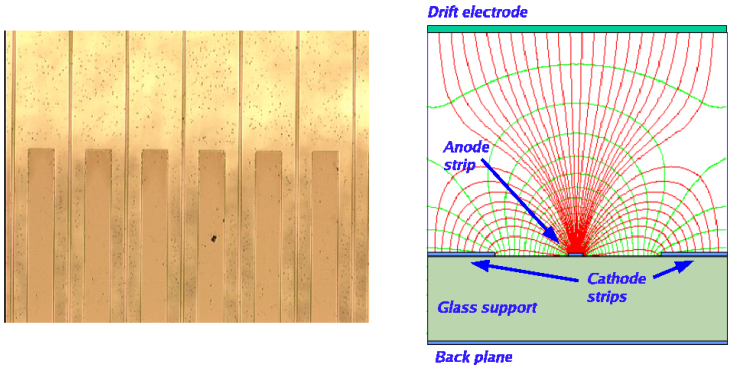

Figure 3.1: Micro Strip Gas Chamber: left) photo of the anode and cathode strips; right) sketch of the detector.

cathode are thin metallic strips which are placed on an insulating support. The upper electrode, called drift electrode, is used to define the drift region. A further electrode behind the insulating support, the back-plane, can be segmented as orthogonal strips giving the second coordinate.
The strips, alternatively connected to positive and negative voltage, act as a multi-anode proportional counter. The electrons, produced by the radiation crossing the detector in the drift region, move towards the anode strips where they are multiplied. The ions produced in the avalanche are mainly collected in the neighbouring cathode strips typically 100 μm distant from the anode.
Standard photolithography technology allows to produce 0.3$\div$0.5 μm thick cathode and anode strips with 100 μm of pitch. The manufacturing process is the same used for the production of multi-layer printed boards.

Operating instabilities were observed in the early device due to the charging-up of the insulating support. In fact when high particle flux crosses the detector, a part of the multiplication ions could be collected on the insulating support. This accumulated charge produces a change of the electric field between the strips changing the detector gain. This effect, which is rate dependent, could be reduced or eliminated using slightly conducting supports [36], and rate capability up to 100 MHz/cm^2 could be achieved [37].

Developed by many groups, MSGCs appeared however rather susceptible to aging and discharge damages. Long-term studies have shown a slow degradation of performances, attributed to the formation of polymers in the avalanche. Anyway, with the proper choice of the components, as gas mixture and detector materials, a long-term survival up to collected charge above 100 mC per cm of strip equivalent to about ten years of operation at LHC has been demonstrated [38].

The appearance of destructive discharges appeared instead to be a more serious problem. In fact, a transition from avalanche to streamer, which is gas gain and ionization density dependent, could easily followed by a discharge due to the short distance of the electrodes. The discharge could heavily damage the strips incrementing with the time the dead channels. This limitation is particular apparent in the new luminosity colliders, where among the particles to be detected, rare but heavily ionizing tracks (nuclear fragments, gamma and neutron conversions) are present. Thus a gain arrangement, that allows at the same time the detection of minimum ionization particles (m.i.p.) excluding the damage produced by the crossing of heavily ionizing particles, could not be possible [1].

Motivated by the problems mentioned above, a great effort has been made to find a more rugged alternative detector to the MSGC. In fact in the following years many of such detectors have been invented (Fig. 3.2): the microgap chamber (MGC) [39], the Microdot [40], the "Compteur $\grave{a}$ Trous" (CAT) [41], the Micromesh gas chamber (MicroMeGas) [42], the Micro-Groove [43] and the WELL [44] detectors.

Among the micro-pattern detectors the *Gas Electron Multiplier* (GEM) [45], proposed in the 1997 by Sauli, represents the object of my Ph.D thesis.

With respect to the other micro-pattern detectors, in the GEM structure the conversion, the multiplication and the signal induction regions are physically distinct resulting in greater

[1] Comment of the referee, Prof. R. Bellazzini: "It is possible to find a gain setting in order to keep high efficiency for m.i.p. while reducing the discharge probability in a heavily ionizing particles environment (NIM A 457 (2001) 22)".

freedom in the readout geometry. Moreover, the possibility to divide the multiplication in more steps allows to drastically reduce the problem of discharge and the ageing processes.

To fulfill the M1R1 requirements of the LHCb experiment and to assure a safe operation mode in such a harsh environment, we choose to adopt a triple-GEM structure.
The use of this type of detector as a triggering device is certainly a novelty in the field of high energy physics. The first application of GEM detectors in high energy physics is the COMPASS experiment, where they are currently used as a tracking device.
However, little interest was devoted so far to the optimization of the time performance of GEM detectors, while at LHC, a critical issue is the high efficiency in the bunch-crossing identification, which require a high detector time resolution.
Because the typical detector time resolution with an Ar/CO_2 (70/30) gas mixture is about 10 ns r.m.s [46], an intense R&D activity on GEM detectors for the Level 0 LHCb muon trigger has been performed by our group in order to improve this limit.

After a general description of the GEM idea (Sec. 3.2), in Sec. 3.3 the principle of operation of a single GEM detector is presented. These two sections allow to introduce the parameters which play an important role in the time performance of the detector.
Our optimization of a triple-GEM detector for triggering purpose, as needed in the LHCb experiment, is presented in Sec. 3.4, Sec. 3.5 and Sec. 3.6, where the role of the electric fields, gaps geometry, the gas mixture and signal formation are discussed.
In conclusion, the global performances (gas gain, rate capability, efficiency in 20 ns time window, discharge probability and ageing tests) of the triple-GEM detector are shown in Sec. 3.7.

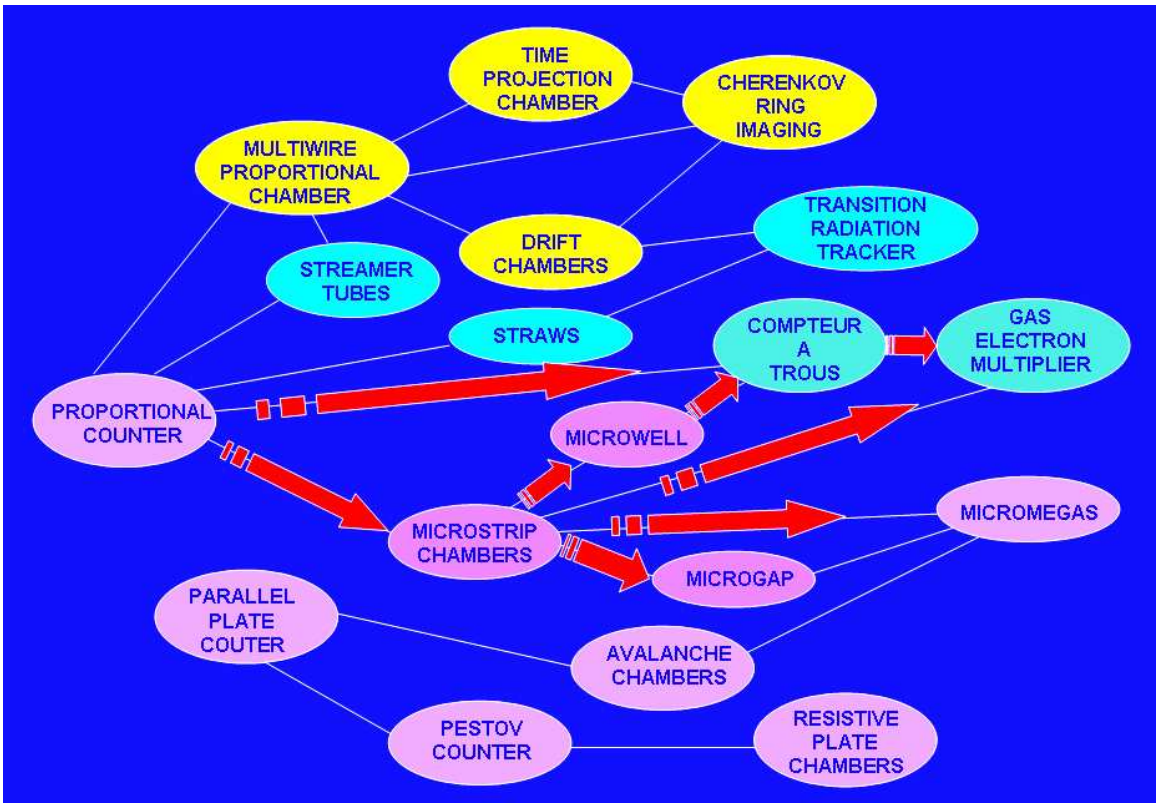

Figure 3.2: The gas detector family tree.

3.2 The GEM idea

The Gas Electron Multiplier (GEM) is a 50μm thick insulating kapton foil, clad on each side with a thin copper layer (5μm) and chemically perforated with a high density of holes. The holes have a bi-conical structure with an external diameter of 70 μm and internal of 50 μm and a pitch of 140 μm [47] (Fig. 3.3).

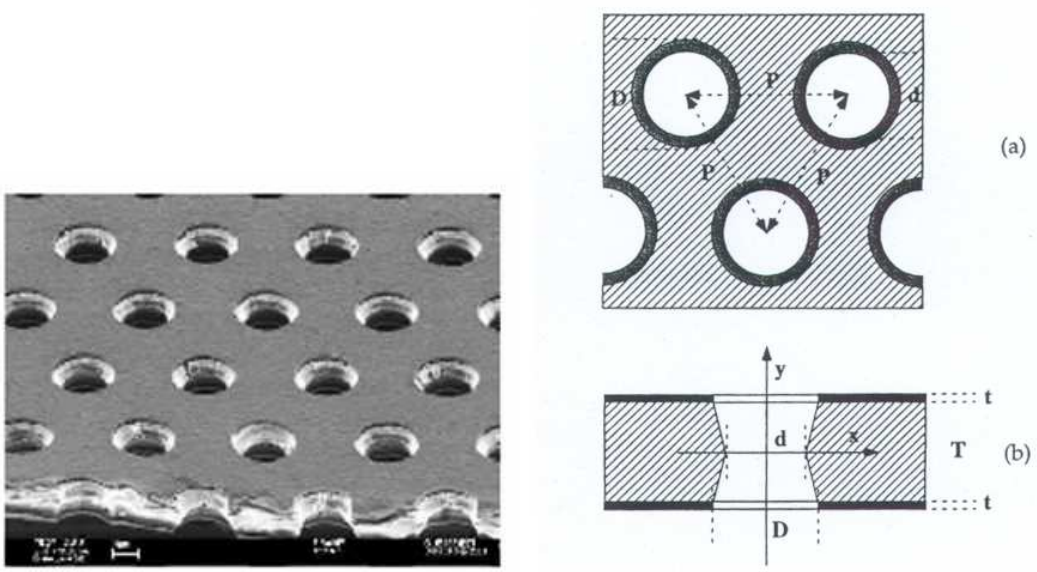

(a) GEM foil as seen at the electron microscope.

(b) Cross section of the geometry of GEM foil and the bi-conical shape of the holes.

Figure 3.3: The GEM foil

In a GEM detector the hole acts as a multiplication channel for the electrons released by ionizing radiation in the gas mixture. Applying a suitable voltage difference (300÷500 V) between the two metal sides, a high electric field ($\sim$ 100 kV/cm) is generated inside the holes. In this region, an electron could acquire enough energy to develop an avalanche. The reachable gain with a single GEM can be greater than 10^3.

The GEM manufacturing technology is realized using conventional photolithography methods [48].

The process starts with the production of two identical masks, whose pattern is transferred to the photo-resist coated foils by exposure to UV light. For such large size, a crucial parameter is the precise alignment of the two masks. Indeed, since the patterned copper layer is used as a mask during the chemical process of the kapton etching, any misalignment between the two masks results in slanted holes, yielding lower gain. This is a particularly difficult requirement due to the use of plastic masks that can deform under thermal stress. The shape of the holes is successively obtained by the immersion of the patterned foil in a solvent. The GEM manufacturing processes is summarized in Fig. 3.4.

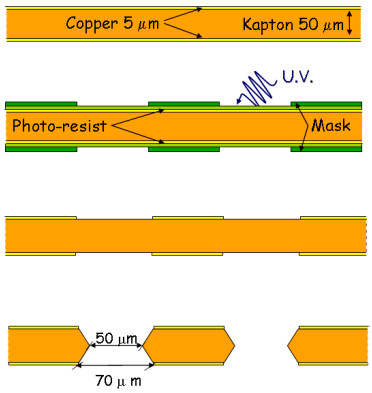

Figure 3.4: GEM manufacturing technology. From the top: commercially available kapton foil; the double mask alignment and the photolithographic process; copper etching by chemical solution; kapton etching using the copper layers as masks.

The choice of the geometrical parameters of a GEM foil, as the hole diameter, the pitch and the hole shape, and the manufacturing technique are a compromise between production yield [2] and safe operation of the detector [50].

3.2.1 Influence of hole diameter

In order to achieve a higher gain, the field lines density in the amplification channel can be increased by raising the voltage difference between the upper and lower GEM electrodes, or by reducing the hole diameter. Fig. 3.5 shows the correlations between the effective GEM

[2] At present, different techniques, based on laser and plasma etching methods [49], have been used for GEM manufacture. Using these techniques, the production of the holes is more complex and slower than the chemical one. Moreover, these methods could produce local defects, such as the creation of metal "bridges" inside the hole which compromise the GEM operation.

gain and the hole diameter, measured at equal gas mixture and electric fields conditions. A gain saturation effect is observed for hole diameter below $\sim$ 70 μm which, as will be discussed in Sec. 3.3.3, is due to the increasing losses of electrons in the avalanche (due to diffusion) to the lower GEM electrode. The saturation effect, whilst limiting the possible gain enhancement, has the very positive effect of reducing substantially the dependence of the detector gain from the precision of the GEM manufacturing process.

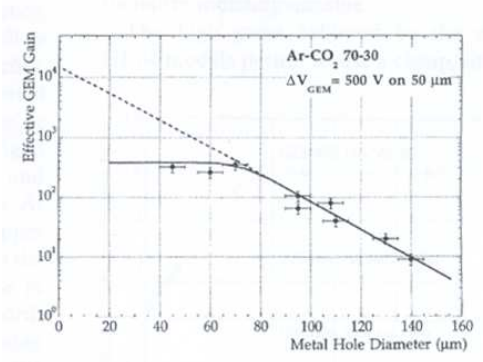

Figure 3.5: Measured effective gain of GEMs in Ar/CO_2 (70/30) with different metal hole diameters. The exponential fit to the points extrapolated to the expected gain for a 50 μm thick parallel plate geometry deduced from the known value of the Townsend coefficient [50].

3.2.2 Influence of hole pitch

The hole pitch does not play a direct role on the gain behavior, but when combined with the hole diameter, affect the *collection efficiency* of the electrons released in the upper volume of the GEM foil into the holes. The *collection efficiency* is correlated with the so called *electron transparency* [3]; as will be discussed in the Sec. 3.3.3, it gives a measure of the electrons losses crossing a hole due to different effects, and plays an important role in the detector performances.
At this level, it is possible to deduce that a high *collection efficiency* is achieved with a small pitch, as shown in Fig. 3.6.

[3] At this point, the concept of the electron transparency can be understood through the optical transparency. The latter is defined as the ratio between the total area of holes and the total area of the foil: $t=\pi D^2/2\sqrt{3}P^2$ where D is the external diameter and P the pitch and a cylindric shape of the hole is assumed. A higher optic transparency is achieved by reducing the pitch value at a fixed hole diameter.

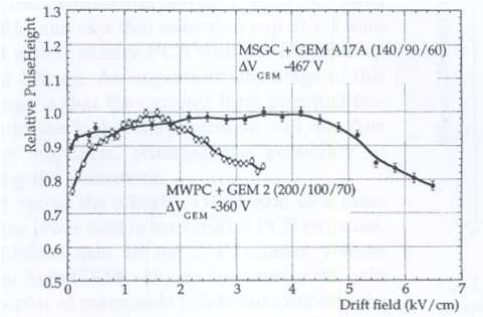

Figure 3.6: *Collection efficiency* as a function of drift field in a GEM of 140 μm pitch and 90 μm holes and a GEM of 200 μm pitch and 100 μm holes [50].

3.2.3 Influence of hole shape

The hole shape affects the *charging-up*, a short-term rate-dependent instability of the electrode resulting as a small increase of the gain due to the presence of the kapton insulating close to the multiplication channels. In fact, the electrons and the ions from the avalanche, collected and accumulated on the insulating kapton surface, produce an alteration of the electric field inside the multiplication channel. The hole geometry which best minimizes this effect is the cylindric shape, as shown in Fig. 3.7.
On the other hand, the choice of a bi-conical shape is a compromise between a good production yield [4] and the limited charging-up effect with respect to the conic shape [50].

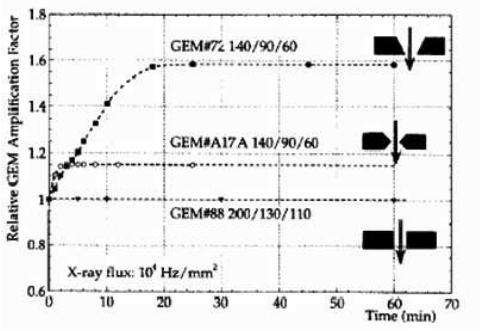

Figure 3.7: Time dependence of the gain for several hole shapes under a particle rate of 10^4 Hz/mm^2 [50].

[4] As previously described, the shape of the holes is obtained by immersion of the patterned foil in a solvent. The hole shape evolves, depending on the etching time, from double-conical to cylindric-like geometry. Although a cylindric shape would be the more desirable geometry, it was found that, probably due to non-uniformities in the kapton, local defects can be created, such as metal "bridge", reducing the production yield.

3.3 The single GEM detector

The most simple gas detector based on GEM technology is the single-GEM detector [51], where one GEM foil is sandwiched between two flat parallel electrodes. The upper electrode plays the role of cathode while the lower one as anode.
The cross section of a single-GEM detector is shown in Fig. 3.8, together with the labelling of the different detector parameters.

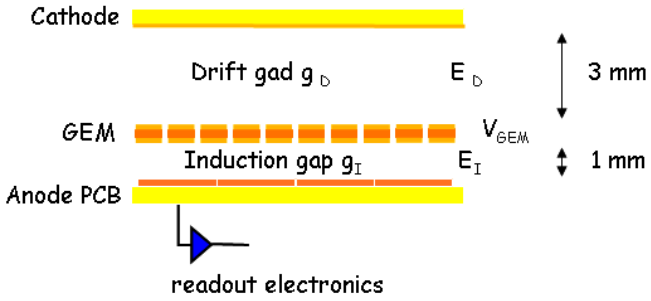

Figure 3.8: Cross section of a single GEM detector: E_D and E_I are the drift and the induction fields, while g_D, g_I are the drift and induction gaps; V_{GEM} is the voltage difference applied to the two copper layers of the GEM foil.

The drift field, E_d, is generated between the upper side of the GEM foil and the cathode, while the induction field, E_I, between the lower side of the GEM foil and the anode (PCB). The relative regions are called drift and induction gaps.

The ionization electrons, produced in the drift gap by the charged particle crossing the detector, following the drift lines move towards GEM holes where they are multiplied.
Some of the electrons from the multiplication are collected on the lower side of the GEM foil. The most of the multiplication electrons are transferred in the induction region, giving rise to an induced current signal on the anode. Typically the fraction of multiplied electrons that are transferred in the induction region is $\sim$ 50% and this fraction depends on the electric field inside the hole and electric field below the GEM (Fig. 3.9).
The multiplication ions are mainly collected on the upper side of the GEM foil instead of drifting towards the cathode leaving the GEM hole from charges in a relatively short time (few μs).

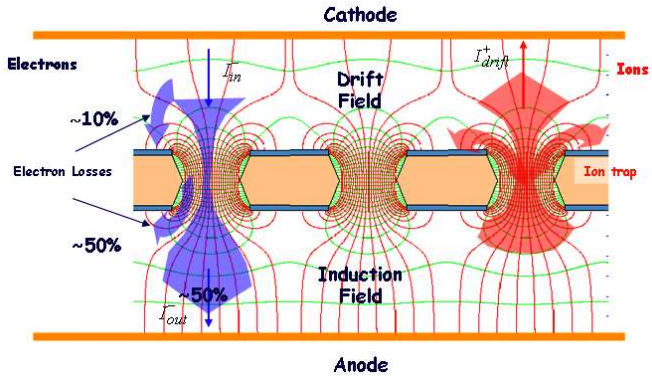

Figure 3.9: Qualitative scheme (not in scale) of a single-GEM detector operation together with the 2D map of electric field lines (red) and equipotential lines (green) in proximity of the GEM holes.

Generally, the read-out is a simple and cheap printed circuit boards (PCB): the structure of the readout can be easily adapted to experimental needs, using strips or pads of arbitrary shapes connected to the front-end electronics (Fig. 3.10). Since the read-out is kept at ground potential, considerable simplification of the front-end electronics is also achieved.

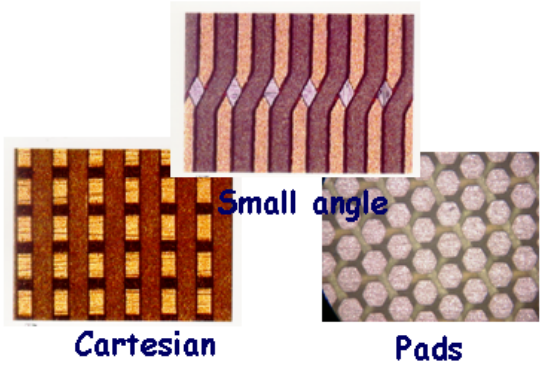

Figure 3.10: Various readouts used with a GEM based detector.

As mentioned above, the induced signal is purely due to the motion of the electrons in the induction gap. Taking into account the high electron mobility, the induced signal is fast and not affected by the ion tail typical of the wire chamber [33].

The parameters of a single-GEM detector, with defined GEM foil geometry and gas mixture, are:

- the electric fields in the drift and the induction gap;
- the thickness of the drift and the induction region;
- the voltage difference applied to the GEM foil.

3.3.1 The gap electric fields

The study of the electric fields of a GEM detector, in various geometries and conditions, is performed with MAXWELL [52] [5] and GARFIELD [53] [6] simulation tools. The field lines in the drift and induction gaps are similar to those of a parallel capacitor with an increasing density close to the holes, as shown in Fig. 3.9.

The drift field

The purpose of the drift field is to collect the primary electrons, produced by the ionization particles in the gap, into the GEM holes. Fig. 3.11 shows a comparison of relative signal amplitude as a function of the drift field, deduced from a measurement of current and from pulse height with two shaping times (100 ns and 1 μs) [51].

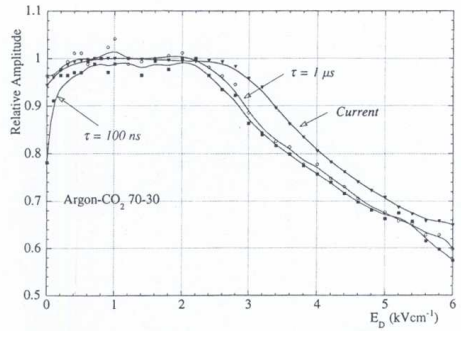

Figure 3.11: Relative signal amplitude on the PCB as a function of the drift field [51].

[5] The Maxwell tool is an engineering program. It allows to construct the 3D geometry of a detector, the so called "cell", taking into account all the detector material properties.

[6] The Garfield program is the common framework used for the simulation of gas detectors.

At low field values (<0.5 kV/cm), the curves drop due to a low electron drift velocity and large diffusion. At intermediate value ($\sim 1 \div 3$ kV/cm), the signals reaches a plateau and decrease again for higher value of drift field. The latter effect is due to the defocusing effect [54] of field-lines above the GEM, which leads the primary electrons to be directly collected on the upper electrode of the GEM.
The above dispersive effects are correlated to the so-called *collection efficiency* which will be discussed in detail in Sec. 3.3.3.

For a given gas mixture and GEM foil geometry, the value of the drift field is chosen in order to optimize the *collection efficiency*. In $Ar/C0_2$ (70/30) gas mixture the typical value of the drift field is 2 kV/cm [51].

The induction field

The task of the induction field is to extract the multiplied electrons from the GEM holes and to transfer them towards the anode.
Fig 3.12 shows the electron current induced on the bottom electrode of the GEM (I_B) and on the pad (I_S), together with the sum (I_{TOT}), as a function of the induction field [51]. The drift field was set to 1 kV/cm to ensure full *collection efficiency* in GEM holes.

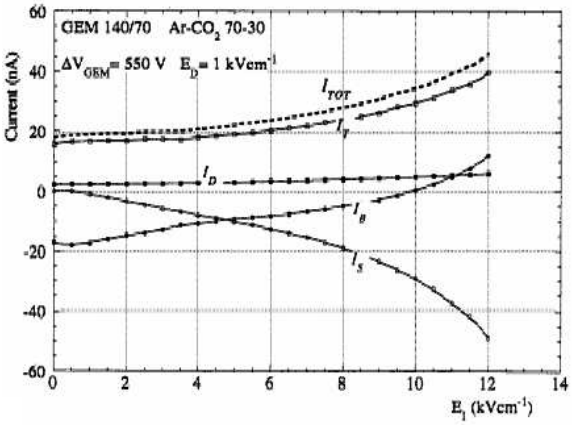

Figure 3.12: Currents on the various electrodes of a single-GEM detector as a function of the induction field: I_S current on the pad, I_B and I_T current on the bottom and upper layer of the GEM, and I_D current of the cathode [51].

At very low value of the induction field all the secondary electrons, extracted from the GEM holes, are practically collected on the bottom GEM electrode and the induced signal is vanishing (Ramo-theorem). By incrementing the induction field, the secondary electrons begin to be collected on the readout electrode, increasing I_S and decreasing I_B.
At very high induction field, $E_I > 8$ kV/cm, discharges on the anode can occur due to the high electric field in proximity of the readout electrode edges.
Independently by the gas mixture used, a value of the induction field of ~ 5 kV/cm is a reasonable compromise and allows to collect a large fraction (50%) of the charge on PCB.

3.3.2 The gap thickness

The drift gap

The geometry of this gap has to be chosen in order to ensure a high particle detection efficiency. For a charged track, the number of electrons clusters created has a Poisson distribution with an average value $\overline{n}$ depending on the particle energy and the gas mixture used. For any reasonable choice of the gas mixture, a 3 mm wide gap guarantees the full efficiency of the detector.
A wider drift gap should essentially leave the detector efficiency unchanged, while it can increase the pile-up effects at very high particle rate as well as the ageing rate. In fact, the charge integrated by the detector obviously linearly depends on the value of the primary electrons released in the drift gap.

The induction gap

The induction gap is typically 1 mm thick in order to maximize the signal fraction integrated by the amplifier. As will be discussed in Sec. 3.6, the GEM signal amplitude is proportional to the ratio between the electron drift velocity and the thickness of the induction gap.
This consideration suggests both the use of a fast gas mixture and a small thickness for the induction gap. However, a sub-millimetric gap is not advised because it would require a high mechanical tolerance in order to avoid discharges on the PCB, and gain disuniformity of detector.

3.3.3 The GEM voltage

The voltage, V_{GEM}, applied to the two metal sides of the GEM foil develops a high electric field inside the holes, and the *intrinsic* gain of the GEM foil directly depends on the V_{GEM}:

$$G_{intrinsic} \propto e^{<\alpha>V_{GEM}} \tag{3.1}$$

where $< \alpha >$ is the average of the first Townsend coefficient [55] along the electron path through the hole. This coefficient is gas mixture and electric field dependent [7].
Generally, the *intrinsic* gain of a single-GEM detector can reach value of the order of 10^3.
As mentioned in the Sec. 3.3.1, there are dispersive effects that decrease the number of the effective electrons transferred on the anode. Consequently, the resulting *effective* gain is smaller than the *intrinsic* one.
These dispersive effects are correlated with the value of the electric fields above and below the GEM and the voltage V_{GEM}.

For a GEM-based detector it is possible to define the following quantity:

1. *collection efficiency* (ϵ^{coll}):

$$\epsilon^{coll} = \frac{electrons\ collected\ in\ the\ holes}{electrons\ produced\ above\ the\ holes} \tag{3.2}$$

   represents the ratio between the number of electrons entering the multiplication channels and the number of primary electrons generated above the GEM.
   The *collection efficiency* is generally a function of the electric field above the GEM and the electric field inside the hole.
   Simulation studies have shown that primary electrons are lost either because they are collected on the upper GEM electrode (defocusing effect [54]) or they hit the kapton surface inside the hole before starting the multiplication (Fig. 3.13, 3.14).
   As already shown in Fig. 3.11, this effect could be in general reduced decreasing the drift field or increasing the electric field inside the hole.
   In case of electronegative gas mixtures, additional primary electrons losses can occur before the multiplication due to the recombination effects. For example, for our gas mixture, $Ar/CO_2/CF_4$ (45/15/40), the electric field in the proximity of the hole ($\sim$ 10

[7] The rigorous formula of the intrinsic gain is: G=exp($\int[\alpha(x) - \eta(x)]\delta$x), where α and η are respectively the first Townsend and the attachment coefficient in the path δx. Both of these coefficients are field and gas mixture dependent. Due to the high value of the field inside the hole (100 kV/cm), the attachment coefficient becomes negligible and the previous formula reaches the Eq. 3.1.

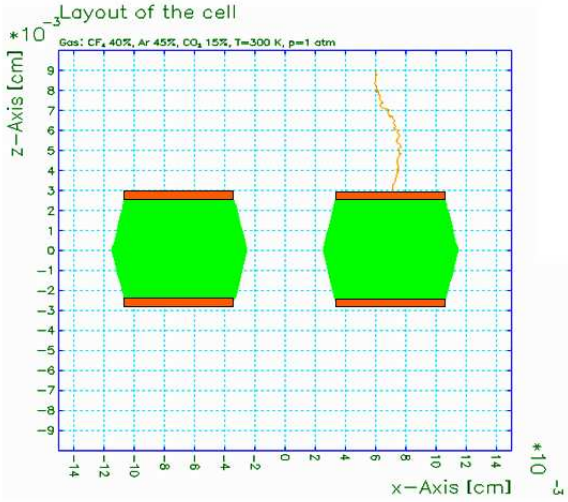

Figure 3.13: Primary electron collection on the upper GEM electrode.

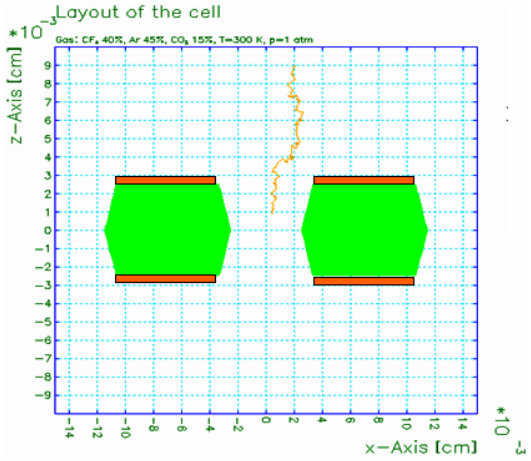

Figure 3.14: Primary electron capture before the multiplication.

kV/cm) can allows for a recombination of the primary electrons due to a high electron attachment with respect to the Townsend coefficient (Fig.3.15).
For the $Ar/CO_2/CF_4$ (45/15/40) gas mixture, the defocusing effect and the capture on the kapton are of the order of 20% and 5% respectively, while the electron attachment is about 10%, giving a global *collection efficiency* of $\sim$ 65%.

2. *extraction fraction* (f^{extr}):

$$f^{extr} = \frac{electrons\ extracted\ from\ the\ holes}{electrons\ produced\ in\ the\ holes} \tag{3.3}$$

this quantity represents the ratio between the number of electrons extracted from the holes and transferred to the PCB and the number of electrons multiplied inside the amplification channels.
The extraction fraction is a function of the electric field inside the hole and the electric field below the GEM.
The simulation studies, Fig 3.16, have shown that $\sim$ 3% of the multiplication electrons are trapped at the hole surface due to the diffusion, $\sim$ 10% are ion captured in proximity of the hole exit. The remaining multiplication electrons, coming out from the hole, are either collected on the bottom electrode of the GEM or transferred to the induction

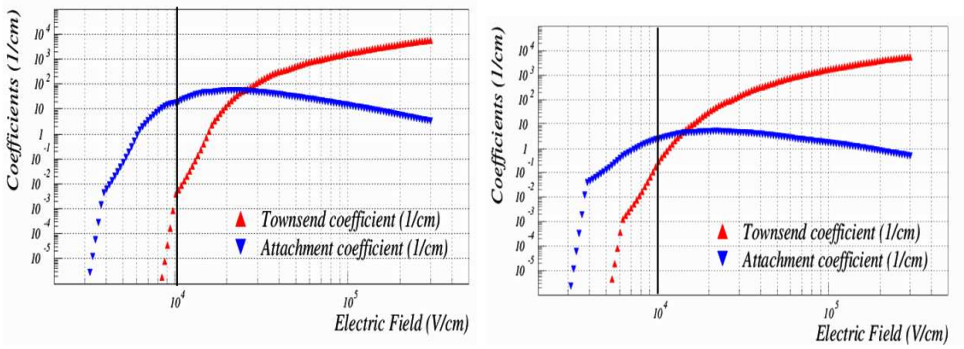

(a) For the Ar/CO_2 (70/30) gas mixture.

(b) For the $Ar/CO_2/CF_4$(45/15/40) gas mixture.

Figure 3.15: Townsend and electron attachment coefficients as a function of the electric field simulated with Imonte. The black line represents the value of the electric field in proximity of both the entrance and the exit of the hole.

region. As discussed in the previous section, the induction field is set at 5 kV/cm to assure a safe detector operation. In this case a fraction of $\sim$ 50% of multiplication electrons are lost on the bottom electrode of the GEM foil and the other 50% goes towards the readout electrode. A total *extraction fraction* of about 35% is obtained.

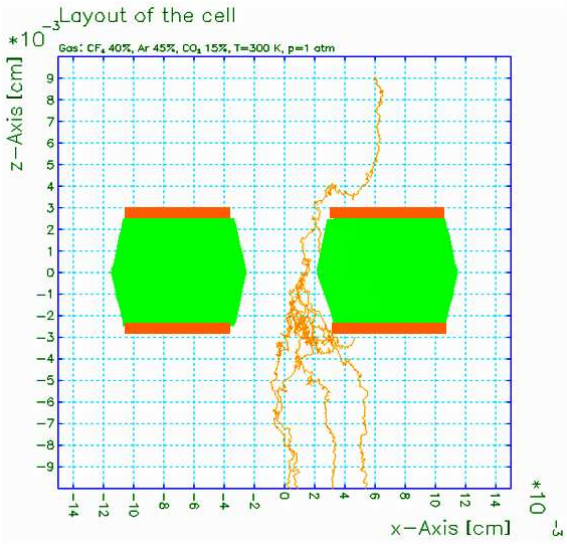

Figure 3.16: The trapping on the kapton surface and the collection on the GEM bottom side of the multiplication electrons.

The definition of the *collection efficiency* and *extraction fraction* allows to introduce the concept of the *effective* gain, G_{eff}, correlated with the *intrinsic* gain of a GEM foil, G_{intr} through the following relation:

$$G_{eff} = G_{intr} \cdot T = G_{intr} \cdot \epsilon^{coll} \cdot f^{extr} \tag{3.4}$$

where we define the *electron transparency* T of the single-GEM detector as the product of $\epsilon^{coll} \cdot f^{extr}$.

The maximum effective gain reachable with a single-GEM detector is of the order of 10^3. Higher gas gain, up to $10^4 \div 10^5$, can be achieved assembling more than one GEM foil in cascade at close distance one to each other.

3.4 The triple-GEM detector

A triple-GEM detector consists of three GEM foils piled-up and sandwiched between two electrodes, a cathode and an anode. The use of three GEM foils allows to reach higher detector gain before the appearance of discharges, without requiring too high voltage applied to each single GEM foil (Fig. 3.17) [8].

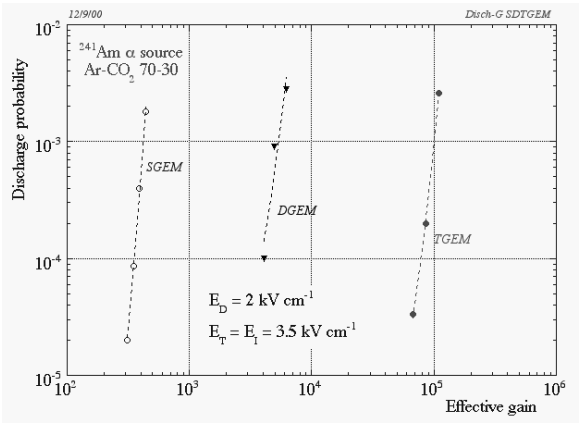

Figure 3.17: Discharge probability as a function of the gas gain for a single, double and triple GEM detectors in Ar/C0$_2$ (70/30) gas mixture [51].

A cross section of a triple-GEM detector, together with the labelling defining the geometrical and electrical parameters, is shown in Fig. 3.18. The voltage difference applied to the various GEM foils are called (from the top to the bottom) V_{GEM1}, V_{GEM2}, V_{GEM3}, and their sum V^{tot}_{GEM}.

The description of the single-GEM chamber, discussed in the previous section, allows to understand the operation of a triple-GEM detector. The gap between the cathode and the first GEM foil acts as conversion and drift region.
The gap between the last GEM foil and the anode is the induction region where, after the multiplication, in this case due to the three GEM foils, the charge induces the signal on the anode PCB.

[8] Clarification required by the referee, Prof. R. Bellazzini: the discharge effect in a gas detector is correlated to the charge density in the avalanche and then to the total gain of the detector. For a triple-GEM detector the charge, which arrive to the third amplification step, is spread over more holes due to the diffusion through previous gaps, thus reducing the discharge probability with respect to a single-GEM detector operating at the same gas gain. This effect is discussed and measured in our work (NIM A 513 (2003) 264).

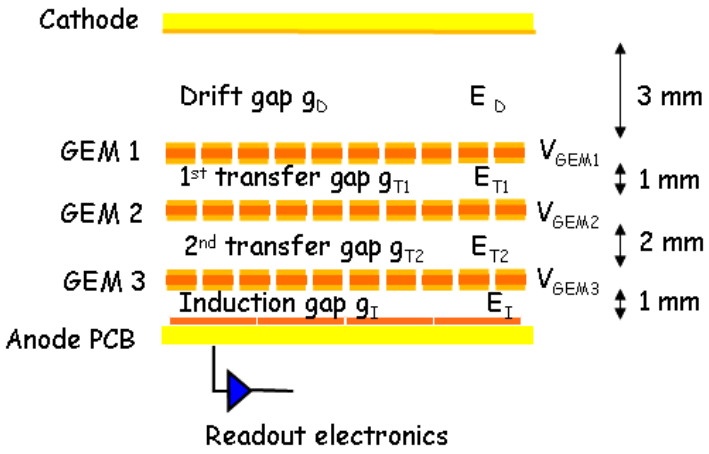

Figure 3.18: Cross section of the triple-GEM detector. E_D, E_{T1}, $E_{T2}$and E_I are the drift, the first and the second transfer and the induction fields respectively; g_D, g_{T1}, g_{T2} and g_I are the drift, the two transfer and the induction gaps respectively.

For the electric fields and geometrical thickness of these gaps, the same considerations done for the single-GEM detector are valid.
The other two gaps, between two consecutive GEM foils, are called transfer regions. They act as an induction region if they are referred to the above GEM, while as a drift region if they are referred to the GEM below. Thus the choice of the transfer fields and the relative thickness requires for additional considerations.

3.4.1 The transfer electric field

The purpose of the transfer field is to transport the secondary electrons produced in the holes of the above GEM and to collect them in the holes of the next GEM. This means that the value of the transfer field must be chosen in order to maximize at the same time the *extraction fraction* from the upper GEM and the *collection efficiency* to the lower GEM (Sec. 3.3.3).
Fig. 3.19 shows the induced current on the electrode readout as a function of the transfer fields for the Ar/C0$_2$ (80/20) gas mixture for a given value of drift and induction fields (E_D= 2 kV/cm, E_I= 5 kV/cm).

At low value of the transfer field ($E_T < 3$ kV/cm), the electron current is affected by a low *extraction fraction*. In fact, the multiplication electrons are extracted by the upper GEM

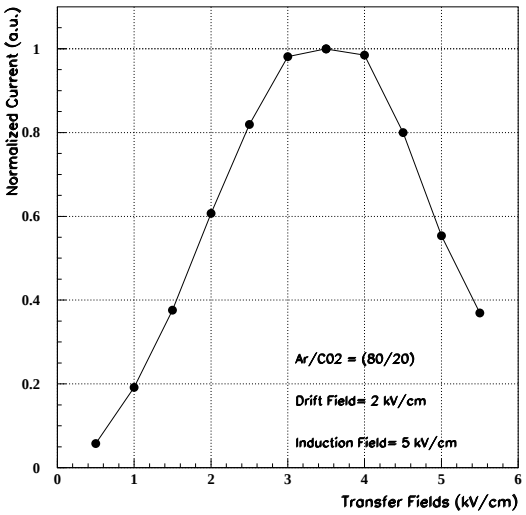

Figure 3.19: Induced current on the readout electrode as a function of the transfer field (E_{T1}=E_{T2}) for the Ar/$C0_2$ (80/20) gas mixture.

holes but they are mainly collected on the bottom electrode of that GEM.
On the other hand, a high transfer field ($E_T > 4$ kV/cm) imply a poor *collection efficiency* due to a high defocusing effect. Indeed, the multiplication electrons, coming from the above GEM, are mainly collected on the upper electrode of the successive GEM.
For an Ar/$C0_2$ (80/30) gas mixture, a typical value for both transfer fields is in the range of 3÷4 kV/cm.

3.4.2 The transfer gap thickness

In order to improve the time performance of the detector and to keep the discharge probability as low as possible, several tests were performed for different size of the transfer gaps, using the following detector geometry (g_D/g_{T1}/g_{T2}/g_I): 3/2/2/1, 3/1/2/1 and 3/1/1/1.
The results of these tests are discussed in the next sections.

The first transfer gap

As a charged particle crosses the detector, the gas ionization occurs in each gaps of the detector. The main difference between the primary electrons produced in the various gaps is the number of multiplication steps that they undergo along their drift towards the anode: the

electrons produced in the drift gap pass through the three multiplication steps, while those generated in the first transfer gap cross only two GEM foils.
Due to statistical fluctuations of the total ionization and the gas gain, the ionization produced in the first transfer gap, and multiplied by the last two GEM, can induce a signal large enough to be discriminated by the front-end electronics. This signal, depending on the drift velocity of the gas mixture and the gap thickness, will be anticipated, with respect to the signal produced by the electron coming from the drift gap, of the quantity $\Delta t = g_t/v_{drift}$.
This effect, particularly important for the time performance of the detector, has been called *bi-GEM* effect [56].
Fig. 3.20 shows the time spectrum obtained with the $Ar/C0_2/CF_4$ (60/20/20) gas mixture for 1 and 2 mm first transfer gap thickness.
For an electric field of 3 kV/cm, the electron drift velocity of this gas mixture is about 100 μm/ns. With a 2 mm gap (black distribution), the time spectrum is characterized by the presence of small amplitude events in advance of $\sim$ 20 ns with respect to the main signal, broadening the distribution. A 5% of the total number of events are represented by *bi-GEM* events.
Viceversa with a 1 mm thickness (red distribution) the anticipated signals, in this case in advance of $\sim$ 10 ns with respect to the main signal, are practically disappeared, being reabsorbed by the global fluctuations of the arrival time of the electrons. In this case, the *bi-GEM* events are less than 2% of the total.

This result suggests that the thickness of the first transfer gap has to be keep as low as possible. We set the value of g_{T1} to 1 mm.
A further reduction of the *bi-GEM* effect could be achieved by increasing the amplification on the first GEM, as will be discussed in Sec. 3.4.3.

The second transfer gap

In the second transfer gap the effects of small amplitude and anticipated signals are vanishing. In fact, the primary electrons produced in this gap are multiplied only by the last GEM, thus in a difficulty way they can give rise to a signal over the electronic threshold.
On the other hand, the thickness of this gap is correlated with the discharge probability. As will be discussed in Sec. 3.7.4, the number of electron-ion pairs could exceed the Raether limit (transition from avalanche to streamer) in the third amplification step (GEM3), and a

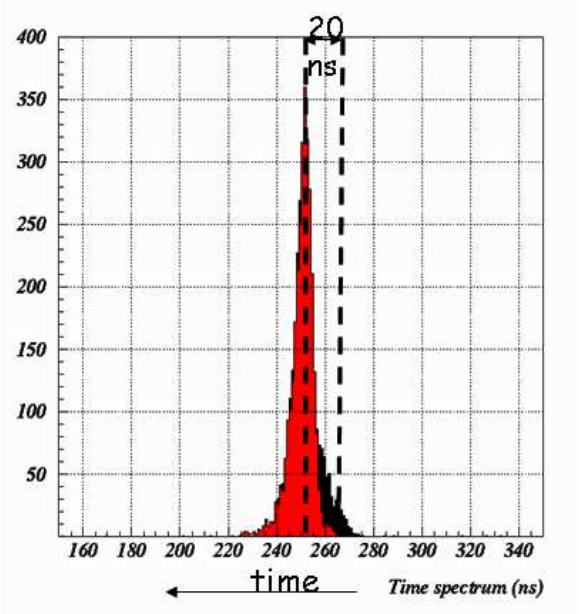

Figure 3.20: The *bi-GEM* signal for a triple-GEM detector (recorded in common stop): time spectrum for 1 mm (red) and 2 mm (black) thickness of the first transfer gap.

discharge can develop inside the hole.

For all gas detectors, the discharge effect can be minimized by adding a suitable fraction of a quencher component to the gas mixture, although the quantity and the type are limited by the degradation of the detector performance due to ageing processes.
For a triple-GEM detector using a given gas mixture, the discharge effect can be reduced by increasing the thickness of the second transfer gap. Indeed, a larger gap allows to increase the electron diffusion in that region. Since the transverse dimension of the electron clouds increases with the square root of the electron drift [33], the number of the holes involved in the multiplication process increase linearly with the thickness of a gap. Consequently, the diffusion allows the electron cloud to be spread over more than a single hole, reducing the probability of reaching the Raether limit in the third GEM (Fig. 3.21).

The measure of the discharge probability, as a function of the gas gain in the $Ar/C0_2/CF_4$ (60/20/20) gas mixtures, for two different thickness of the second transfer gap, 1 and 2 mm respectively, has been performed with an ^{241}Am (α) source [57].

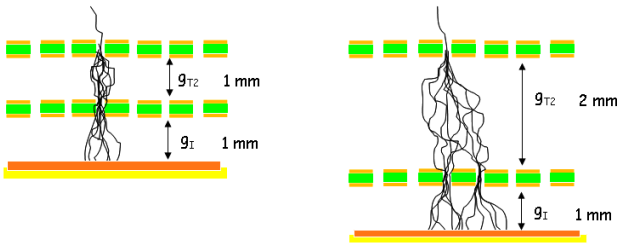

Figure 3.21: Qualitative schema of diffusion effect for different size of the transfer gap.

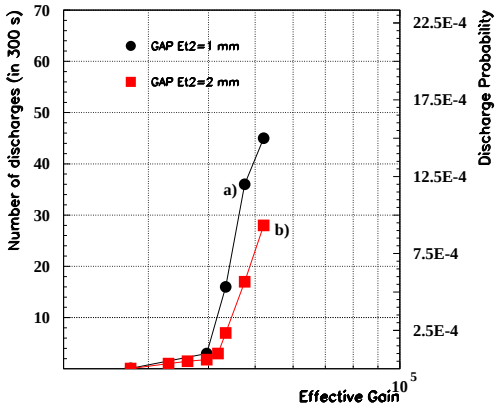

Figure 3.22: The discharge probability, performed with an ^{241}Am source, as a function of the gas gain in the Ar/$C0_2$/CF_4 (60/20/20) gas mixtures for 2 different thickness of the second transfer gap, 1 and 2 mm.

As shown in Fig. 3.22, the discharge probability for a 2 mm gap (red curve) is a factor of 2 less than that one obtained with a 1 mm gap (black curve), for a gas gain of 4.5×10^4.

Taking into account the maximum size required by the muon system for the whole detector thickness and at the same time the necessity to minimize the discharge effect, we set the value of the second transfer gap to 2 mm.

3.4.3 The GEM voltages

For a triple-GEM detector the *intrinsic* gain is an exponential function of V_{GEM}^{tot}.
Together with the electric field in the various gaps, that define the *electron transparency* T_{tot}, the *effective* gain of the detector is defined as follows:

$$G_{eff} = G_{intr} \cdot T_{tot} = \prod_{k=1}^{3} e^{<\alpha>_k \cdot V_{GEMk}} \cdot T_k = e^{<\alpha>^{tot} \cdot V_{GEM}^{tot}} \cdot \prod_{k=1}^{3} \epsilon_k^{coll} \cdot f_k^{extr} \qquad (3.5)$$

where the $<\alpha>$ is the average of the first Townsend coefficient [55] of the electron path through the hole, ϵ_k^{coll} and f_k^{extr} are the *collection efficiency* and the *extraction fraction* of the k^{th} GEM foil.

Since the effective gain depends on the voltage applied the three GEMs only through their sum, it is possible to unbalance these voltage differences in order to reduce the discharge effect in the last GEM. Indeed, at a fixed V_{GEM}^{tot}, i.e. at a fixed gain, it is convenient to increase the voltage applied on the first GEM while reducing the one applied to third GEM. In this case, the charge reached on the third GEM is greater but the diffusion effect allows the electron cloud to be spread over a larger number of holes, reducing the discharge probability.
The studies with the α source enable us to choose the GEM configuration that minimizes the discharge probability. The optimal configuration of the GEM voltages is [58]:

$$V_{GEM1} \gg V_{GEM2} \geq V_{GEM3} \tag{3.6}$$

This GEM voltage configuration, reducing the discharge effect, allows also to improve the detector time performance due to a decrease of the *bi-GEM* effect (Sec. 3.4.2). In fact, the incidental primary electrons produced along the first transfer gap will be multiplied with a lower gain with respect to the case in which the GEM voltage configuration is not unbalanced. The above GEM voltage configuration, together with 1 mm thick first transfer gap, allow to reduce the *bi-GEM* down to 1%.
At the same time, the *collection efficiency* on the first GEM can slightly increase due to a reduction of the defocusing effect.

3.5 The time performance

The main request for triggering in LHCb Muon system is to provide a high efficiency in the bunch crossing time window. Hence, besides high overall efficiency, the triple-GEM detector should ensure good time performance.

The time performance of a GEM-based detector is correlated with the statistics of the cluster [9] in the drift gap.
The general expression for the space-distribution of the cluster *j* created at distance *x* from the first GEM, is [33]:

$$A_j^{\overline{n}}(x) = \frac{x^{j-1}}{(j-1)!}\overline{n}^j e^{-\overline{n}x} \tag{3.7}$$

where $\overline{n}$ is the average number of clusters created per unit length. For a given drift velocity in the drift gap, v_d, the probability-distribution of the arrival times on the first GEM for the cluster *j* gives:

$$P_j(t_d) = A_j^{\overline{n}}(v_d t_d) \tag{3.8}$$

Specifically for the first cluster produced closest to the first GEM (j = 1):

$$P_1(t_d) = \overline{n} \cdot e^{-\overline{n}v_d t_d} \quad \Rightarrow \quad \sigma_1(t_d) = \frac{1}{\overline{n} \cdot v_d} \tag{3.9}$$

The latter gives the *intrinsic* value for the time resolution of the detector if the first cluster is always detected.
A high primary ionization ($\overline{n}$) and a fast (v_d) gas mixture should be chosen in order to improve the time performance of a GEM detector.
A preliminary simulation study of the gas mixture properties [59] has been done by using the following simulation tools:

- *Magboltz*, which computes the electron drift velocity, the longitudinal and the transverse diffusion coefficients;
- *Heed*, which calculates the energy loss through the ionization of a particle crossing the gas and allows to simulate the cluster production process;
- *Imonte*, which computes the Townsend and attachment coefficients;

[9] In general, the number of clusters produced in the drift region is correlated to the type of incident particle (α, γ, π, proton), to its energy and the gas mixture used as converter.

Using the *Magboltz* simulation tool, the electron drift velocity as function of the drift field for various gas mixtures tested had been evaluated (Fig. 3.23). The curve of the Ar/CO_2 (70/30) gas mixtures, commonly used by other authors is also reported.

It should be noted that the $Ar/CO_2/CF_4$ (45/15/40) and the Ar/CF_4/iso-C_4H_{10} (65/28/7)

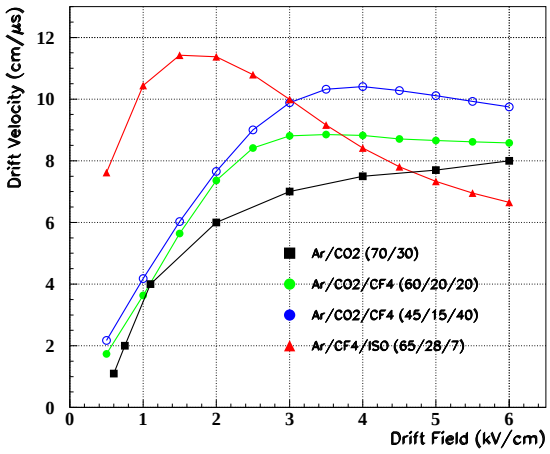

Figure 3.23: Simulated electron drift velocity for the studied gas mixtures. The curve of the Ar/CO_2 (70/30) is reported for comparison.

reach the highest drift velocity, $\sim$11cm/μs, for 3.5 and 2 kV/cm drift field, respectively.
The *intrinsic* time resolution, which depends on the inverse of the product of the drift velocity and the specific primary ionization in the drift gap had been evaluated using *Magboltz* and *Heed* simulation tools.
Tab. 3.1 summarizes the properties of the gas mixtures together with the *intrinsic* time resolution, while in Fig. 3.24 is shown the *intrinsic* time resolution as a function of the drift field.

Gas Mixture	Drift velocity (drift field)	$<$ Clusters/mm $>$	Intrinsic time resolution
Ar/CO_2 (70/30)	7 cm/μs (@3 kV/cm)	3.3	4.7 ns (@3 kV/cm)
$Ar/CO_2/CF_4$ (60/20/20)	9 cm/μs (@3 kV/cm)	5	2.3 ns (@3 kV/cm)
$Ar/CO_2/CF_4$ (45/15/40)	10.5cm/μs (@3.5 kV/cm)	5.5	1.7 ns (@3.5 kV/cm)
Ar/CF_4/iso-C_4H_{10} (65/28/7)	11.5 cm/μs (@2kV/cm)	5.7	1.5 ns (@2 kV/cm)

Table 3.1: Summary table of the gas mixture properties: optimized drift velocity and average cluster yield. The relative *intrinsic* time resolution is also reported.

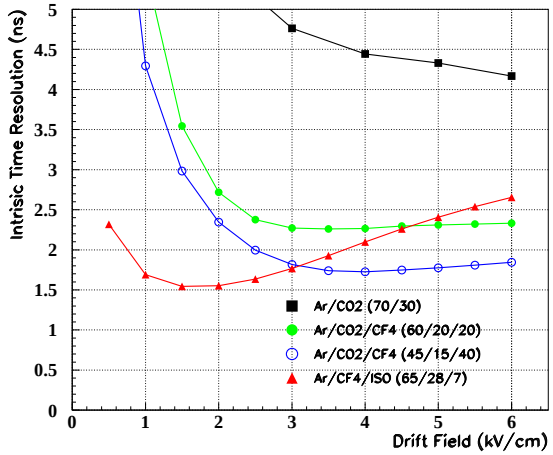

Figure 3.24: The *intrinsic* time resolution of a triple-GEM detector as a function of the drift field. The curve of the Ar/CO_2 (70/30) is also reported as comparison.

The result of this simulation study is that the best *intrinsic* time performance is achieved with the $Ar/CO_2/CF_4$ (45/15/40) and the Ar/CF_4/iso-C_4H_{10} (65/28/7) gas mixtures.

It should be stressed that the *intrinsic* time resolution represents a lower limit. In fact, taking into account the limited *collection efficiency* of the first GEM (Sec. 3.3.3), the statistical fluctuation of the gas gain (under-fluctuation of the gas gain [63]) and the finite threshold of the electronics, it could happen that the signal induced by the first cluster cannot be discriminated. In this case the successive pile-up of clusters is needed to have a signal above the electronic threshold. This effect is the main limitation of the detector time resolution.
In order to avoid or to reduce this effect, it is necessary to increase the single electron detection capability. The use of a fast gas mixture, characterized by a high drift velocity at a relative low value of drift field, which ensures a large *collection efficiency* in the first multiplication stage, gives a high detection efficiency of the first cluster.

3.6 The signal formation

In GEM detector the signal is completely induced by the electron motion in the induction gap. As the first electron emerges from the last GEM, it starts to induce a current on the pads which stops when it is collected.
The current I_k induced on the electrode *k*, due to a moving charge *q* and velocity v_d, can be calculated using the Ramo's theorem [62]:

$$I_k = -\frac{q\overrightarrow{v_d}(x) \times \overrightarrow{E}_k(x)}{V_k} \tag{3.10}$$

where $\overrightarrow{E}_K(x)$ is the electric field created by raising the electrode *k* to the potential V_k.
As such, if V_k= 1 V and all the other pads are connected to ground, Ramo's theorem becomes:

$$I_k = -q\overrightarrow{v}(x) \times \overrightarrow{E}_k^w(x) \tag{3.11}$$

where $\overrightarrow{E}_k^w(x)$ is called the *weighting field*.
The $\overrightarrow{E}_k^w(x)$ behavior has been simulated [59] and it results to be practically constant in the induction gap meaning the electron drift velocity is constant too.
It is expected that each electron emerging from the last GEM induces a rectangular current signal in the nearest pad with a width dependent on the time spent by the electron to cross the induction gap:

$$i = -\frac{q}{t} = -\frac{qv_d}{x} \tag{3.12}$$

where *x* is the thickness of the induction gap and v_d is the electron velocity in that gap.

It must be noticed that for a given charge, higher induced signals have been achieved by reducing the thickness of the induction gap and using a fast gas mixture for induction field in the range 4.5÷5.5 kV/cm.

3.7 The R&D activity on triple-GEM detector

In this section the measurements performed in the R&D activity on GEM detectors operated with CF_4 and isobutane based gas mixture are presented.
The use of such new gas mixtures have also required for the study of the detector capability to tolerate 10 years of LHCb running without damages or performance losses.
For this R&D activity small size prototype have been used, where the geometrical configuration can be easily changed and adapted to the specific test to be performed. These prototype have been realized with three GEM foils (10×10 cm^2 active area) previously stretched with a home-made tool in order to avoid electrostatic instability (see Sec. 4.3.1) and glued on FR4 frames. The anode readout has segmented in 6×16 mm^2 pads. The cathode has made up of a kapton foil, with copper on one side, glued on a similar frame. All frames have then fixed to the FR4 box with nylon screws. The FR4 box has also act as gas container (Fig. 3.25).
The pads have been connected to a fast preamplifier based on VTX-chip with a sensitivity of 10 mV/fC, peaking time of 5 ns and electronic noise charge of about 1300e$^-$ r.m.s at zero input capacitance. The VTX chip, supplying an analog output, resulted to be particularly suitable in this R&D phase.
More details of the prototype chamber construction and the VTX readout can be found in [57].

In the Sec. 3.7.1 and Sec. 3.7.2 the effective gain and the rate capability measurement are respectively discussed.
The results obtained with the fast CF_4 and isobutane based gas mixtures will be discussed in Sec. 3.7.3 and 3.7.3 respectively in term of time resolution and efficiency (in 20 ns time window), while the effects of such gas mixtures on the discharge and ageing effects will be shown in Sec. 3.7.4 and Sec. 3.7.5 respectively.

3.7.1 Effective gain measurement

As already discussed in Sec. 3.4.3, the effective gain of a triple-GEM detector is related to V_{GEM}^{tot} and the first Townsend coefficient [55] as follows:

$$G_{eff} \propto e^{<\alpha>V_{GEM}^{tot}} \tag{3.13}$$

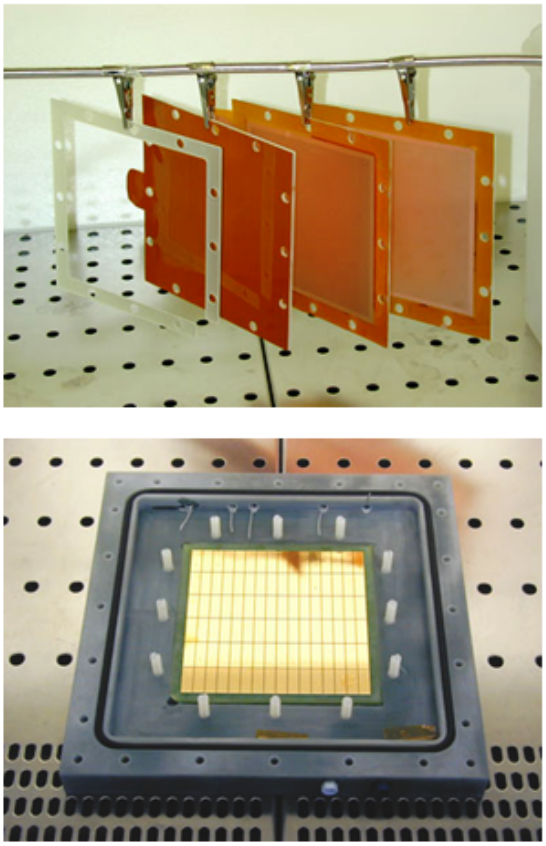

(a) Top: The three GEMs glued on the FR4 frames of different thickness; Bottom: the readout pads mounted on the FR4 box.

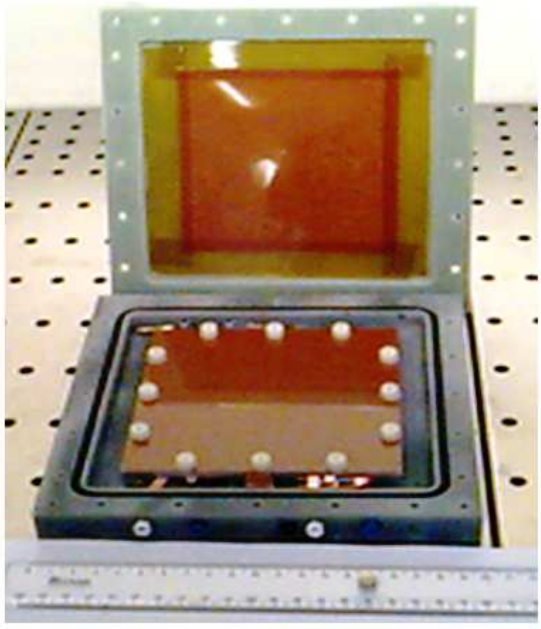

(b) The three GEMs stacked in the FR4 box.

Figure 3.25: The 10×10 cm^2 triple-GEM prototype.

The gas gain measurement has been performed by irradiating a triple-GEM prototype with a high intensity 6 keV X-ray tube.
The current induced on the pad I_{PAD}, for a given X-ray flux Φ_{RX} and irradiating area S, is proportional to the detector gain G, through the relation:

$$I_{PAD} = e \cdot N_\gamma \cdot S \cdot \Phi_{RX} \cdot G \tag{3.14}$$

where *e* is the electron charge and N_γ is the gas ionization produced by the X-ray, that depends weakly on the gas mixture ($\approx$ 200 electron-ion pair).

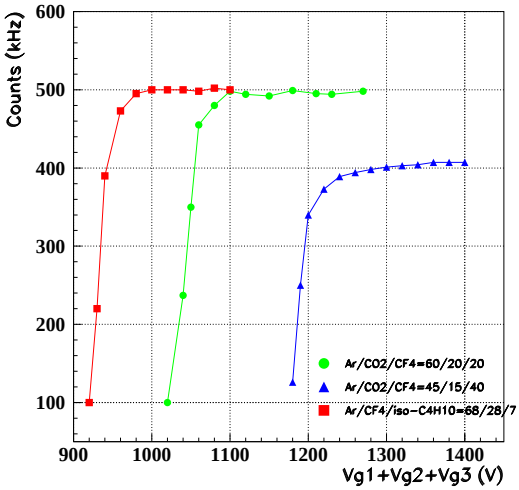

(a) Effective particle rate as a function of V_{GEM}^{tot} for various gas mixtures. The different height of the plateau is due to the different cross sections of the photon conversion in the gas mixture.

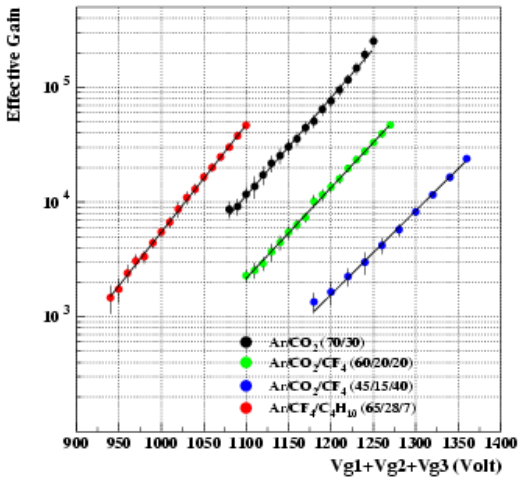

(b) Effective gain of a triple-GEM detector as a function of V_{GEM}^{tot} for the various gas mixtures tested.

Figure 3.26: Effective gain measurements.

Taking into account the different cross sections of the photon conversion in the various gas mixtures, the rate of converted photon, $S \cdot \Phi_{RX}$, has been preliminary measured connecting the pads to the readout electronics. Fig. 26(a) shows the measured particle rate on the pads as function of V_{GEM}^{tot} for the gas mixtures tested. The counts have been recorded with a scaler at the discriminator output, with a discriminator threshold set to 70 mV well above the electronic noise.

Successively, the readout electronics has been removed and the induced current on the readout pads has been measured. Fig. 26(b) shows the effective gain of the detector as a function of V_{GEM}^{tot} for the various gas mixtures tested and for the Ar/CO_2 (70/30) gas mixture, commonly used by other authors.
From the exponential fit, the average Townsend coefficient for the different gas mixtures tested has been determined (Tab. 3.2).

Gas mixture	$< \alpha >$ (V^{-1})
Ar/$C0_2$ (70/30)	19.6×10^{-3}
Ar/$C0_2$/CF_4 (60/20/20)	18.2×10^{-3}
Ar/$C0_2$/CF_4 (45/15/40)	16.9×10^{-3}
Ar/CF_4/iso-C_4H_{10} (65/28/7)	21.5×10^{-3}

Table 3.2: Results of the exponential fit of the Townsend coefficient along the multiplication path for the various gas mixtures tested.

3.7.2 Rate capability

The rate capability of a detector depends on the time required by the ions to move from the avalanche region to the ion collection electrode. In a GEM structure the ions produced inside the hole are mainly collected on the upper electrode of the GEM itself in a time of the order of few μs.

The detector rate capability has been measured with the Ar/CO_2/CF_4 (60/20/20) gas mixture at the gas gain of 2×10^4. In Fig. 3.27 a good gain stability was found up to a particle rate of 60 MHz/cm^2, showing a very high rate capability and well above the LHCb requirement. This measurements was limited by the maximum flux of our X-ray tube.

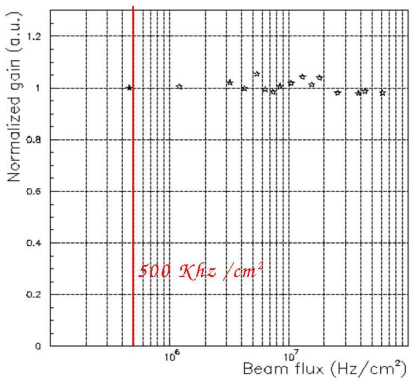

Figure 3.27: Rate capability measurement of a triple-GEM detector: normalized gain as a function of the X-ray flux. The gain stability shows a very good rate capability and is well above the LHCb requirement (500 kHz/cm^2).

3.7.3 Time and efficiency performances

Several tests have been performed at the T11 beam facility of PS-CERN with a π beam of 3÷4 GeV/c. These tests allowed us to measure the time performance and the efficiency in 20 ns time window of the detector operated with the new gas mixtures, for optimized geometry and electric field configurations.

The time performance

As discussed in Sec. 3.5, the time performance of a GEM-based detector are correlated with the gas mixture properties. In particular, it has been shown that good time resolution can be achieved using fast and high primary ionization gas mixtures.
A comparison of the time distribution for the considered gas mixtures is shown in Fig. 3.28 [64]. The electric configuration of the various electric fields which optimize the *collection efficiency* and time performance for the different gas mixtures are summarized in Tab. 3.3.

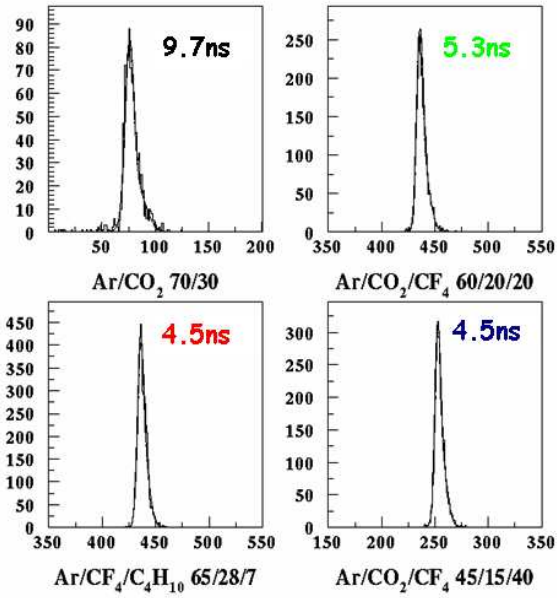

Figure 3.28: The best time distribution for single detector obtained at PS beam facility of CERN [64]. The relative gas gain was: 1×10^5 for the Ar/CO_2 (70/30); 3×10^4 for the $Ar/CO_2/CF_4$ (60/20/20); 1×10^4 for the $Ar/CO_2/CF_4$ (45/15/40); 2×10^4 for the Ar/CF_4/iso-C_4H_{10} (65/28/7).

As expected from the simulation, a considerable improvement with respect to the Ar/CO_2

Gas mixture	E_D (kV/cm)	E_{T1} (kV/cm)	E_{T2} (kV/cm)	E_I (kV/cm)
Ar/CO_2 (70/30)	3.0	3.0	3.0	5.0
$Ar/CO_2/CF_4$ (60/20/20)	3.0	3.5	3.5	5.0
$Ar/CO_2/CF_4$ (45/15/40)	3.5	3.5	3.5	5.0
Ar/CF_4/iso-C_4H_{10} (65/28/7)	2.0	3.0	3.0	5.0

Table 3.3: The electric field configuration used during the tests of the new gas mixtures.

(70/30) gas mixture ($\sim$ 10 ns of r.m.s) is obtained with the iso-C_4H_{10} and CF_4 based gas mixtures, reaching time resolutions better than 5 ns (r.m.s.).

The time resolution (r.m.s.) of a single chamber as function of the gas gain is shown in Fig. 3.29. As expected, an obvious improvement of the time performance is observed increasing the detector gain.
Fig. 3.30 shows the time resolution measurement for two detectors logically OR-ed, as foreseen in the LHCb experiment.

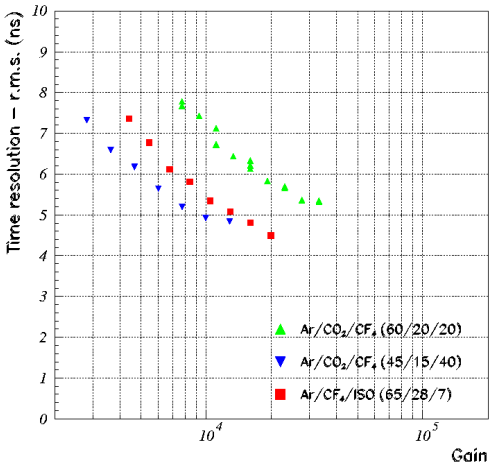

Figure 3.29: Time resolution (r.m.s) as a function of the gas gain for a single detector.

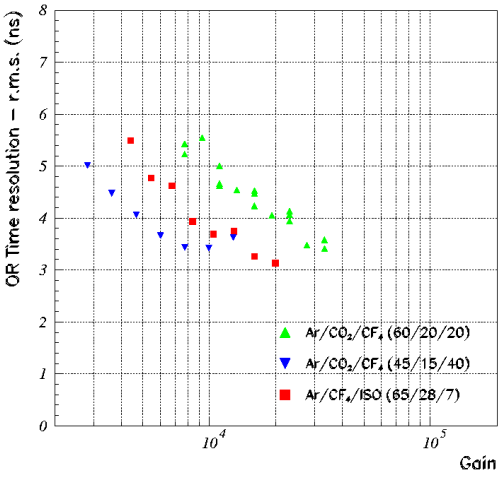

Figure 3.30: Time resolution (r.m.s) as a function of the gas gain for two detectors logically OR-ed.

The efficiency in 20 ns time window

In order to trigger muons produced in consecutive bunch-crossing, a triple-GEM station, i.e two detectors logically OR-ed, should have an efficiency in 20 ns time window higher than 96%.

Fig. 3.31 shows the efficiency in a 20 ns time window as a function of the effective gain for a single detector. As expected the slow and the low primary ionization Ar/CO_2 (70/30) gas mixture does not fulfill the above requirement, even at very high gas gain ($\epsilon_{20} < 85\%$). Viceversa, the use of iso-C_4H_{10} and CF_4 based gas mixtures, allows to reach efficiency in 20 ns time window larger than 96% at moderate gas gain.
The configuration of the electric fields for the various gas mixtures is the same as that reported in Tab. 3.3.
Fig. 3.32 shows the efficiency within 20 ns time window for two detectors logically OR-ed as foreseen by the experiment. Besides a better time performance, the use of two detectors for station provides also some redundancy.

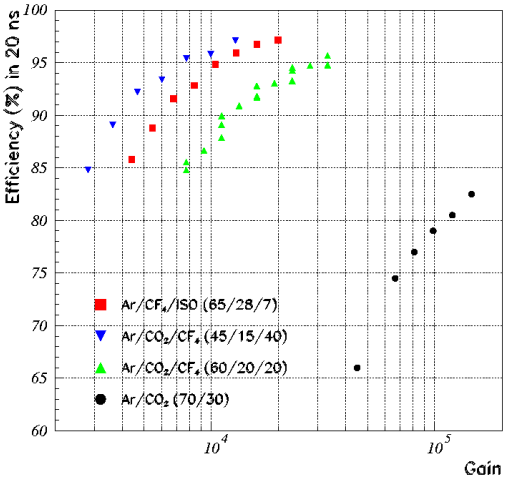

Figure 3.31: Efficiency in 20 ns time window as a function of the gas gain for a single detector. The Ar/CO_2 (70/30) gas mixture is also reported as a comparison .

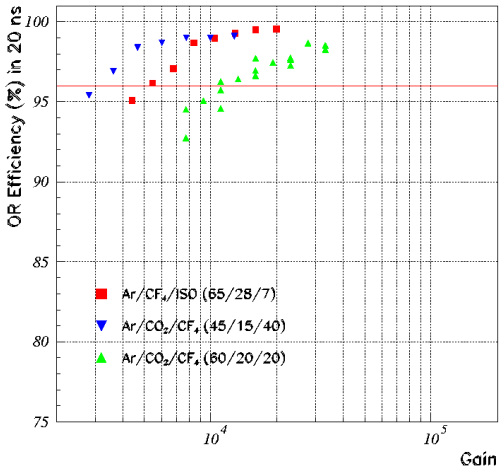

Figure 3.32: Efficiency in 20 ns time window as a function of the gas gain for two detectors logically OR-ed.

3.7.4 The discharge process

The occurrence of discharges in a gas detector is correlated to the transition from avalanche to streamer [65]. This transition is gain and primary ionization density dependent. Indeed, for a given ionizing radiation, the increase of the applied voltage above a certain threshold value, results in a propagating streamer. The threshold value for the transition from avalanche to streamer depends on the type of the ionizing radiation, being lower for highly ionizing particles. The voltage threshold is correlated to the reaching of the Reather limit, that is when the avalanche size exceeds $10^7 \div 10^8$ ion-electron pairs [66],[67].

In GEM detectors, and more generally in micro-pattern detectors, due to the very small distance between anode and cathode, the formation of the streamer can be easily followed by a discharge. The discharge acts as a short circuit between the two copper sides of the GEM foil discharging in a short time the whole charge stored in the GEM. This phenomenon represents one of the most important problems of damage in micro-pattern detectors.
In a triple-GEM detector the discharge probability is in general lower than for other micro-pattern detectors. This is due to the fact at a fixed gas gain a triple-GEM detector has the advantage to share the total gain on the three GEM foils.
In particular, for triple-GEM detectors the discharge probability is larger in the third GEM where the charge density is higher. As discussed in Sec. 3.4.2, a 2 mm 2^{nd} transfer gap helps to reduce the discharge probability.

Discharge studies have been performed at the πM1 beam facility at Paul Sherrer Institute (P.S.I.) of Zurigo. The detector prototypes were irradiated with a low energy hadron flux with an intensity of up to 300 MHz on about ~ 15 cm^2 of the detector active area. The beam is a quasi continuous beam with 19 ns time separation between two particle bunches. In our experimental area, the beam was composed of 300 MeV/c pions with an estimated contamination of 7% of protons.

The discharge probability is defined as the ratio between the observed frequency of discharges and the incident particle rate. The measurement was performed by monitoring and acquiring the currents drawn by the various GEM electrodes. We counted discharges by detecting the current spikes on the pads, corresponding to the OR of the discharges on the three

GEM foils.
In Fig. 3.33 the discharge probability per incident particle is reported as a function of the gas gain for the three gas mixtures. The presence of the isobutane allows to sensibly reduce the discharge probability even at very high gain. This result is due to the high isobutane cross section of photon absorption in the range of 1 and 10 eV that limits the streamer propagation.

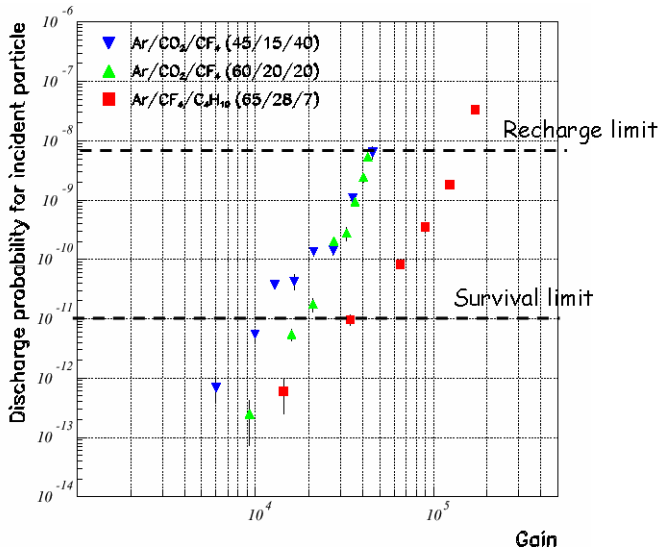

Figure 3.33: Discharge probability per incident particle as a function of the effective gain for a detector with 3/1/2/1 gap geometry.

During the PSI test each detector integrated, without any damages or ageing effect, about 5000 discharges on 15 cm^2, i.e $\sim$ 330 discharges/cm^2.
Taking into account the average charged particle rate expected in LHCb (Φ_{LHCb}=184 kHz/cm^2), the maximum discharge probability ($P_{LHCb}^{discharge}$) to integrate 330 discharges/cm^2 in 10 years (Δt_{LHCb} = 10^8 s) of LHCb running could be calculated as follows:

$$\begin{aligned} P_{LHCb}^{discharge} &= \frac{integrated\ \ discharges\ \ per\ \ cm^2}{\Phi_{LHCb} \cdot \Delta t_{LHCb}} \\ &\simeq 10^{-11} \end{aligned}$$

The estimated maximum discharge probability, which represents a survival limit for discharges, corresponds to a gas gain of about 1.2×10^4, 2×10^4, 4×10^4 respectively for the

$Ar/CO_2/CF_4$ (45/14/40), $Ar/CO_2/CF_4$ (60/20/20) and Ar/CF_4/iso (65/28/7) gas mixtures.

At the same time, it is necessary to take into account the dead time produced by discharges. Since the capacitance of a GEM sector is $\sim$ 10 nF and the limiting resistor is 1 MΩ, the recharging time of a GEM sector (S_{sector}= 80 cm^2 see Cap. 4) in which the chamber results inefficient is $\sim$ 10 ms .
To keep this inefficiency below 0.1%, the maximum tolerable discharge probability comes out to be:

$$\begin{aligned} P_{LHCb}^{discharge} &< \frac{0.1\%\ inefficiency}{\Phi_{LHCb} \cdot S_{sector} \cdot t_{recharge}} \\ &< 6.8 \times 10^{-9} \end{aligned}$$

Therefore, such a limit due to the recharging is less stringent than the above survival limit.
It should be stressed that the survival limit measured at PSI was conservative because all detectors were still working after the test.
For this reason, we performed a further destructive test to determine the maximum number of discharges that the detector can stand before breakdown. This test was performed in laboratory with an ^{238}Am source. The irradiated area was 0.5 cm^2 and the detector was operated with the $Ar/CO_2/CF_4$ (45/14/40) at a gas gain of 4×10^4, higher than that one foreseen in the experiment (6×10^3). The test was repeated three times and the detectors died after 500, 700 and 800 discharges. Taking the first of the three numbers, assuming the average charged particle rate expected in LHCb and 10 years of running, a maximum discharge probability of 5.4×10^{-11} per incident particle was calculated; from this number and from the results of Fig. 3.33, a maximum gas gain of about 1.8×10^4 for the $Ar/CO_2/CF_4$ (45/14/40) is obtained. Since the detector damage due to a discharge across a GEM hole is correlated with the energy stored in the GEM, that scales as the power of two of the applied voltage ($\mathcal{E}$= 1/2 CV^2), and since the detector was irradiated with highly ionizing particles, also this result must be considered quite conservative.

3.7.5 The ageing process

Gaseous detector have been used for many decades in modern high energy physics experiments for particle detection and tracking. Soon after their development, it has been common to find problems associated with their long exposure to radiation, limiting their lifetime.
The observed phenomenology included the appearance of local and permanent damages detected as self-sustained discharges, excessive currents, gradual loss of performances (energy resolution, decrease and non-uniformity of the gas gain).
These ageing phenomena are correlated with the formation of polymeric layers on the detector electrodes, possibly induced by pollution released by materials used in the gas system or chamber construction, or impurities in the gas itself [68].
The chemistry of the ageing process has not been yet deeply studied thus a rigorous explanation of why certain chambers age and others do not cannot be yet discussed with certainty. The approach to the ageing problem is still in most cases purely experimental.
It should be stressed that ageing test should be performed as close as possible to the real conditions. Consequently, the irradiated area of the detector should be as large as possible while the detector should be operated with a gas flow and radiation flux which are comparable to those foreseen in the experiment. Of course for time constrains such tests must be accelerated, then a radiation flux several times higher than the foreseen one have to be used, often affecting the reliability of the results.

Considering the average charged particle rate expected at LHCb on the whole detector area and a gas gain of $\sim 10^4$, a current of about 8 μA is expected on the readout pads.
In this section preliminary aging tests, performed irradiating a small area of the detector, are discussed. This measurement allows to test the long-term radiation compatibility of the different gas mixtures with the GEM foil materials. On the contrary in in Sec. 4.4.1 a large area ageing test in very different experimental condition will be discussed.

Tests have been performed by irradiating a triple-GEM prototype with a high intensity X-ray tube. The X-ray flux was $\sim$ 50 MHz/cm^2 and the irradiated area was about 1 mm^2. The gain changes induced by the ambient parameters variations (temperature and atmospheric pressure) have been corrected by a second, low irradiated, triple-GEM detector used as a reference chamber. The reference chamber has installed in the same gas line upstream the

high irradiated chamber. During the tests no humidity monitoring has performed and the gas has supplied with an open flow system, using Rilsan tubes for a global tube length of 15 m (including exhaust line). We can not exclude that these measurements have done with a not negligible water content (hundreds of ppm) in the gas mixture. No oil bubblers have used on the exhaust gas line. As foreseen in the experiment, the gas flow was 100 cc/min enough to avoid the gas poisoning due to the ionizing radiation flux used in the measurement.
The behavior of the normalized gain as a function of the integrated charge is shown in Fig. 3.34, Fig. 3.35 and Fig. 3.36 for the various gas mixtures tested. The charge integrated in 10 years of LHCb running (Δt_{LHCb}) has been estimated as follows:

$$Q_{LHCb}^{integrated} = 2 \cdot \Phi_{LHCb} \cdot \Delta t_{LHCb} \cdot e \cdot N \cdot G \tag{3.15}$$

where the factor 2 takes into account that the integrate charge is by means the sum of the currents induced on the pads readout and the bottom electrode of the third GEM (G3 D), Φ_{LHCb} is the average charged particle flux expected flux in M1R1 (460 kHz/cm^2)[10], *e* is the electric charge (1.6×10^{-19} C), *N* is the specific ionization that is estimated to be $\sim$ 40 electron-ion pair for all the gas mixtures and *G* is the gas gain used in the test.
Tab. 3.4 summarizes the values of the gas gain, the integrated charge and the equivalent LHCb years of running for each of the gas mixtures tested.

Gas mixtures	Gas gain	Integrated charge (C/cm^2)	Equivalent LHCb years
Ar/CO_2/CF_4 (60/20/20)	2×10^4	20	$\sim$ 16 years
Ar/CO_2/CF_4 (45/15/40)	6×10^3	4.2	$\sim$ 11 years
Ar/CF_4/iso-C_4H_{10} (65/28/7)	1×10^4	10.2	$\sim$ 15 years

Table 3.4: Summary table of the local ageing test.

As shown in Fig. 3.34 and Fig. 3.35 no ageing effects, generally due to the presence of the CF_4, have been observed [11], while a moderate ageing (less than 10% in 10 LHCb equivalent years) has been observed with the Ar/CF_4/iso-C_4H_{10} gas mixture.
The positive result obtained with the isobutane based gas mixture is probably due the presence of the CF_4 whose dissociation products, that can lead to the formation of hydrofluoric

[10] This quote particle rate value has been used in all publications of our group instead of 184 kHz/cm^2 because during the R&D activity the average particle flux was not still defined. Since this value was updated at 184 kHz/cm^2, the integrated charge in these tests results conservative.

[11] On the contrary, as will be discussed in Sec. 4.4.1, not negligible etching effects have been observed in different experimental condition during the large irradiation test with full size detectors.

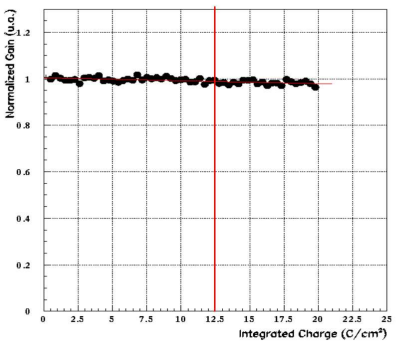

Figure 3.34: Normalized gain as a function of the integrated charge (PAD+ G3 D) for the $Ar/CO_2/CF_4$ (60/20/20) gas mixture [64]. The detector gas gain has been set at 2×10^4. The red line indicates the integrated charge corresponding to 10 years of operation at LHCb.

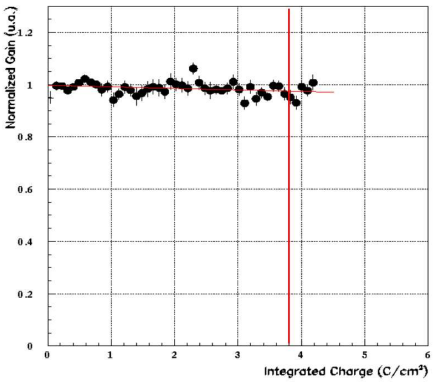

Figure 3.35: Normalized gain as a function of the integrated charge (PAD+ G3 D) for the $Ar/CO_2/CF_4$ (45/15/40) gas mixture [64]. The detector gas gain has been set at 6×10^3. The red line indicates the integrated charge corresponding to 10 years of operation at LHCb.

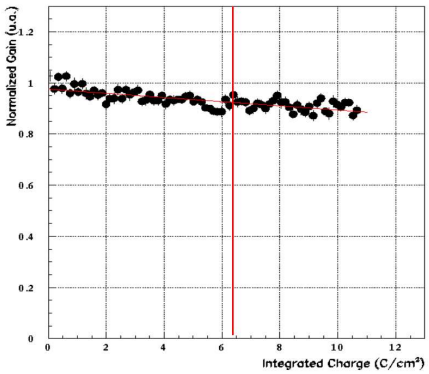

Figure 3.36: Normalized gain as a function of the integrated charge (PAD+ G3 D) for the $Ar/CF_4/iso\text{-}C_4H_{10}$ (65/28/7) gas mixture [64]. The detector gas gain has been set at 1×10^4. The red line indicates the integrated charge corresponding to 10 years of operation at LHCb.

acid (HF) in presence of a not negligible water contamination, can be very effective in suppressing polimerization processes (CF_4 etching effect [69]).

3.8 Conclusions of the R&D activity

The R&D activity performed on the triple-GEM detector (10×10 cm^2 of active area) give us very interesting and unique results.
The detector shows very high rate capability, well above the maximum rate at LHCb.
The detector geometry, the electric fields configuration and the gas mixtures have been studied in order to optimize the detector efficiency in 20 ns time window and the time performance, and to minimize the discharge probability.
Time resolutions better than 5 ns are achieved with fast and high yield CF_4 and iso-C_4H_{10} based gas mixtures, considerably improving the results obtained in the past with the standard Ar/CO_2 (70/30) gas mixture ($\sim$ 10 ns).
With these new gas mixtures, the detector achieves an efficiency in 20 ns time window above the 96% at moderate gas gain, while keeping the discharge probability per incident particle lower than $\sim 5\times10^{-11}$.
In particular, the results with the high intensity pion/proton beams at PSI have shown that the use of a small fraction of iso-C_4H_{10} or a large amount of CF_4 results in very stable detector operation. Moreover, this test demonstrates that a triple-GEM is a very robust detector.
After a high intensity local X-ray irradiation equivalent to more than 10 years of operation at LHCb-M1R1, negligible ageing effects have been observed with the CF_4 based gas mixtures.

Taking into account these considerations and considering the necessity to avoid the use of flammable gas, we choose the Ar/CO_2/CF_4 (45/15/40) as the reference gas mixture for the LHCb experiment.
For this gas mixtures, the best choice for the electric fields of the detector is 3.5/3.5/3.5/5 together with the unbalanced configuration of the voltages applied to GEMs ($V_{GEM1} \gg V_{GEM2} \geq V_{GEM3}$).

Chapter 4

The triple-GEM detector in LHCb

4.1 Detector overview and requirements

The total area of M1R1 region, about 0.6 m^2, will be covered with 12 stations composed by two triple-GEM detectors logically OR-ed pad by pad. The active area of each station is 200×240 mm^2.

The stations are arranged in four layers to provide full angular coverage: two layers are upstream and downstream the wall support structure (Fig. 4.1). The stations must fit into the 37 cm space available between the RICH2 and the Preshower (Fig. 4.2).

However, the major constraint for the station dimension is the space available around the beam pipe. Fig. 4.3 shows the transverse view ($y - x$ plane) with respect to the LHCb beam axis, together with the chamber active area, the panels and the electronics dimension. In this space is also included the gas pipes, the high voltage (HV) and the low voltage (LV) cables to supply the station and the electronics respectively.

Tab. 4.1 summarizes the space constraints of the M1R1 stations.

Station	Constraint
active area	200×240 mm^2
thickness	< 75 mm
x-length	< 430 mm
y-length	< 310 mm

Table 4.1: Space constraints for a detector station in M1R1.

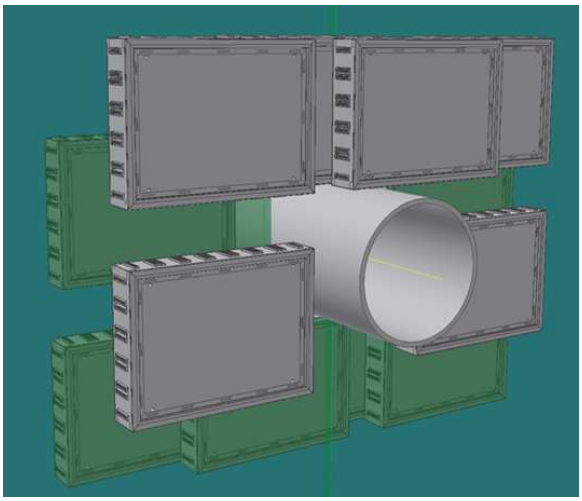

Figure 4.1: Sketch of the station arrangement in M1R1 region in the x-y plane. The two sets of detector stations, upstream and downstream the wall support structure, are shown with different colors.

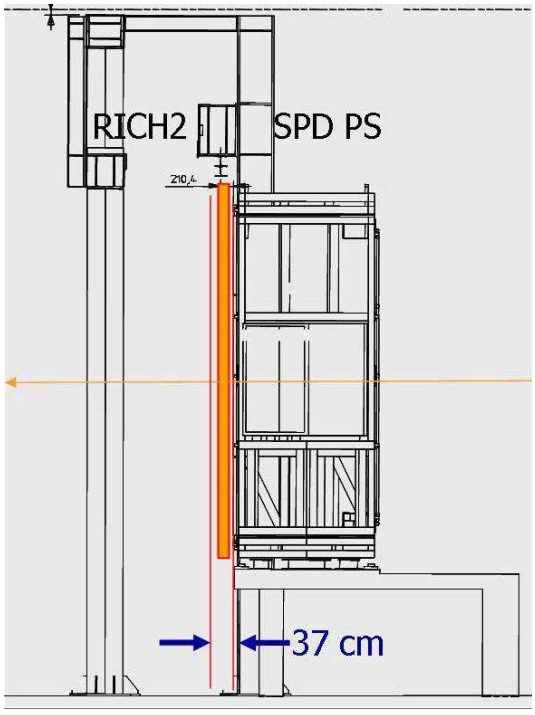

Figure 4.2: Sketch of the station arrangement in M1R1 region in the z plane.

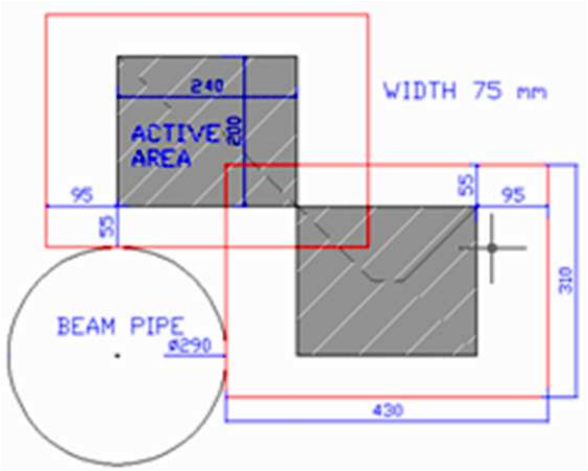

Figure 4.3: Transverse view, with respect to the LHC beam axis, of the geometrical envelope of 2 out of the 12 stations, together with the chamber active area, the panels and the electronics dimension.

The detector requirements that a triple-GEM station have to fulfill in M1R1 region are:

- a particle rate capability up to 500 kHz/cm^2;
- each station must have an efficiency higher that 96% within 20 ns time window;
- a pad cluster size, i.e. the number of adjacent detector pads fired when a track crosses the detector, should not be larger than 1.2 for a 10×25 mm^2 pad size;
- the detector must tolerate, without damages or performance losses, an integrated charge of ~ 1.8 C/cm^2 in 10 years of operation at a gas gain of $\sim 6\times10^3$ and an average particle flux of 184 kHz/cm^2 for an average luminosity machine of 2×10^{32} cm^{-2} s^{-1};

Moreover, since the M1 is placed in front of the calorimeters, a special care has to be taken in the detector design to minimize the material budget. All components used for the chamber construction have been selected in order to minimize this requirement. Clearly, these choices are a compromise between rigidity and low mass requirements. The materials must be also qualified for long term exposure to radiation. As shown in Tab. 4.2, the material budget of the detector station, electronics and faraday cage is about 9% of X_0.

In order to provide the full angular coverage, an overlap of two or more stations is present as shown Fig. 4.4, where the material budget distribution, in percentage of X_0, is reported for the overlap of three stations in one corner of the M1R1 region. The material budget is $\sim$ 6% X_0 in the active area, while it increases up to 20% in correspondence of the overlap of the FR4 frames.

Part	**Details**	**Radiation length** [cm]	**% of** X_0
3 GEMs foil	6×5 μm Cu	1.43	0.21
	3×50 μm kapton	28.6	0.05
			TOTAL: 0.26
Cathode plane	24 μm Cu	1.43	0.16
	2 mm FR4	19.3	1.03
	18 μm Cu	1.43	0.13
	1 μm Ni	1.42	0.007
	0.15 μm Au	0.33	0.005
	8 mm Honeycombs		0.15
			TOTAL: 1.48
Readout plane	24 μm Cu	1.43	0.16
	2 mm FR4	19.3	1.03
	18 μm Cu	1.43	0.13
	1 μm Ni	1.42	0.007
	0.15 μm Au	0.33	0.005
	8 mm Honeycombs		0.15
			TOTAL: 1.48
Frame (uniformly spread)	7 mm FR4	19.4	0.7
			TOTAL / chamber : 3.92
Electronics (uniformly spread)	1 mm $Si0_2$	12.3	< 0.5
Faraday Cage (uniformly spread)	300 μm Brass	1.43	< 0.5
			TOTAL / station : 8.84

Table 4.2: Material budget for a triple-GEM station.

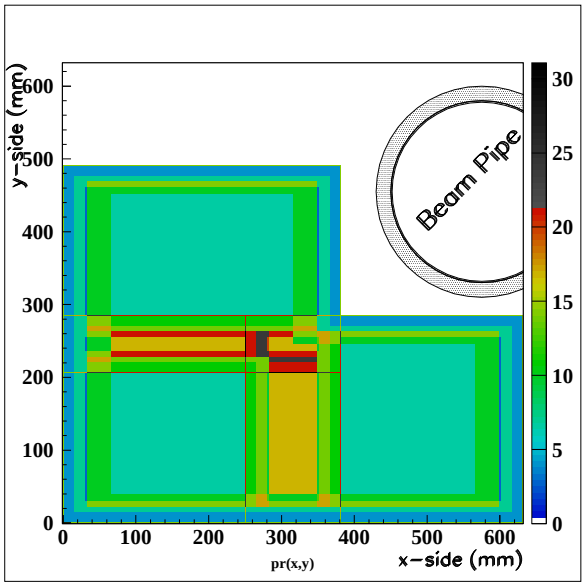

Figure 4.4: Material budget distribution in percentage of X_0 in the overlap of three stations.

4.2 Chamber components and design

4.2.1 The honeycombs panels

The main support of a chamber is given by two honeycomb panels acting as drift cathode and pad-readout. The panels are custom-made using the vacuum bag technique. During the panels production, a machined ALCOA-alloy plane is used as reference.
The panel is made with a 8 mm honeycomb foil which is sandwiched between a gold plated (0.15 μm) PCB faced to the sensitive volume and a back-plane realized with a copper clad (12 μm) fiberglass (FR4). The panels house two FR4 gas inserts, which are connected to the inner detector volume through two holes on the corner of the PCB. Four additional FR4 bushing are used as reference holes for the detector assembly and during the installation of the final detector on the wall support structure of the experiment.
Fig. 4.5 shows the various step of the panels production, while Fig. 4.6 shows a sketch of the final panel assembly in the vacuum bag.

PCB panels are checked for planarity with a 3-D machine measuring on a grid of 35 points. Measurements of the first twelve panels show that a displacement from an average plane is of the order of 60 μm (r.m.s.) (Fig. 4.7).

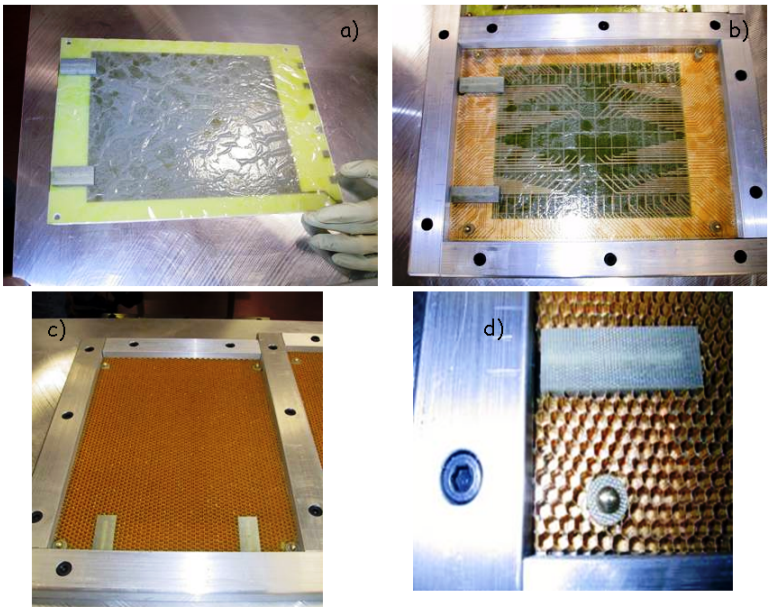

Figure 4.5: Panel production steps: (a) the cathode and (b) the readout PCB are coupled with gas inserts and the four bushing. Then a thin 3M epoxy film is applied; c) the honeycombs foil, cut to size, is placed above followed by the back-plane; d) close view of the gas insert and the bushing.

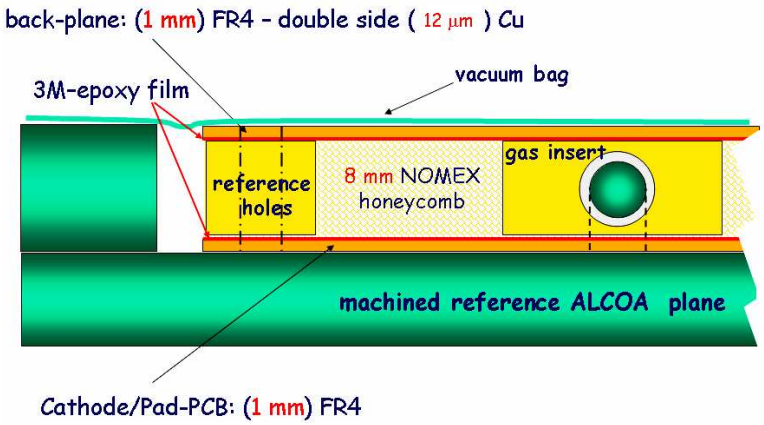

Figure 4.6: Sketch of the panel assembly in the vacuum bag.

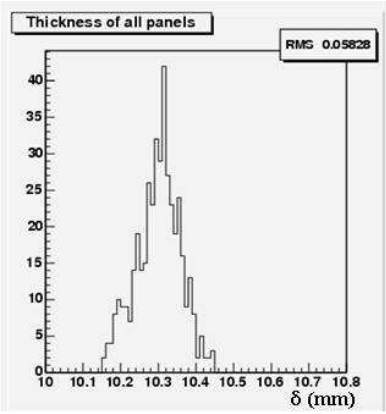

Figure 4.7: Distribution of the displacements, δ, of twelve PCB panels from an average plane.

The drift panel

The drift panel is a simple printed circuit with the drift cathode area of 200×240 mm^2 realized with successive layers of copper (18 μm), nickel (1 μm) and gold (0.15 μm). On one side, seven contact pads for the HV connection of the various detectors electrodes are present (Fig. 4.8).

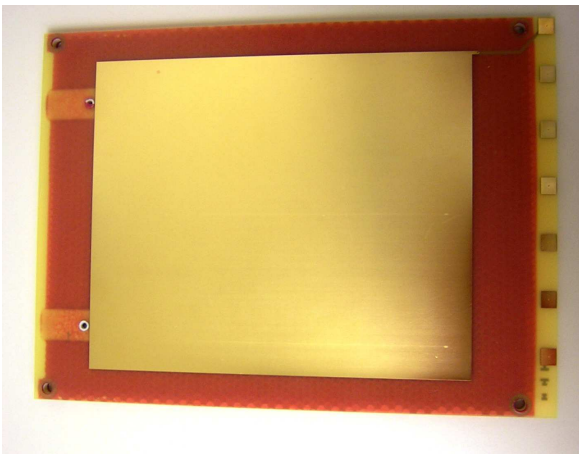

Figure 4.8: The PCB cathode: the gold-plated area represents the active area of the chamber. The two gas inserts and the seven HV contacts are visible in the left and the right of the picture respectively.

The pad-readout panel

The PCB readout is a matrix of 8×24 gold-plated pads (25×10 mm^2) with a ground grid of 100 μm between the pads (Fig. 4.9). As will be discussed in Sec. 4.4.2, we chose such a pad readout in order to minimize the effect of the geometrical cluster size.

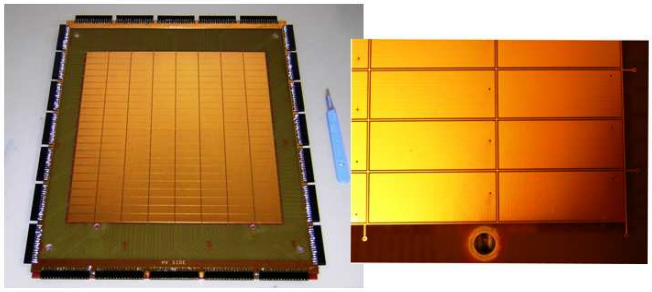

Figure 4.9: The pad readout: the gold-plated pad matrix of 200×240 mm^2 represents the active area of the chamber. A close view of the insert gas and the ground grid between the pads is shown in the right picture.

In addition, the capacitance, Fig. 4.10, of the pad including the trace from the pad to the output connector, which affect the minimum value of the electronics threshold, has been kept below 30 pf with the pad layout shown in Fig. 4.11.
A readout panel is validated for the chamber production if it satisfies the planarity criteria mentioned above and if shorts are not presents.

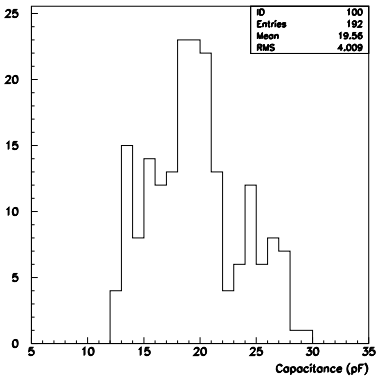

Figure 4.10: Capacitance distribution of our pad layout.

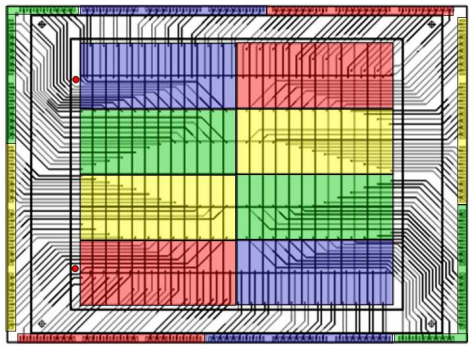

Figure 4.11: Station pad layout as view from the L0 muon trigger.

4.2.2 The GEM foil

The GEM hole has a bi-conical shape with an external and internal diameter of 70 μm and 50 μm respectively, and hole-pitch of 140 μm.
The GEM foils are manufactured by the CERN-EST-DEM workshop following our global geometrical design. The foil has an active area of 202×242 mm^2, which is little greater then those of the panels because a small misalignment in the chamber assembly can occur. The effect of this choice, which will be discussed in Sec. 4.4.2, allows to obtain a full efficiency in the overlap of two adjacent stations.
Moreover, in order to reduce the energy stored on the GEM and the discharge propagation, one side of the foil has been divided in six sectors ($\sim 66\times240$ mm^2) while the other side is not segmented. The separation between sectors is 200 μm.
Fig. 4.12 shows the segmented side of a GEM foil and the HV connections.

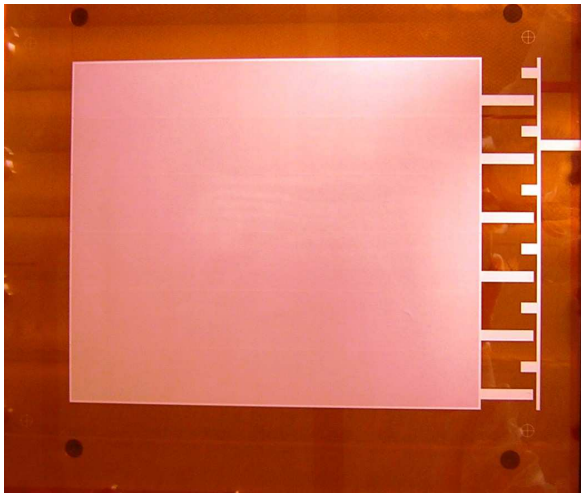

Figure 4.12: A GEM foil as seen from the segmented side. The HV connections are visible on the right of the picture.

In order to check the quality of GEM foils, various quality tests are performed. A preliminary optical inspection is performed with a microscope to check for photolithographic imperfections. If the GEM foil passes the visual inspection, a high voltage test is performed. Such a test is done in a gas tight box (Fig. 4.13), flushed with nitrogen in order to keep the relative humidity at $\sim$25% level. The voltage is applied through a 100 MΩ limiting resistor,

to avoid damages to the GEM foil in case of discharges. The acceptance requirement is a maximum leakage current less than 1 nA at 500 Volts. The HV test is performed twice: before the frame gluing, checking each sectors; after the GEM framing, when the SMD limiting resistor are soldered in the slots of the frame, checking the whole GEM foil, before the final assembly.

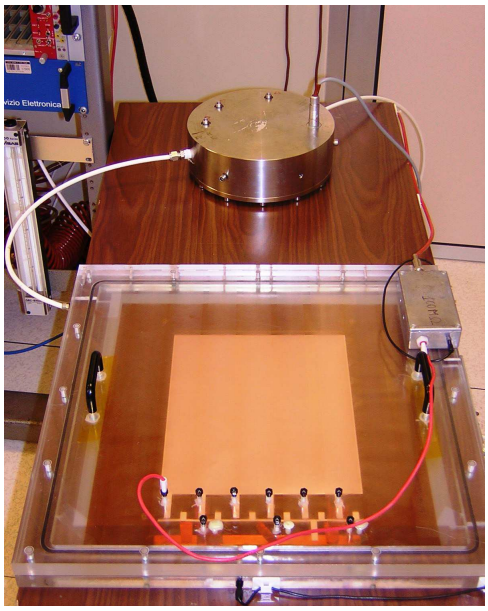

Figure 4.13: The gas tight plexiglass box used for the HV test of GEM foils.

4.2.3 The frames

The GEM electrodes are supported by fiberglass frames (FR4) of suitable size and thickness (1, 2 or 3 mm).
On the HV side six slots are used to allocate the limiting resistors, which permit to apply the high voltage to the six sectors of the segmented side of the foil. Four holes, drilled at the corners of the frame, are used as reference holes for the chamber construction. Fig. 4.14 shows the layout of a frame.
Since the internal side of the fiberglass frame are in contact with the sensitive volume of the detector, they are visual inspected in order to find and eliminate any residual spikes or broken fibers, and then cleaned in a ultrasonic bath with de-ionized water and dried in an oven at a

temperature of 80 ^{o}C for 12 hours (Fig. 4.15).

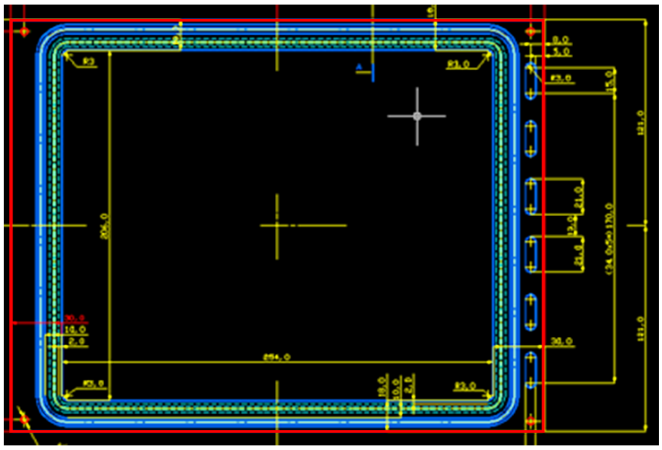

Figure 4.14: The frame layout.

Figure 4.15: The clean procedure of the frame. From the left to the right: the visual inspection; the cleaning in the ultrasonic bath; the drying in the oven at 80 ^{o}C.

4.3 Chamber construction and tools

All the construction operations are performed inside a class 1000 clean room. The schematic of the triple-GEM assembly is shown in Fig. 4.16.

The whole assembly procedure has been defined in each steps as follows:

- The GEM foils, which pass the optical inspection and the HV quality tests, are stretched with a home-made tool. The GEM foil is clamped with jaws equipped with a plastic O-ring. The mechanical tension of 10 N/jaw (two jaws per side), corresponding to a mechanical pressure of 20 MPa, is applied at the edge of the foil and monitored with gauge-meters (Fig. 4.17). The advantages of this stretching technique will be discussed in detail in the next section.

- The frame is glued on the stretched GEM foil using the Araldite 2012 which has a good electrical behavior and suitable handling properties (work life of 5 minutes and curing time of 2 hours). The aging properties of this glue has been studied with a global irradiation test, which will be described in Sec. 4.4.1. In order to prevent epoxy diffusion into the GEM and to assure an uniform glue layer, a rolling wheel is used to apply the epoxy on the frame. Each GEM foil is framed following the above procedure with 1, 2 and 3 mm thick frame.

- The 1 MΩ SMD limiting resistors are soldered in the 6 slots of the frame (Fig.4.18) and a HV test is performed again on the whole GEM foil, before the final assembly.
  .

- The three framed GEMs are glued on the top of the cathode PCB using four reference pins to guarantee the mechanical positioning, following the right order: the 3 mm thick frame, defining the drift gap; the 1 mm thick frame (1^{st} transfer gap); the 2 mm thick frame (2^{nd} transfer gap) and then the last 1 mm thick frame (bare), which followed by the pad panel, defines the induction gap (Fig. 4.19).
  This assembly operation is performed on a machined ALCOA-alloy reference plane. On the top of the whole sandwich a load of 100 kg is uniformly applied for 24h, as required for epoxy polimerization (Araldite AY103 + HD991 hardener). This glue ensures a good electrical behavior, convenient handling properties and well-known aging

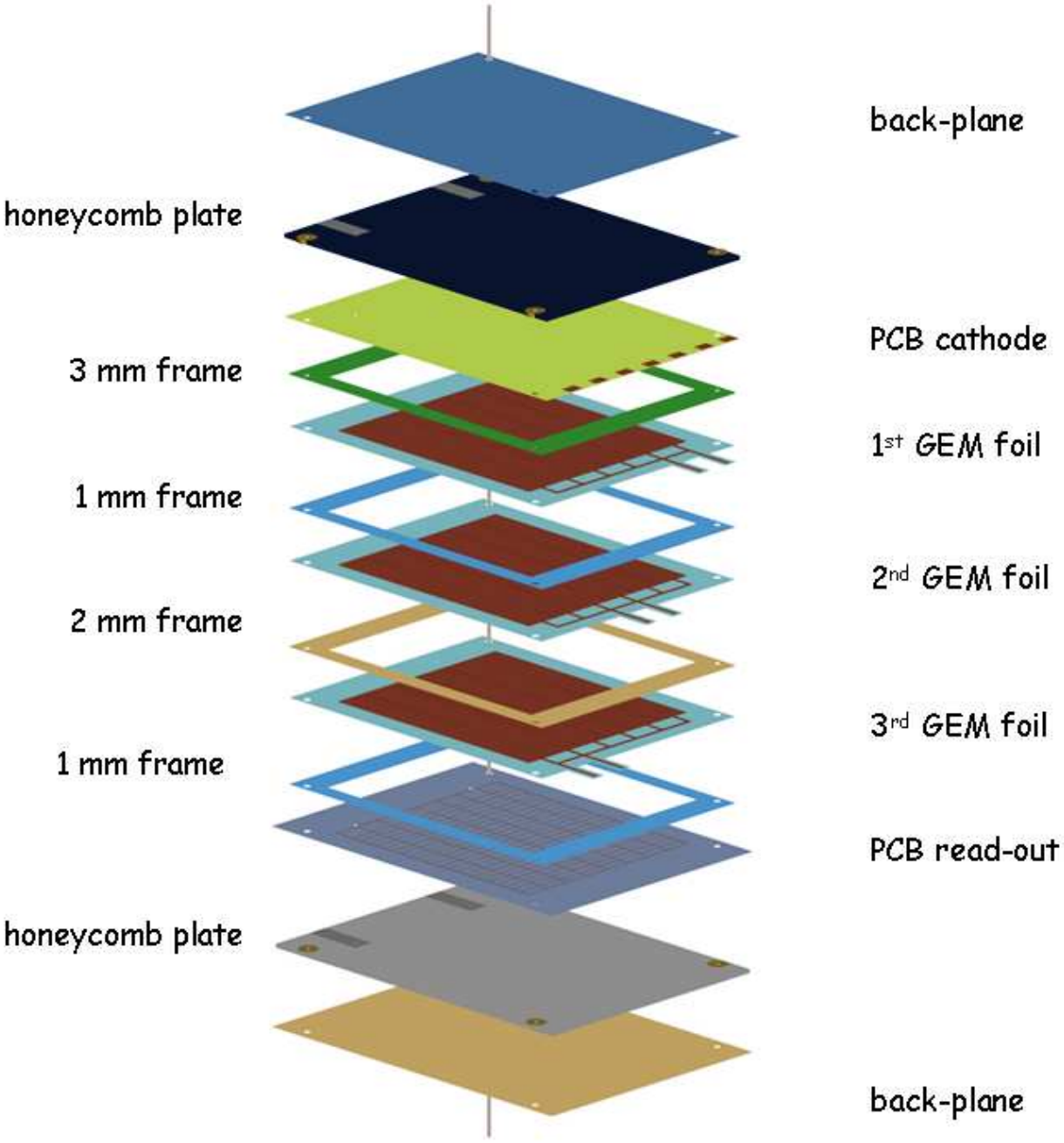

Figure 4.16: Exploded view of a triple-GEM assembly.

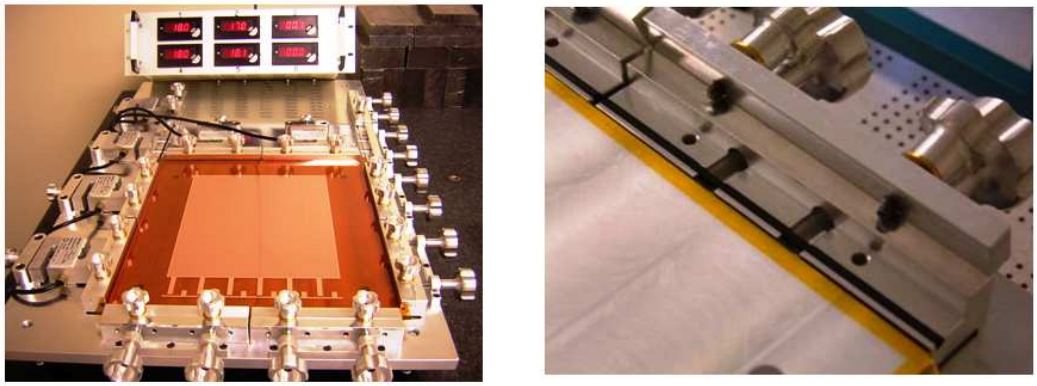

Figure 4.17: Left: The GEM foil under stretching; Right: a close view of the jaw, equipped with a plastic O-ring, used to clamp the foil.

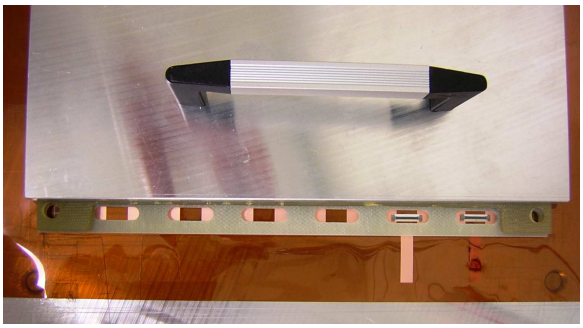

Figure 4.18: Soldering of the SMD limiting resistor inside the six slots of the frame.

properties [70]. To prevent micro-leaks, the edges of the chamber are sealed with a thin layer of glue.

- The chamber is then completed with the final soldering of the HV connections to the contacts of cathode panel. To avoid gas leaks from the corners of the chamber and to hang up the chamber on the muon wall, Stesalite bushings are inserted and glued in the the four reference holes of the structure.

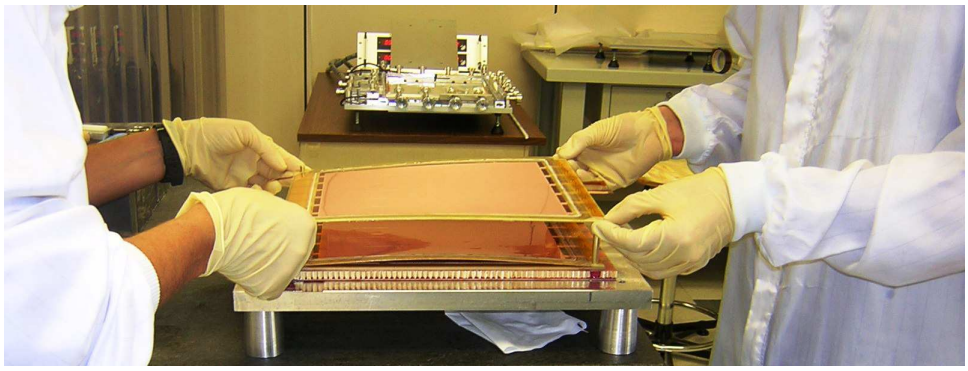

Figure 4.19: The framed GEMs are assembled on the cathode PCB.

4.3.1 The stretching of the GEM foil

The electrostatic attraction between the electrodes of two consecutive GEM foils could produce a sag of the foil itself, including electrostatic instability such as foil oscillation, and giving rise to possible discharges and local gas gain changes.
For example, in COMPASS experiment, which is equipped with triple-GEM detector, the GEM foils are not stretched. To avoid the problem of the sag, a grid of thin fiberglass spacer ($\sim$ 400 μm width) was used as a support for the GEM foil. Of course the support grid, placed inside the active area, causes a not negligible loss of the detector efficiency [70].
To avoid electrostatic instability and to achieve a good uniformity response, we chose to stretch the GEM foil. The mechanical tension applied to the GEM foil and its behavior as a function of time have been investigated with various tests.

Electrostatic attraction effect

When an electric field, E, is applied between two consecutive GEMs, an electrostatic attraction is established and its value is given by [71]:

$$\frac{F}{S} = \frac{\epsilon}{2} \cdot (E)^2 \tag{4.1}$$

where E is expressed in V/m thus the electrostatic pressure F/S is expressed in Pa.
Assuming the permittivity of the gas mixture equal to that of the vacuum and by applying an electric field of 5 kV/cm between two consecutive foils, an equivalent pressure due to electrostatic force of $\sim$1 Pa is obtained.

To estimate the sag produced by 1 Pa on a GEM foil, previously stretched at 20 MPa, a uniformly distributed load of 0.8, 1.6 and 2.4 N is applied. Using the 3-D machine, the foil bending is measured on a grid of 25 points (Fig. 4.20, 4.21).
Since a load of 1 N distributed over an area of 400×400 mm^2, equivalent to $\sim$ 6 Pa, gives a sag of $\sim$ 100 μm and since the sag linearly depends on the mechanical pressure, the electrostatic pressure of $\sim$ 1 Pa will produce a sag of $\sim$ 15 μm.
It should be stressed that such estimation represents an upper limit for the actual sag of a stretched foil because the two opposite forces, symmetrically applied to each GEM foil, result in a vanishing sag.

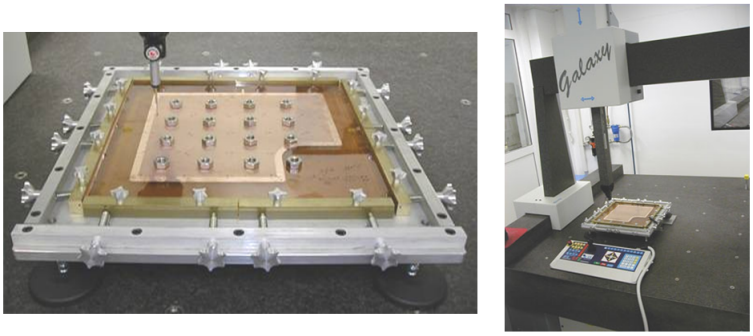

Figure 4.20: Left: Close view of the distributed load on the GEM foil; Right: The 3-D machine used for the measure GEM sag.

Creep effect

In addition, it should be taken into account the kapton *creep*, i.e. the plastic deformation of the kapton when it is stressed above its yield stress [72]. The latter is the stress at which the material behavior changes from the elastic to plastic. In fact, applying repeatedly a mechanical tension to a GEM foil, the kapton strain does not return to its initial state. Fig. 4.22 shows the mechanical tension applied on a kapton foil, normalized at 20 MPa, as a function of the time for two consecutive stretching procedures. After two hours a mechanical tension loss of $\sim$ 10% is observed, while the creep rate decrease to about $\sim$ 1% in the same time interval. Taking into account for this effect, the GEM foil is stretched twice before to proceed for the gluing of the frame.

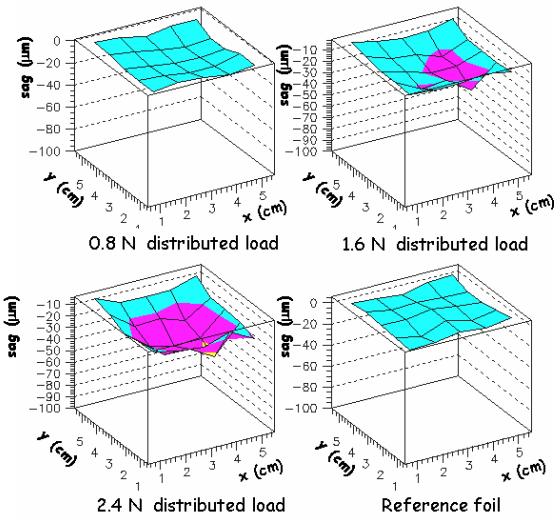

Figure 4.21: Measure of the bending of a GEM foil, previously stretched at 20 MPa, when a distributed load of 0.8, 1.6 and 2.4 N are applied.

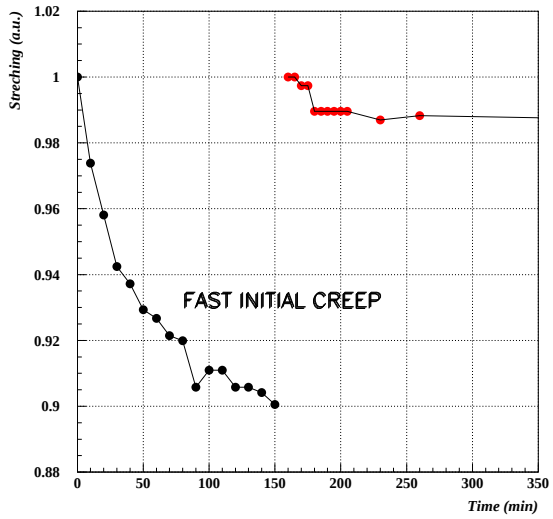

Figure 4.22: The mechanical stretching behavior as a function of the time. Repeated stretching allows to practically recover the kapton *creep* rate.

Radiation effect

The radiation effects on the mechanical stretching of the GEM foil and the epoxy resin, used to glue the GEM on the fiberglass frame, have been studied at the γ irradiation facility of

the ENEA Casaccia. For this test, a 20×24 cm^2 GEM foil has been stretched at 20 MPa and then framed. To characterized the GEM foil before the test, a distributed load of 1 N, corresponding to a mechanical pressure of 20 Pa, has been applied, resulting in a sag of $\sim$ 95 μm.
After 10 days of irradiation at 20 Gy/h (equivalently to 4 years of LHCb), a sag of 120 μm has been measured for a mechanical pressure of 20 Pa. Therefore, a mechanical tension loss of $\sim$ 20% has been observed at the end of the test, which in our case correspond to a negligible effect (from 15 μm to 18 μm, in pessimistic case).

4.3.2 Mechanical specification

The uniformity of the chamber performances, such as the efficiency and the gas gain, depends on the mechanical tolerance on each gap. In fact, since the tolerance on the GEM hole diameter is by construction very tight, $\pm$ 2.5 μm, and the gas gain saturates for the hole range of 40÷70 μm, the effect on the gain due to hole diameter disuniformity is practically negligible.
Taking into account the planarity of the PCB panels, the possible disuniformity of the various gluing, the precision of the frame thickness, we estimate a global mechanical tolerance of $\sim$ 100 μm for each gap of the chamber.

As discussed in Sec. 3.4.3, the effective gain of a GEM detector is the product of the intrinsic gain and the electron transparency, which depends on the electric field inside the GEM holes and the electric field of the various gaps, i.e. E_D, E_{T1},E_{T2}, E_I.
Since the electric field can be assumed constant across the gap, its value is done by the ratio of the voltage difference applied to the electrodes and the thickness of that gap, i.e V/d. Therefore, a local variation of the gap thickness (δgap) will correspond to a variation of the electric field in the gap (δE_{gap}) and consequently to a variation of the effective gain, δG_{eff}, through the changes induced on the electron transparency, T:

$$\delta gap \implies \delta E_{gap} \implies \delta T \implies \delta G_{eff}$$

Since the effective gain represents the charge collected on the the pads readout, the measurements of the effective gain has been performed measuring the current induced on the pads.

The drift field is set to 3.5 kV/cm in order to maximize the drift velocity of the $Ar/CO_2/CF_4$ (45/15/40) gas mixture (Fig. 4.23). A mechanical tolerance of $\pm$ 100 μm on the drift gap, 3 mm thick ($\sim$ 3% of the gap size), is equivalent to a drift field variation of $\pm$ 0.1 kV/cm. The pad current as a function of the drift field is shown in Fig. 4.24. The red dotted line indicates the value chosen for the drift field, while the black lines indicate the range of variation ($\pm$ 0.1 kV/cm) corresponding to a mechanical tolerance of $\pm$ 100 μm. The resulting effective gain variation (δG_{drift}) is $\pm$ 1%.

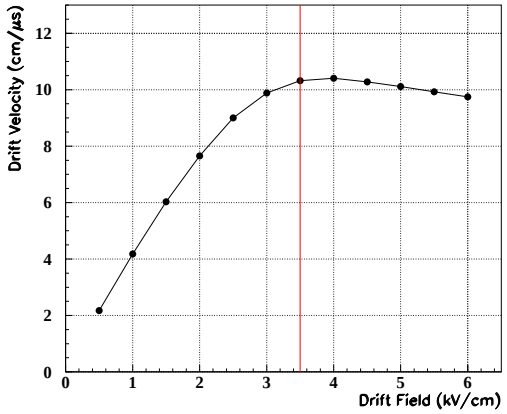

Figure 4.23: Electron drift velocity as a function of the drift field. The maximum drift velocity is reached when the drift field is set at 3.5 kV/cm.

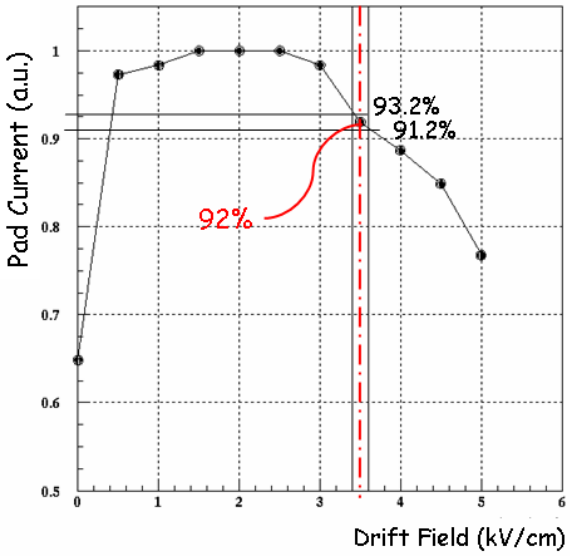

Figure 4.24: Normalized pad current of the detector as a function of the drift field. For a mechanical tolerance of $\pm$ 100 μm, the effective gain changes of about $\pm$ 1%.

The electric field of the first transfer gap is set to 3.5 kV/cm as a compromise between high transparency and low discharge probability. The latter is shown in Fig. 4.25 for different value of the first transfer field measured with an α source. With a field of 3.5 kV/cm, the discharge probability results to be a factor of three less than that one obtained with 4.5 and 5 kV/cm [57]. This is due to a larger *extraction fraction* on the second multiplication step corresponding to a grater possibility to reach the Reather limit.
A mechanical tolerance of $\pm$ 100 μm for the first transfer gap, that is 1 mm thick, corresponds to a transfer field change of $\pm$ 0.35 kV/cm. Such a variation results in a gain variation (δG_{tran1}) of $\pm$ 3% (Fig. 4.26).

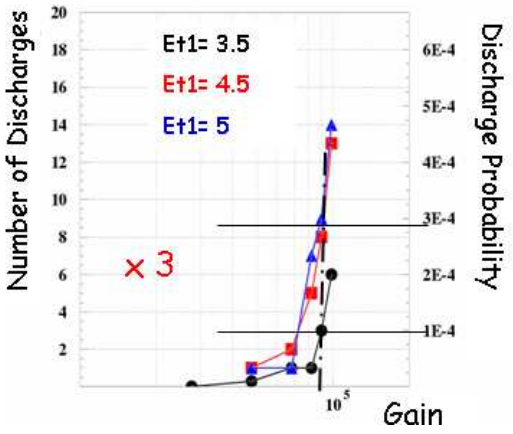

Figure 4.25: Discharge probability as function of the effective gain for different values of the first transfer field measured with an α source [57].

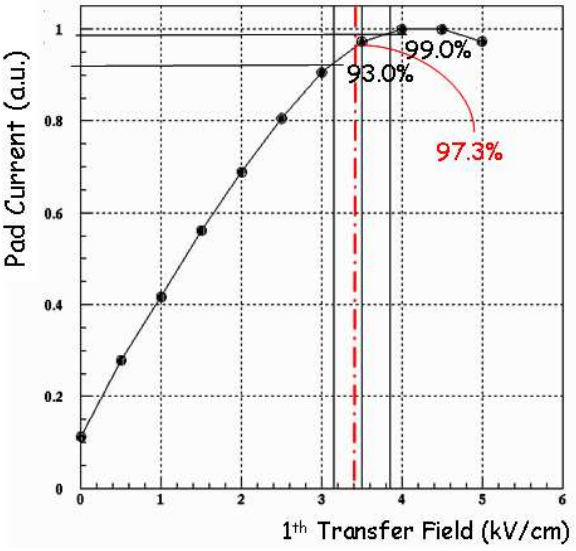

Figure 4.26: Normalized pad current as a function of the first transfer field. For a mechanical tolerance of $\pm$ 100 μm, the effective gain changes of about $\pm$ 3%.

At the same way, the second transfer field is set to 3.5 kV/cm as a compromise between high transparency and low discharge probability. As for the first transfer field, an electric field of 3.5 kV/cm ensures a discharge probability which is factor of two less than that one obtained with higher values [57] (Fig. 4.27).
For the second transfer field, a mechanical tolerance of $\pm$ 100 μm, which is 2 mm thick, is equivalent to a variation of the second transfer field of $\pm$ 0.18 kV/cm, corresponding to gain variation (δG$_{tran2}$) of $\pm$ 3%, as shown in Fig. 4.28.

The induction field allows to adjust the charge sharing between the pad and the bottom electrode of the third GEM. Fig. 4.29 shows the current sharing on the pad and the bottom electrode of the third GEM as a function of the induction field. Due to the quite steep dependence of the effective gain on the induction field, a mechanical tolerance of $\pm$ 100 μm, 1 mm thick, corresponds to an induction field variation of $\pm$ 0.5 kV/cm, inducing a gain changes, δG$_{ind}$, of the order of $\pm$ 4%.

In Tab. 4.3 the single contributions to the gain variation coming from each single gap are

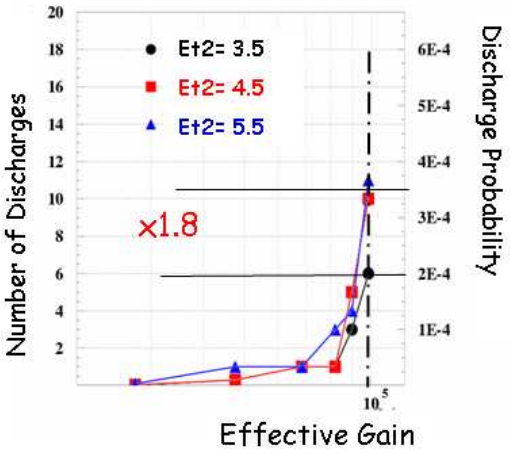

Figure 4.27: Discharge probability as a function of the effective gain for different values of the second transfer field measured with an α source [57].

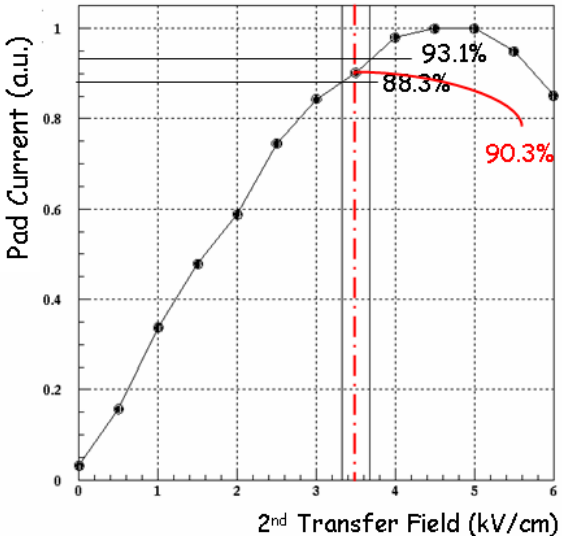

Figure 4.28: Normalized pad current as a function of the second transfer field. For a mechanical tolerance of $\pm$ 100 μm, the effective gain changes of about $\pm$ 3%.

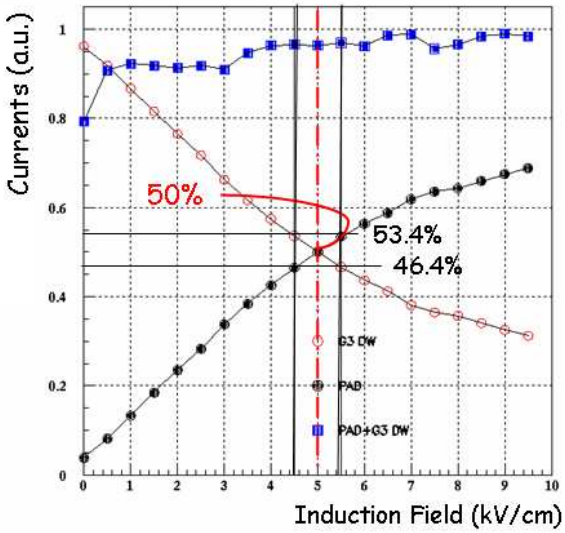

Figure 4.29: The current sharing on the pad (in red) and on the bottom electrode of the third GEM (in black) as a function of the induction field. A mechanical tolerance of $\pm$ 100 μm produces an effective gain variation of $\pm$ 4%.

summarized. The global effect, ΔG_{eff}, obtained as the squared sum of each single contribution comes out to be of the order of $\pm$ 6%.
As comparison between this estimation and a direct measurement of the gain uniformity of our chamber will be reported in the next section.

	Gap Thickness [mm]	E_{field} [kV/cm]	δE_{field} (δ gap = $\pm$ 100 μm) [kV/cm]	δG_{eff} [%]
Drift	3	3.5	0.1	1
1^{st} transfer	1	3.5	0.35	3
2^{nd} transfer	2	3.5	0.18	3
Induction	1	5.0	0.5	4
			Total Δ G_{eff}	*6*

Table 4.3: Summary of the gain variation due to a mechanical tolerance of $\pm$ 100 μm in each gap of the detector.

4.3.3 Quality check

Several quality check are performed, before the chamber assembly, on different detector components. Among these tests, in the previous sections I discussed the GEM foil tests and the planarity check performed on PCB panels. After the chamber construction, the detector tightness and its gain uniformity are measured.

Gas leak test

In the experiment the gas mixture will be supplied in parallel for the 12 detector stations with an open flow system. A gas leak could imply an undesirable contamination of the gas mixture with H_2O and O_2. Taking into account the large amount of CF_4 (40%) presents in the gas mixture, a small fraction of water could give rise to the formation of hydrofluoric acid (HF), which will etch the detector electrodes.
The setup of such a test is shown in Fig. 4.30. The gas leak rate measurement of a chamber is referred to that one of a reference chamber, of same volume and with a negligible gas leak ($<$ 1 mbar/day), in order to take into account for atmospheric pressure and temperature

variations. To ensure a good thermal insulation both chambers are placed in a foam box. The test begins inflating in parallel, up to an overpressure of $\sim$ 10 mbar, the two chambers and measuring their relative overpressure variations through two distinct probe. The gas leak of test chamber is measured by the difference value of the two probes (Fig. 4.31).

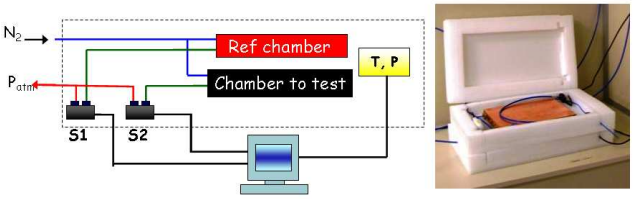

Figure 4.30: Gas leak setup.

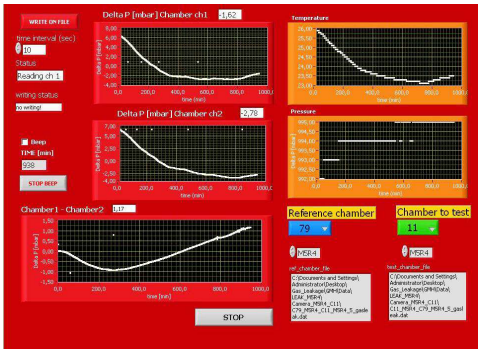

Figure 4.31: Monitor display of the leak rate measurement.

The typical gas leak rate of a chamber is of the order of few mbar/day, as shown in Fig. 4.32, corresponding to a humidity level of $\sim$ 50 ppm per volume for a gas flow rate of 80 cc/min (as foreseen in the experiment).

Gain uniformity measurements

In order to check the uniformity response two kinds of tests are carried out after the gas tightness measurement. The first test is performed on a single chamber, while the second is executed on the whole station.

The uniformity gain test allows to check both the mechanical tolerance and the uniformity response of a single chamber. This test is performed with an X-ray gun (Fig. 4.33). The current signal induced on each pad, 192 pads per chamber, is read-out with a 1 nA sensitivity current-meter and corrected for the temperature and the pressure variations. The water content and the temperature of the gas mixture are monitored with a probe mounted on the gas line outlet. The atmospheric pressure is monitored outside the gas line with another probe. The chamber is mounted on a X-Y plane moved with computer controlled step-motors. The measured gain uniformity is shown in Fig. 4.34. Taking into account the pad size (25$\times$10

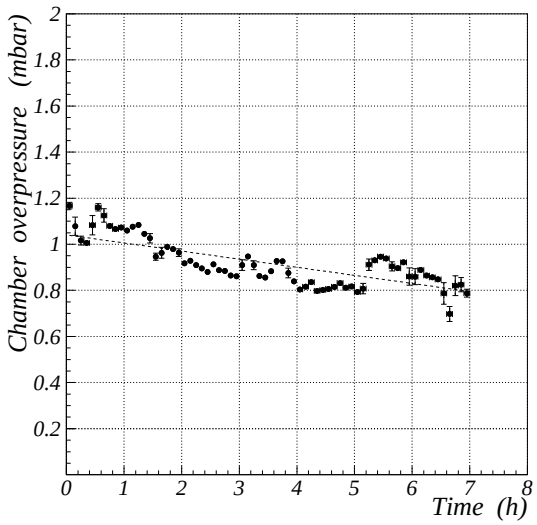

Figure 4.32: Gas leak rate as a function of the time. A rate less than 1 mbar per day is achieved. This value corresponds to a humidity level of $\sim$ 50 ppm per volume with a flow rate of 80 cc/min.

mm^2), the diameter of the X-ray collimator ($\sim$ 5 mm) and the X-ray beam spread, the small gain losses are due to a not full illumination of the 64 border pads.

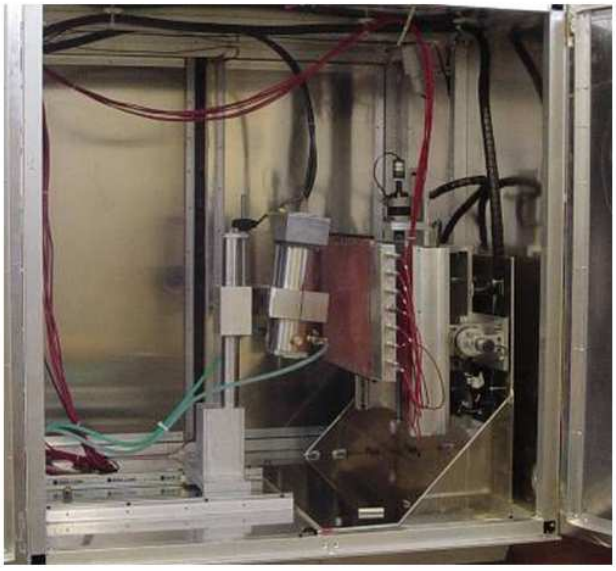

Figure 4.33: Picture of the X-ray tube.

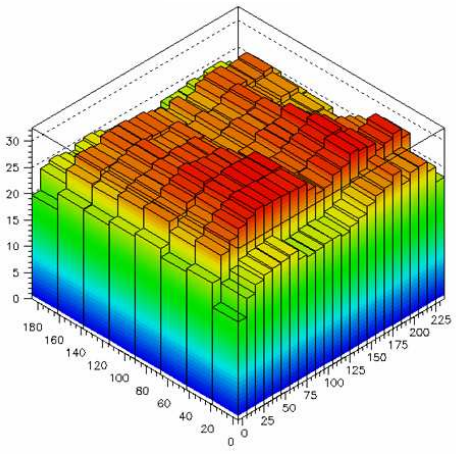

Figure 4.34: The gain uniformity measurement performed on a single chamber.

The measured gain uniformity with and without the border pads are better than 12% and 6% respectively (Fig. 4.35, 4.36).
Not considering the border pads of the readout, the measured gain uniformity is in good agreement with the estimation made in the previous section.

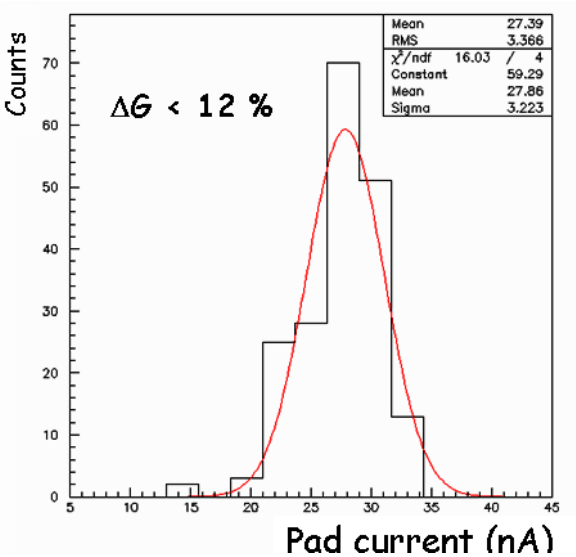

Figure 4.35: Gain uniformity distribution of all the 192 pads of a chamber.

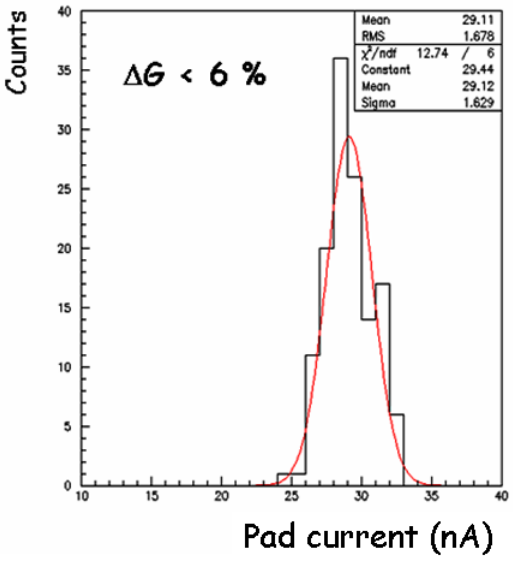

Figure 4.36: Gain uniformity distribution excluding the 64 border pads.

The second test allows to check the uniformity response of the whole station in terms of the efficiency (within 20 ns time window) and the pad cluster size. For this reason, two chambers are coupled through the four reference pin holes and with the cathodes faced one to each other. The faraday cage and the front-end electronics, based on the CARIOCA chip [31], are mounted on the four side of the station (Fig. 4.37). Taking into account the pad size of 10×25 mm^2, 384 electronic channels are needed to readout the whole station.
The performances of the station are tested with a cosmic ray setup, as shown in Fig. 4.38. The trigger is the coincidence of two scintillator layers which cover all the active area of the station. They are 1 m far and before the lower scintillator a thickness of 10 cm of lead ($\sim$ 18 X_0) are used to select muons. To avoid geometrical inefficiency and to ensure a high tracking of muons, two layers of drift tubes are placed above and the below the detector station. The space resolution reachable with the drift tubes is better than $\sim$150 μm (r.m.s.).

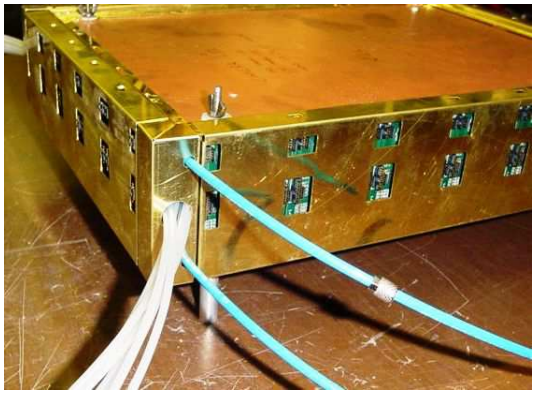

Figure 4.37: The detector station.

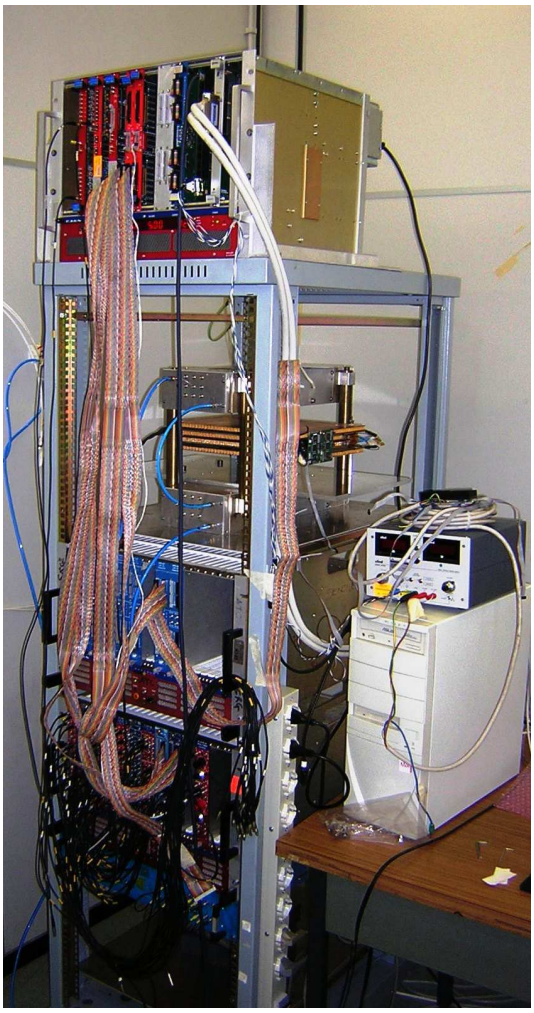

Figure 4.38: Picture of the cosmic ray setup used to measure the final station performances.

4.4 Triple-GEM detector performance

4.4.1 Global ageing test

In M1R1 region a triple-GEM detector must tolerate, without damage or performance losses, an integrated charge of $\sim$ 1.8 C/cm^2 in 10 years of operation at a gain of $\sim$ 6000 and an average particle flux of $\sim$ 184 kHz/cm^2 for an average machine luminosity of $\mathcal{L}$ = 2$\times$10^{32} cm^{-2}s^{-1} [1].

Local aging test on small size detectors (10$\times$10 cm^2 active area) operated with Ar/CO_2/CF_4 (45/15/40) gas mixture was performed with a high intensity X-ray tube. As shown in Sec. 3.7.5, after an integrated charge equivalent to $\sim$ 11 years of operation at LHCb (for a particle rate of 460 kHz/cm^2), negligible aging effects were observed ($<$ 5%).
Anyway, due to the large amount of CF_4 (40%) present in the gas mixture, in order to check the compatibility between the construction materials (both for detector and gas system) and the gas mixture, a global irradiation test of the full size detector station is required.
For this reason we performed a test at the Calliope facility of the ENEA-Casaccia.

Setup of the test

The Calliope plant is a pool-type irradiation facility equipped with a ^{60}Co radioisotope source placed in a shielded cell. The emitted radiation consists of photons with an energies of 1.17 MeV and 1.33 MeV. The activity at the time of the test was $\sim 8\times10^{14}$ Bq (June, 15th, 2003). In Fig. 4.39 is shown the Calliope plant with the arrangement of the chamber inside the irradiation hall.

Three full size prototypes were irradiated at different gamma doses corresponding to m.i.p. fluxes of $\sim$ 1 MHz/cm^2 for one chamber (that we call chamber "C"), $\sim$ 15 MHz/cm^2 for a second chamber (chamber "A"), and 20 MHz/cm^2 for a third chamber (chamber "B"), as shown in Fig. 4.40.
Because of the very high current drawn by the detectors under irradiation, to reduce the volt-

[1] The integrated charge in 10 years of LHCb running (Δt_{LHCb}) is estimated as follows:
$Q_{LHCb}^{integrated} = 2 \cdot \Phi_{LHCb} \cdot \Delta t_{LHCb} \cdot e \cdot N \cdot G$, where the factor 2 takes into account the current on the pad readout and the bottom electrode of the third GEM, Φ_{LHCb} is the average charged particle flux expected flux in M1R1 (184 kHz/cm^2), *e* is the electric charge (1.6$\times$10^{-19} C), *N* is the specific ionization that is estimated to be $\sim$ 40 electron-ion pair and *G* is the gas gain.

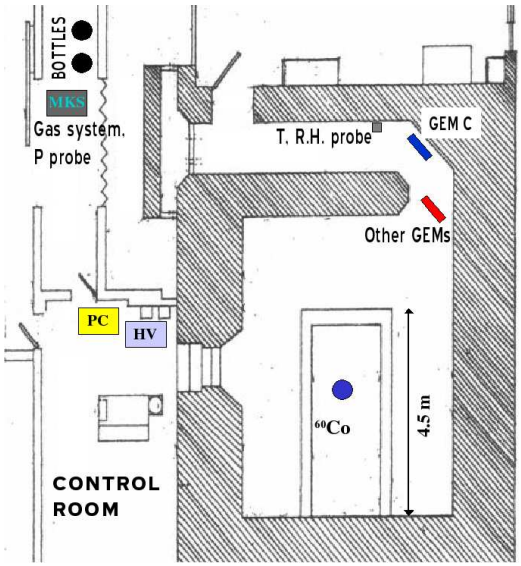

Figure 4.39: Map of the irradiation cell.

Figure 4.40: Position of the chamber during the test. On top of the blue rack was placed the chamber A and B. On the black rack, where the radiation flux was less intense, was placed the chamber C.

age drop in the GEMs foils down to few volts, the chamber A and B were equipped with 100 kΩ limiting resistors, while 1 MΩ limiting resistors have been used for the lowest irradiated chamber C.

Since the irradiation hall had a high humidity level due to the presence of the water pool, the gas distribution system was realized with suitable materials. The whole gas inlet line was made of stainless-steel tubes, while the exhaust gas line was made of polypropylene tubes (not hygroscopic). The gas flow rate was 350 cm^3/min, to be compared with the single

detector volume of $\sim$ 350 cm^3. The lowest irradiated detector was used as reference chamber and installed upstream in the same gas line of the high irradiated detectors. A probe was directly installed on the gas line, downstream the test chambers, in order to monitor the temperature and humidity of the gas mixture (Fig. 4.41). The water content in the gas mixture was substantially kept under few tens of ppm during the whole test. An additional probe supplied the monitor of the atmospheric pressure.

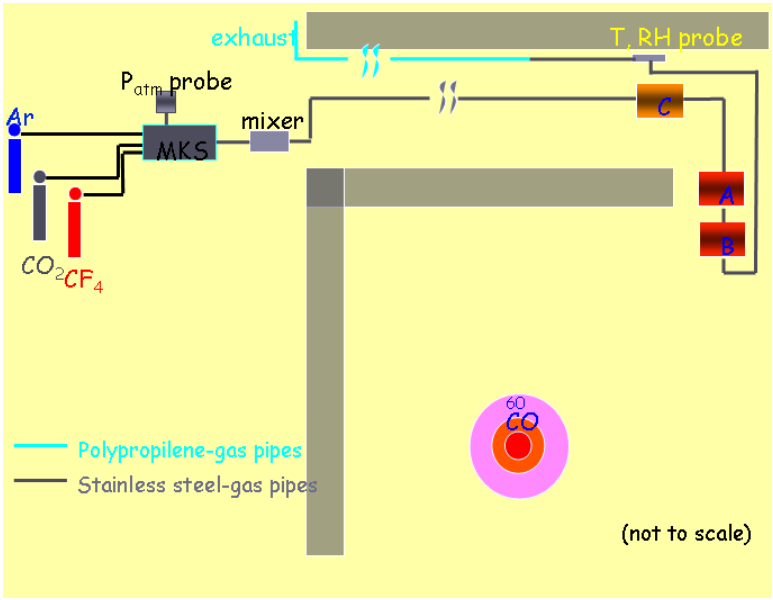

Figure 4.41: Sketch of the gas system.

The temperature and the atmospheric pressure variations were used to correct the gas gain of the chamber, according to the following empirical relation:

$$G \propto e^{<\alpha> V_{GEM}^{tot}} \cdot e^{\beta T/p} \tag{4.2}$$

where the parameters, $<\alpha>$ = 17$\times 10^{-3}$ V^{-1} [2] and β = 40 mbar/K, have been previously measured in laboratory with the X-ray.
During the test the working voltage was set to V_{GEM}^{tot} = 1280 V, corresponding to a gas gain of $\sim$ 6$\times 10^3$ at T = 300 ^{o}K and p = 990 mbar.

[2]This value of the Tonwsend coefficient differs from that obtained in Sec. 3.7.1 because in that test was not taken into account for the T/p variations.

Test results

The detector have been irradiated for a period of 35 days. The total accumulated charges by the three prototypes were $\sim$ 0.16 C/cm^2 for the lowest irradiated detector, $\sim$ 1.6 C/cm^2 and $\sim$ 2.2 C/cm^2 for the highest irradiated ones, corresponding respectively to about 1 (chamber C), 8.5 (chamber B) and 11.5 (chamber A) years of operation at LHCb. At the end of the test chamber C has shown no aging, while current drops of $\sim$89% and $\sim$80% were observed respectively for chamber A and B, as shown in Fig. 4.42.

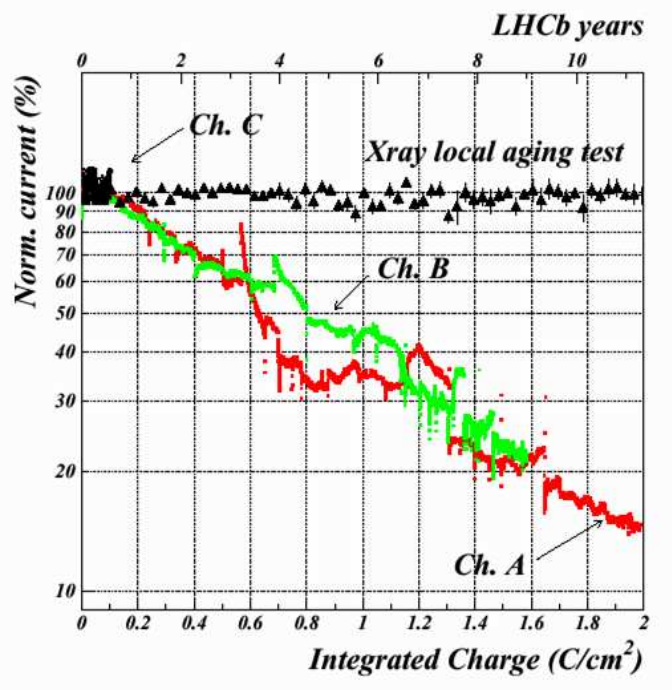

Figure 4.42: Comparison between local aging and the global irradiation test at the ENEA-Casaccia.

The result obtained in this test has been attributed to the insufficient gas flow rate (350 cm^3/min, the maximum flow reachable with our mass-flowmeters) with respect to the very high gamma ray flux (up to 15-20 MHz/cm^2 equivalent m.i.p. on the whole detector area, corresponding to a pad current of the order of 400-500 μA) at which chambers were exposed during the irradiation test.
On the contrary, local tests were performed in completely different experimental conditions: a gas flow rate of 100 cm^3/min for a global detector current of 0.4-0.2 μA (over an irradiated

area of the order of 1 mm^2).
In this framework we believe that the global irradiation test has been performed in strong *gas pollution* conditions and then should be considered pessimistic and misleading. In fact, the chambers were probably submitted to a strong plasma etching by fluorine, produced in the fragmentation of the CF_4, and not quickly removed by the gas flow. As a consequence, permanent changes should be found on the GEM foil, in particular on the GEM holes diameter and probably also on the holes shape, especially on the third GEM foil, where the charge density is larger.
Several checks and measurements successively done on the aged chambers support such hypothesis.

Gain and rate capability measurements on aged chambers

The gain of the aged chambers has been measured with a X-ray source at a relatively low particle flux of ~ 1.6 MHz/cm^2.

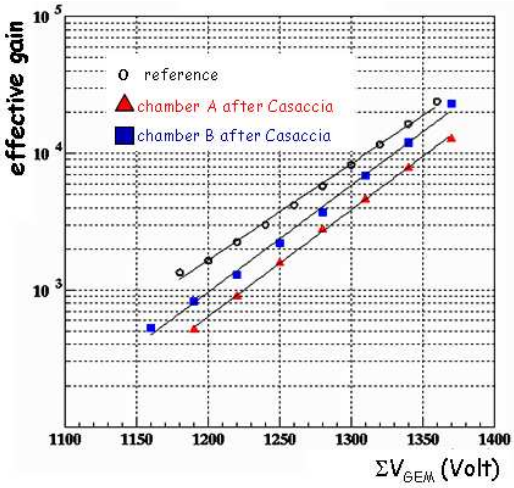

Figure 4.43: Comparison between the gain measured on a new GEM detector and the gain measured on chamber A and B after the Casaccia aging test.

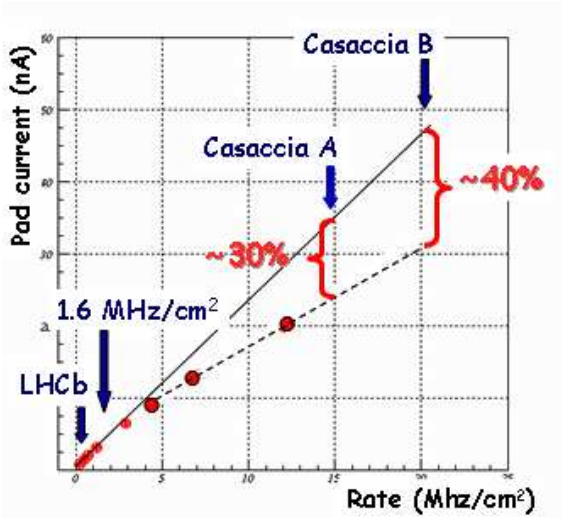

Figure 4.44: Rate capability loss of aged chamber A and B.

In Fig. 4.43 is shown the comparison between the effective gain of the chambers before (empty circles) and after (full triangles for chamber A, full squares for chamber B) the global irradiation test. The gain reduction is $\simeq 55\%$ for chamber A, and $\simeq 32\%$ for chamber B. In

	Chamber A	Chamber B
Gain reduction	$\sim 55\%$	$\sim 32\%$
Rate reduction	$\sim 30\%$	$\sim 40\%$
Total reduction	$\sim 85\%$	$\sim 70\%$

Table 4.4: Summary table of the gas gain and rate reduction performed with the X-ray tube. The sum of the two effects is comparable with the gain drop observed at the end of Casaccia test.

addition, as shown in Fig. 4.44, the chambers A and B exhibit a considerable rate capability reduction at high particle fluxes (for a not-aged detector a rate capability at least of ~ 50MHz/cm^2 has been previously measured). In particular, a simple linear extrapolation of the last two measured points (full circles) up to the particles fluxes at which the chamber A has been operated during the global irradiation test (15 MHz/cm^2), indicates a gain drop of $\sim 30\%$ ($\sim 40\%$ for chamber B, considering the same loss of linearity of the rate capability of chamber A).
These results are compatible with the current drops observed at the global irradiation test and are summarized in Tab. 4.4. In fact, for chamber A the gain drop of 55% at low rate, and the loss of linearity of the rate capability at 15 MHz/cm^2 of 30%, explains the current drop of 89% .

It should be stressed that the rate capability is fine up to 3-4 MHz/cm^2, well above the LHCb requirements for M1R1 (the maximum particle flux in M1R1 is ~ 500 kHz/cm^2).

Beam test results on aged chambers

The performances of the two chambers, A and B, were measured before the global irradiation test at the electron beam facility (BTF) of the Frascati Laboratory in the spring 2003. After the aging test both chambers have been again tested at the PS beam facility at CERN in the autumn of the same year. Both tests have been performed at a particle flux of ~ 100 kHz/cm^2, close to the average particle flux foreseen at the LHCb experiment. We thus had the possibility to compare the performances of the chambers before and after the global irradiation test. The results show that aged chambers exhibit practically the same performance in terms of efficiency in 20 ns time window as before their irradiation, except for a moderate shift toward higher voltages, of the working points. For chamber A the shift of the operating

voltage, Fig. 4.45 (top), is about 15 V, while for chamber B the shift is negligible. For a station made with these two detectors logically OR-ed, the efficiency in 20 ns time window is practically unaffected, Fig. 4.45 (bottom).

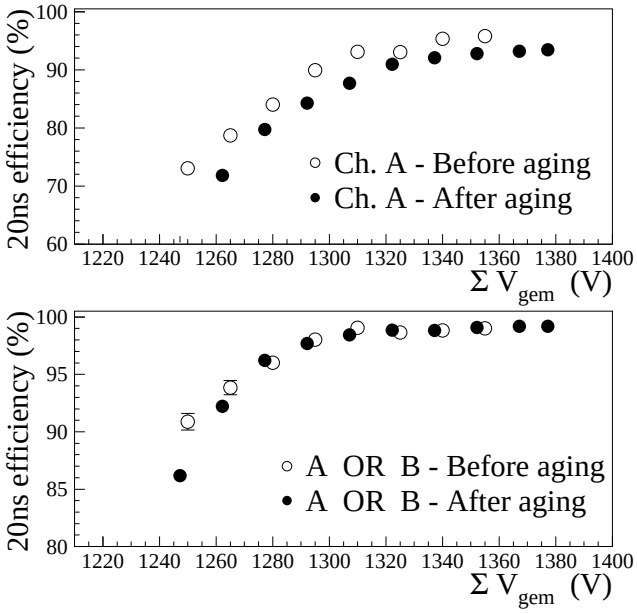

Figure 4.45: Efficiency in 20 ns time window before and after irradiation: (top) for chamber A; (bottom) for the two chambers logically OR-ed

SEM analysis and X-ray spectroscopy on aged chambers

In order to understand the etching mechanism occurred during the global irradiation test, a scanning electron microscope (SEM) analysis has been performed on various samples of the aged chambers.

The results obtained are clearly compatible with a fluorine etching: no polymerization deposits (typical of the so called classical aging [69]) have been observed on the surfaces. As expected the etching effects are larger on the third GEM foil, minor effects are found on the second GEM, while the first GEM does not present any appreciable etching effects, see Fig. 4.46. As shown in Fig. 4.47, on both third and second GEMs the observed effect consists of a appreciable widening of the external (copper) holes diameter, from the standard 70 μm

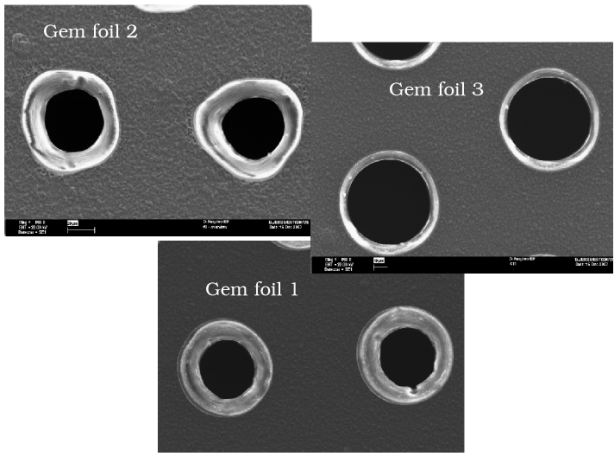

Figure 4.46: Picture of the three gem foils. The widening of the holes from the first to the third foil is visible.

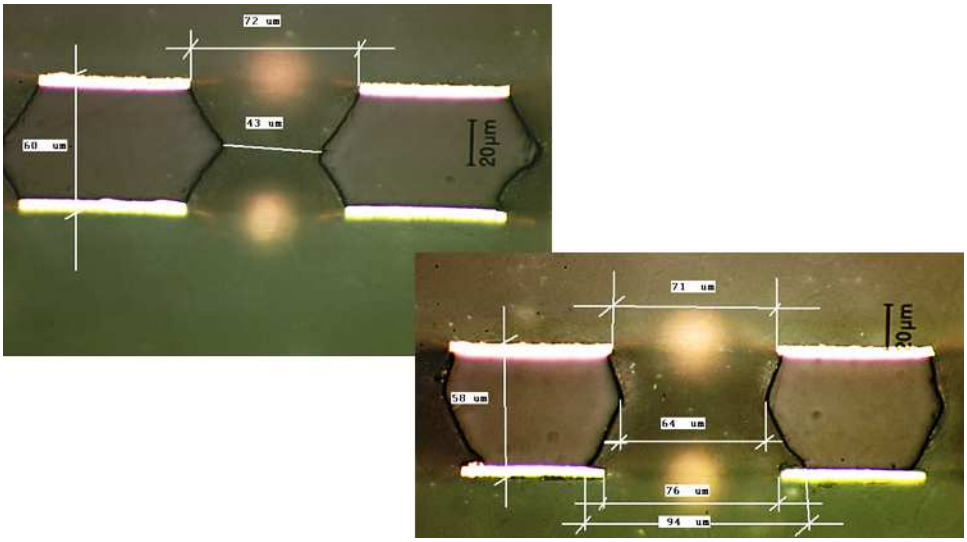

Figure 4.47: Cross section of first GEM foil (left) and third GEM foil (right) of chamber A.

up to 80 μm. In addition on the third GEM, where the etching processes were clearly larger, also the kapton inside holes has been etched: the internal hole diameter from the standard 45-50 μm becomes 60-65 μm.

Fluorine has been found only on the bottom surface (where negative ions and electrons are collected) of the third and second GEM, being larger on the third GEM and smaller on the second one. In Fig. 4.48 the comparison between the X-ray spectra done on the bottom surfaces of the three GEM foils are shown. Fluorine is mostly located on the copper around

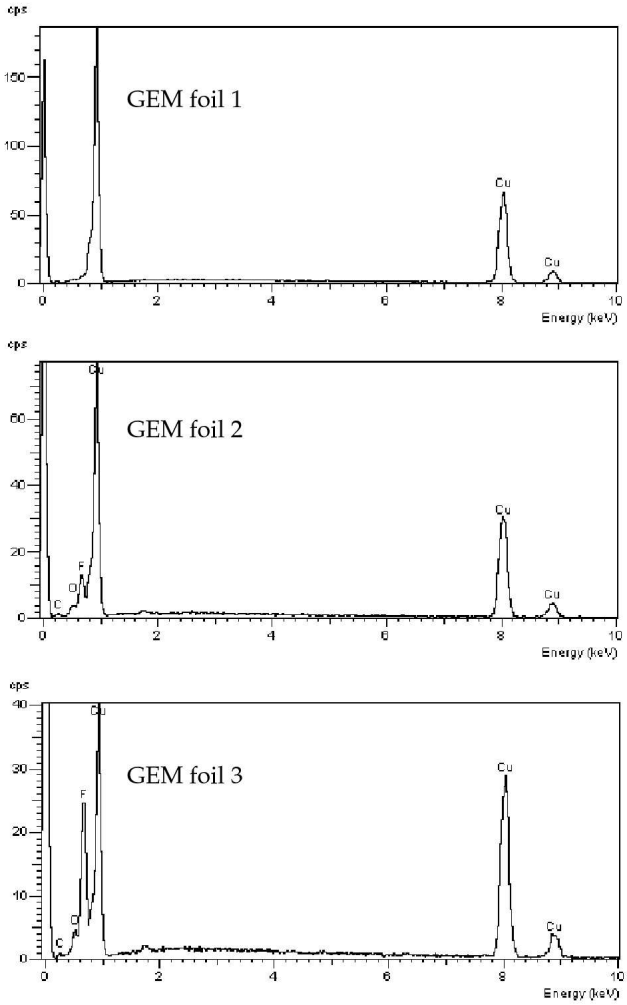

Figure 4.48: X-ray spectroscopy of the bottom surfaces of the three GEM foils of chamber A: no fluorine on the first GEM foil, small deposit on the second GEM foil and larger deposit on the third GEM foil.

the holes edge, leading to the formation of a thin non conductive layer (a fluorine-copper compound). The Fig. 4.49 shows the comparison between the X-ray spectroscopy of the top and bottom surfaces of the third GEM foil of the Chamber A.

In Fig. 4.50, 4.51 and 4.52 the comparison between the etching effects found on the third GEM foils of the two chambers are shown (A and B respectively). The holes of chamber A are clearly more etched than those of chamber B, in agreement with the observation of larger fluorine deposits. During the global irradiation test chamber A accumulated the largest quantity of charge (~ 2.2 C/cm^2).

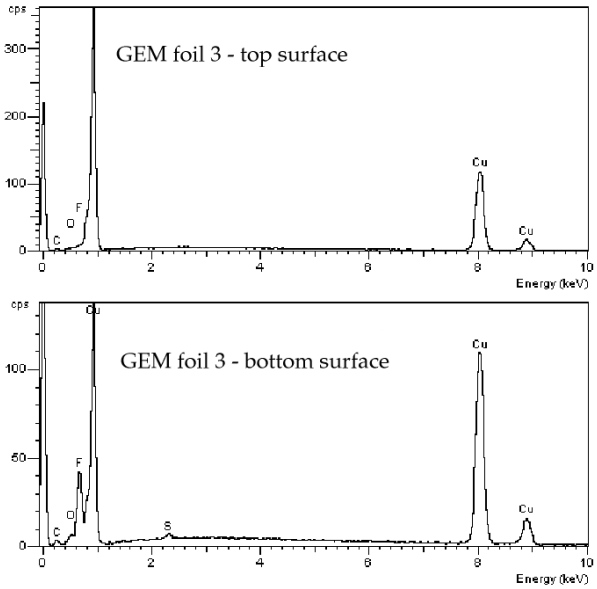

Figure 4.49: X-ray spectroscopy of the third GEM surfaces (top and bottom respectively) near the hole edge shows presence of fluorine only on the bottom surface.

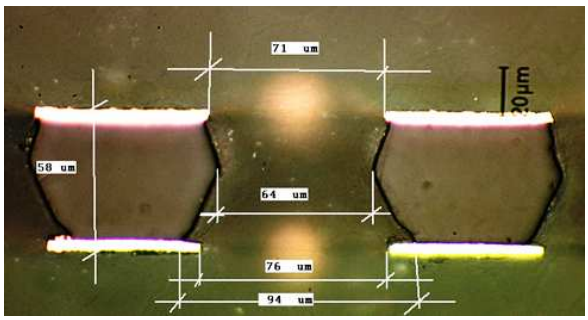

Figure 4.50: Cross section of third GEM foils of the chamber A.

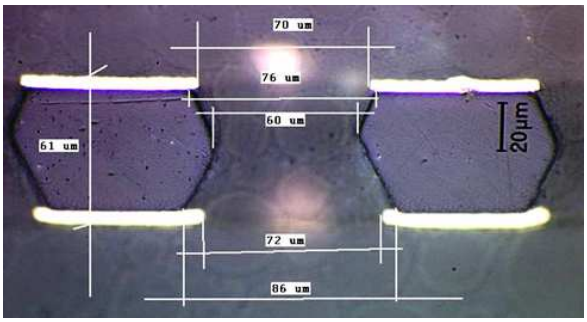

Figure 4.51: Cross section of third GEM foils of the chamber B.

The cathode (drift electrode) and the anode (the pad PCB) were found perfectly clean. The results of the SEM analysis give a reasonable explanation of the observed effects:

- the enlargement of GEM holes leads to a decrease of the gas gain [51];
- while the etching of the kapton inside the holes and the non conductive layer on the copper near the hole edge, enhance charging-up effects, reducing the rate capability of the detector.

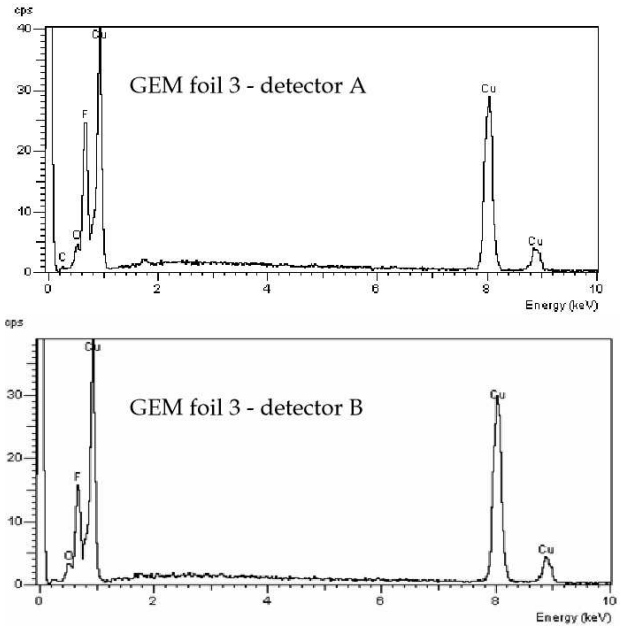

Figure 4.52: Comparison between the X-ray spectroscopy of the bottom surfaces third GEM foils, of the chambers A and B; larger fluorine deposit has been found on chamber A.

Finally, in order to demonstrate that the etching observed at the global irradiation test was essentially due to an insufficient gas flow rate compared with the high irradiation level, we reproduced such conditions irradiating with a high intensity X-rays beam a 10×10 cm^2 prototype, flushed with a reduced gas flow, Fig. 4.53. The current drawn by the chamber was about 1 μA on a 1 cm^2 irradiated area, while the gas flow was $\sim$ 20 cm^3/min. In such conditions we observe a permanent gain drop of about 40% in $\sim$3 LHCb equivalent years.
The test, repeated with a gas flow of $\sim$ 200 cm^3/min and with a current of 0.5 μA on a 1 cm^2 irradiated area, gave a result compatible with no aging in about 10 LHCb equivalent years.

Global ageing test conclusion

The results of the severe and systematic tests performed on triple-GEM detectors, indicate that the detector is robust and can tolerate the radiation dose foreseen in 10 years of operation in the region M1R1 of the LHCb experiment: detectors, even after a severe irradiation in very bad conditions, exhibit good time and efficiency (in 20 ns) performances, except for a shift of about 15 V on the working point for a single detector, while for two detector logically OR-ed the performances are practically unchanged.

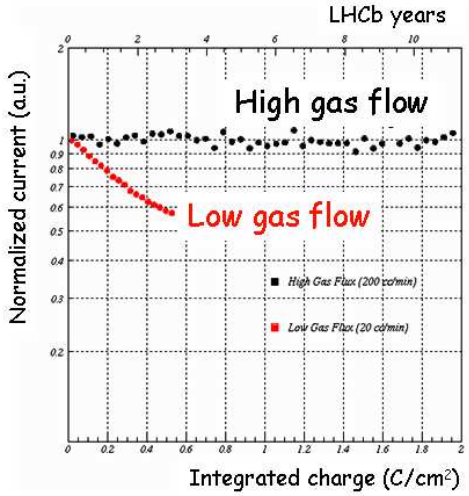

Figure 4.53: Comparison between the aging measured on a small prototype with low gas flow ($\sim$ 20 cm^3/min) and high gas flow ($\sim$ 200 cm^3/min).

In addition the results of the global irradiation test, apparently in disagreement with the other aging tests previously performed, have been understood. We have demonstrated that the etching observed during this test is clearly correlated with bad gas flow rate conditions. No etching occurs if the gas flow is properly set. In the LHCb running conditions, where the average current collected on pads by one full size chamber will be of the order of 5μA, a safe gas flow rate could be $\sim$ 80-100 cm^3/min.

4.4.2 Test beam results at PS-CERN beam facility

The test has carried out in the T11 area of CERN PS with pions of $\sim 3 \div 4$ GeV/c. The experimental setup is shown in Fig. 54(a). The coincidence of scintillators S1, S2, S3 and S4 has been used to give the trigger signal to the DAQ system.
The S1 and S2 scintillators had an area of 15×15 cm^2 and 20×20 cm^2 respectively.Two 0.5×0.5 cm^2 scintillator fingers (S3 and S4) have been used to select a small beam spot area for fine scanning over a single readout-pad (Fig. 54(b)).
The S1 and S4 signals have been sent to a constant fraction discriminator and the coincidence of the discriminator outputs has been delayed to give the common stop to the TDC, with a resolution of ~ 0.5 ns (r.m.s.). To avoid showering particles, a cut on the ADC counts of the S1 and S4 has been applied.

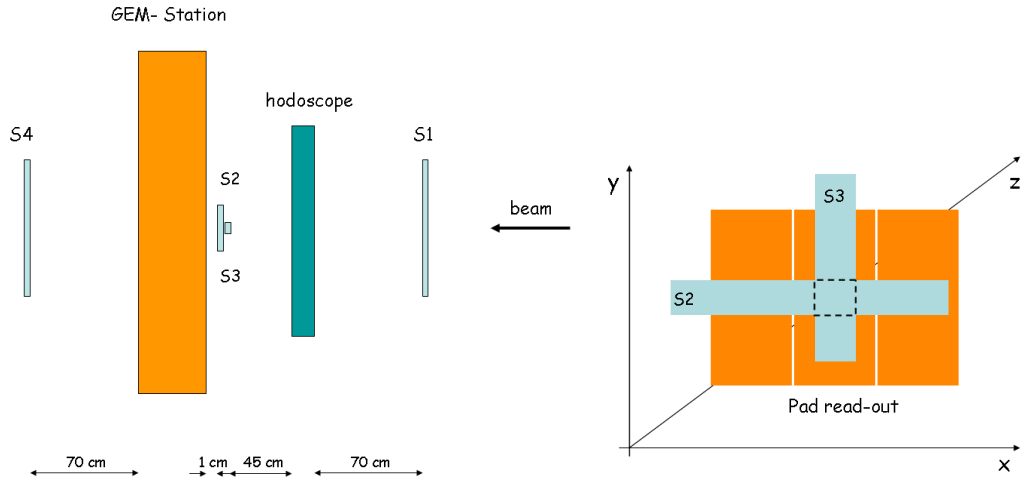

(a) View along the beam direction.

(b) View in the $x - y$ plane.

Figure 4.54: The setup at T11 area.

The information from 8 horizontal and 8 vertical strips (8 cm long and 1 cm wide) of a hodoscope has been used in the data analysis to identify the beam position with respect to a pad of the station. The two projections in the x and y direction are gaussian distributed with $\sigma_x = \sigma_y \sim 1.3$ cm.

The pad signals of the GEM station have been discriminated on front-end boards (FE) and sent to TDCs. Since in this test the DIALOG chip, which form the OR of the two output signals coming from the two chambers, was not yet available, the OR has been performed at the data analysis level. It should be stressed that the two output signals, which are compared, has been always recorded on the same TDC. Moreover, the DIALOG chip will allow to delay one of the two output signals with steps of 1.5 ns before the OR operation. This possibility has been also added in the data analysis considering the delay which minimize the time resolution of the two OR-ed chambers. During the tests, we used front-end electronics based on the ASDQ++ chip with a the discrimination threshold of $\sim$ 2 fC. The ASDQ++ chip has a sensitivity of 25 mV/fC, a peaking time of 10 ns and an electronic noise charge of about 1700 e^- r.m.s at zero input capacitance.

The electrodes of the two coupled chambers have been supplied separately in order to easily scan over the whole HV operating range. It should be stressed that in the experiment the whole station will be supplied by two distinct HV divider (one per chamber).
To assure a statistical error below 1% on the efficiency measurement, up to 10^4 events were acquired for each HV setting.

In the following sections, the measure of the geometrical cluster size and efficiency in 20 ns time windows are presented. I remark that a detector station, i.e. two chamber logically OR-ed, must have an efficiency in 20 ns time window grater than 96% and a geometrical cluster size, i.e. the average number of pads above the electronics threshold, less than 1.2 for a pad size of 10×25 mm^2.

Pad layout choice

As discussed in Sec. 4.2.1, two pad readout configurations, one with a ground grid of 100 μm between the pads and the other without, have been investigated during a dedicated test beam (May 2004).

Since in the experiment the particles will uniformly cross the detector active area, the geometrical pad cluster size must be determined as an average of millimetric scan along the pad size. The measurement has been performed by moving the detector station with steps of $\sim$ 1 mm in the x direction, as shown in Fig. 54(b), and selecting the beam spot by means of scintillator fingers, requiring the hodoscope coincidence.

Fig. 4.55 shows the pad cluster size and the efficiency in 20 ns time window as a function of the impact position of the particle for each chamber at a gas gain of ~ 6000. The upper plot refers to the chamber without the ground grid, while the bottom one refers to the chamber with the ground grid.

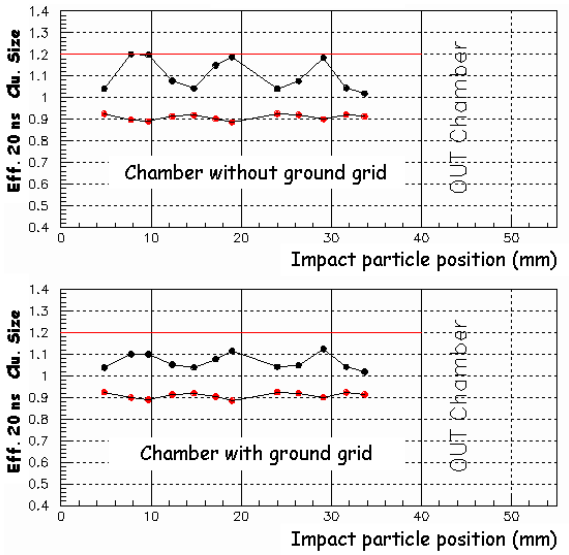

Figure 4.55: The pad cluster size (black point) and the efficiency within 20 ns time window (red point) as a function of the impact particle position for two chambers with different pad readout.

The millimetric scan has been repeated for different voltage setting (i.e. detector gas gain) and the average of the pad cluster size and the efficiency in 20 ns time window has been determined considering the scanned pads.
Fig. 4.56 shows the average geometrical pad cluster size and the average efficiency in 20 ns time window as a function of V_{GEM}^{tot} for the two chambers.

The use of a ground grid allows to obtain a good efficiency in 20 ns time window, while reducing the average geometrical pad cluster size with respect to that one found without the ground grid. This effect is due to the transverse dimension of the electron cloud, which depends on gas gain: for larger signals a larger induction on the adjacent pads is observed, increasing the pad cluster size. Adding a ground grid between pads allows to collect part of the electron charge on the grid, reducing the induction on the adjacent pads, while keeping efficiency unchanged.

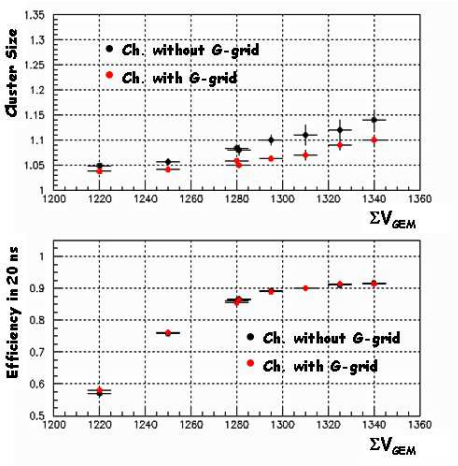

Figure 4.56: Average geometrical pad cluster size and average efficiency in 20 ns time windows as a function of V^{tot}_{GEM} for the pad readout with a ground grid (red points) and without the grid (black points).

Efficiency and geometrical pad cluster size in 20 ns time window

A test of the detector with the final readout configuration (pad readout with a ground grid) has been performed in November 2004.
Fig. 4.57 shows the pad cluster size and the efficiency within 20 ns time window as a function of the impact position of the particles for each chamber at a gas gain of ~ 6000.

These plots show how the choice to enlarge the GEM active area with respect to the area of the cathode and the pad readout (see Sec. 4.2.2) allows to keep high efficiency up to 1 mm outside of the pad readout. Therefore in the overlap of two detector stations, as foreseen in the experiment, no efficiency losses will occur.
The average pad cluster size and the average efficiency in 20 ns time window as function of the gas gain for the OR of the two chambers are reported in Fig. 4.58.

We define, as the onset of the plateau [3] of the station, the value of the gain which corresponds to 96% efficiency within 20 ns time window. The end of the plateau is defined by the maximum pad cluster size (i.e. 1.2) allowed by the experiment requirements. The resulting plateau, in terms of the gain, ranges from ~ 5500 to ~ 18000, corresponding to ~ 80 Volts. It must be stressed that the maximum gain value of this working range (18000) corresponds to the safe and conservative value of the discharge probability of $\sim 5\times10^{-11}$, as discussed in Sec. 3.7.4.

[3] This term is used here with the meaning of the working range in which the GEM station satisfies the LHCb requirements

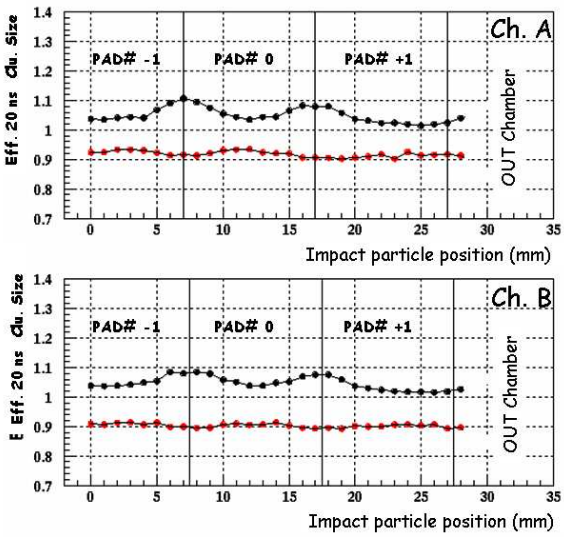

Figure 4.57: The pad cluster size and the efficiency within 20 ns time window as a function of the impact particle position for the chamber A (top) and the chamber B (bottom). The vertical line represents the boundary line of adjacent pads and the end of the active area.

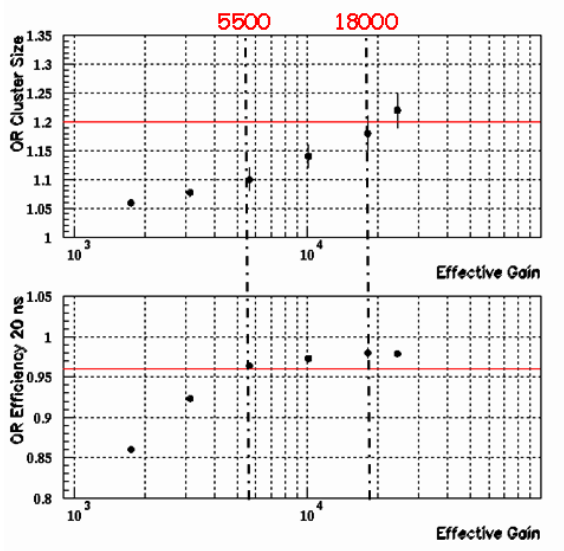

Figure 4.58: Detector station performances: the average pad cluster size (top) and the average efficiency within 20 ns time window (bottom) as a function of the gas gain.

The time distribution, Fig. 4.59, of the detector station (two chamber OR-ed pad by pad) at a gas gain of 1800 shows a time resolution of 2.9 ns (r.m.s.). This value represents the best time resolution reported in literature for a GEM based detector [73].

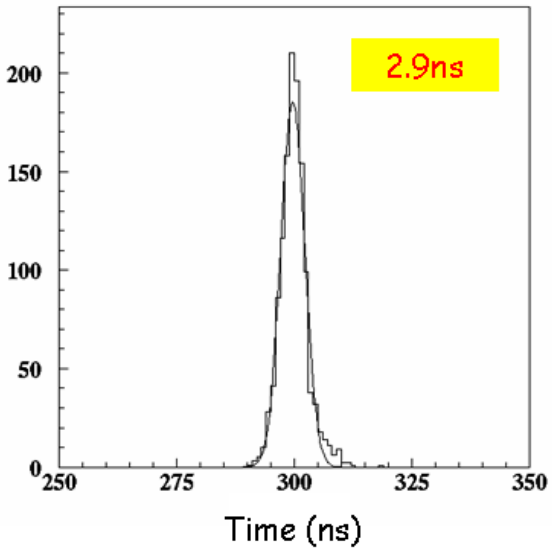

Figure 4.59: Time spectrum of the detector station for a gas gain of 18000 [73].

Electronics comparison

The results till now reported has been performed with the ASDQ++ chip. Since in the experiment the detector will be equipped with a front-end electronics based on the CARIOCA chip, a dedicated test with this electronics was required. It should be stressed that this CARIOCA version is designed for the MWPCs of the LHCb muon apparatus, so that not fully optimized for a GEM detector, for what concerns the gain of the pre-amplifier and tail cancellation and baseline restoration circuits, not required for the pure electronic signal of a GEM. In Tab. 4.5 the main parameters of both ASDQ++ and CARIOCA chips are summarized.

The detector station efficiency in 20 ns time window as function of V_{GEM}^{tot} for the ASDQ++ and the CARIOCA chips for the electronics threshold of $\sim$ 2 fC and $\sim$ 3 fC respectively, is reported in in Fig. 4.60.
A shift of $\sim$ 10 Volts in the plateau is observed with the CARIOCA chip as consequence of

Parameter	ASDQ++	CARIOCA
Peaking time	$\sim$ 10 ns	$\sim$ 10 ns (C_{det}=30 pF)
Input resistance	25 Ω	$< 50\,\Omega$
Average pulse width	< 50 ns	< 50 ns
ENC (r.m.s) for the negative amplifier	1750e$^-$+37e$^-\times C_{det}$ (pF)	2240e$^-$+42e$^-\times C_{det}$ (pF)
Sensitivity	$\sim$ 24.5 mV/fC	$\sim$ 16 mV/fC

Table 4.5: Front-end chip parameters [28].

the high electronics threshold, that for this version of the chip was not possible to reduce.

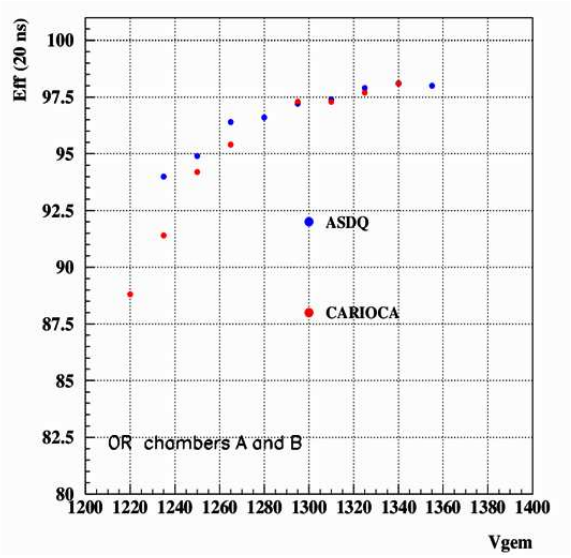

Figure 4.60: Detector station efficiency in 20 ns time window as function of V^{tot}_{GEM} for the ASDQ++ (blu points) and the CARIOCA (red points) chips for an electronics threshold of $\sim$ 2 fC and $\sim$ 3 fC respectively.

The positive results of this test enable us to design a new version of the CARIOCA chip, called CARIOCA-GEM, with the goal of reducing as much as possible the minimum electronics threshold, increasing the pre-amplifier gain. Moreover, the ion tail cancellation and the baseline restoration circuits will be removed to ensure a lower noise.

4.5 Conclusions

The full size detector operated with the fast $Ar/CO_2/CF_4$ (45/14/40) gas mixtur, demonstrate to be suitable to operate in the harsh environment around the beam pipe and largely fulfills the requirements of the region M1R1 of the LHCb experiment.
The full size detector, constituted by two coupled 20×24 cm^2 triple-GEM detectors, have been extensively and successfully tested at the T11-PS CERN facility, confirming the results obtained in the R&D phase with the small prototypes.
The large irradiation test, performed with a high intensity 1.25 MeV γ from a ^{60}Co source, indicate that the detector is robust and can tolerate the radiation dose foreseen in 10 years of operation in the region M1R1 of the LHCb experiment. Even after a severe irradiation in very bad conditions, the triple-GEM detector exhibit good time and efficiency (in 20 ns) performances.
In the last period we finalized the design of the detector and its construction tools, as well as the chamber quality checks.
A novel GEM foil assembly technique based on the stretching of the GEM foil itself, with the advantage to eliminate dead zone in the detector active area, has been successfully developed by our group.
The detector construction does not show any critical points and the construction of the 24 triple-GEM detectors has been started in the two INFN production sites of Cagliari and Laboratori Nazionali di Frascati.

Chapter 5

Study of luminosity measurements at LHCb

5.1 Introduction

The LHCb experiment will have a great potential to make various precision measurements in the B physics sector and to discover New Physics. It is designed to provide high statistics B related data sample, and the accuracy of the precision measurements will be also limited by systematic effects, such as uncertainty in the measurement of the luminosity.
In general, luminosity measurement and monitoring are needed for several purposes with somewhat different requirements. For physics analysis, one requires as precise as possible a measurement of the integrated luminosity, needed to compute a cross section from an observed number of events. Even for those physics analysis that do not require an istantaneous luminosity measurement, a luminosity monitoring would be useful as well for the tuning of the beam parameters.

In this chapter, two different physical channels will investigated in order to perform a luminosity measurement at LHCb: the dimuon coming from $Z^0 \rightarrow \mu^+\mu^-$ decay and the single muon coming indifferently from the W or Z^0 decay. For the next, I will refer to these measurements as *dimuon* and *single muon luminometers*, respectively.
Despite the limited angular acceptance of the LHCb spectrometer, these simulation studies will show that a luminosity measurement can be achieved with high statistical accuracy.

In the next section the several possible methods adopted to measure the luminosity at hadron colliders will be described. The hadronic production of W and Z^0 bosons at LHC energy will be discussed in Sec. 5.3, while the various simulation tools used to generate and analyse the Monte Carlo samples within the LHCb software will be considered in Sec. 5.4. Finally, the analysis and the results of the *dimuon* and *single muon luminometers* will be discussed in Sec. 5.5.

5.2 Luminosity measurements at LHC

In general, three types of luminosity measurements can be distinguished.

In the first measurement, the luminosity is completely determined by the properties of colliding beams [1]:

$$\mathcal{L} = F \frac{f \sum_i N_1^i N_2^i}{4\pi \sigma_x^* \sigma_y^*} \tag{5.1}$$

At LHC, f = 11 kHz is the beam-revolution frequency, F = 0.9 is a factor which accounts for non-zero crossing angle ($\sim$ 300 μrad), N_1^i and N_2^i are the numbers of protons in the colliding bunches ($\sim 10^{11}$) and σ_x^* and σ_y^* are the transverse bunch widths ($\sim$ 16 μm and assumed to be the same for all bunches) at the interaction point (IP).

The second method is based on the measurement of the proton-proton total and differential forward elastic cross sections which are related by the optical theorem. This method requires dedicated detectors placed as close as possible to the beam and is performed at LHC by the TOTEM experiment [74].

In the third approach the rate for a process, S, with a well known and sizable cross section, σ, is accurately measured and the luminosity $\mathcal{L}$ is extracted from:

$$S = \mathcal{L} \times \sigma \times B.R. \tag{5.2}$$

where B.R. is the branching ratio related to the specific process. In this case the precision is related to the theoretical error on the cross-section.
This method is widely used at e^+e^- colliders by exploiting the very clean Bhabha scattering, which allows to reach a high precision. At hadron colliders generally the high background makes rather difficult this kind of measurements. Moreover, the production cross section has

usually larger uncertainty. Nevertheless few processes can be still profitably used.
One example is the exclusive lepton-pair production via photon-photon fusion:

$$p\,p \rightarrow p\,p\,l^+\,l^-$$

where l = e or μ.
Luminometers based on such process have been proposed in [75], [76]. The cross section can be calculated at the LHC energy within pure QED with a theoretical uncertainty below 1%. On the other hand, the estimated production cross-section including branching ratio is low, of the order of 1 pb [77]. Assuming an average luminosity 2×10^{32} cm^{-2}s^{-1}, and considering 1y = 10^7 s, an integrated luminosity of 2 fb^{-1} is obtained at LHCb. This means 2000 events collected per year using the Eq. 5.2. In order to assure a statistical uncertainty below the theoretical limit, a collection of $\sim$ 10000 events is needed. This means that a luminosity measurement can not be achieved at LHCb with the required frequency, while it will be used in the higher luminosity experiments, such as ATLAS and CMS.

Other interesting processes that can be used in the luminosity measurements are the leptonic decays of the W and Z^0 bosons. The production cross sections, extrapolated at LHC energy, are rather large and have been recently calculated with a theoretical uncertainty below 4% [77].
In the next sections, their use as suitable luminometers at LHCb will be extensively studied.

5.3 Hadronic production of massive bosons

In the framework of the parton model the Z^0 and $W^{\pm}$ bosons are produced as resonances in the processes $pp \to \mu^+\mu^- X$ and $pp \to \mu^{\pm}\nu X$ respectively, as schematized in Fig. 5.1.

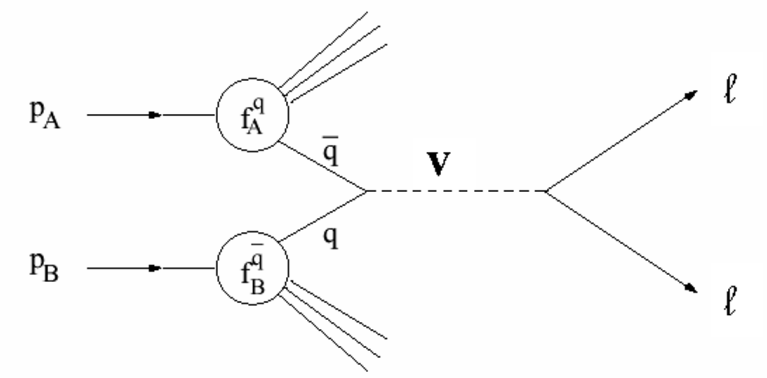

Figure 5.1: The basic $q\overline{q} \to V \to ll$ parton model interaction. I denote with V the Z or W boson, while with l the μ or the ν.

If p_A and p_B are the two incoming beam protons in their center of mass frame, each with energy E_{beam}, the total squared center of mass energy is then s = $4E^2_{beam}$. The two $q\overline{q}$ (as well as qg) that enter the hard interaction carry fractions x_1 and x_2 of the total beam momentum, i.e. they have four-momenta

$$p_1 = E_{beam}(x_1; 0, 0, x_1) \qquad p_2 = E_{beam}(x_2; 0, 0, -x_2)$$

The squared invariant mass of the two partons is defined as

$$\widehat{s} = (p_1 + p_2)^2 = x_1 x_2 s$$

with $\widehat{s} = M_V^2$ (M_V is the boson mass).
The QCD tree level diagrams for the point-like parton process are drawn in Fig. 5.2. The most probable process is the quark-antiquark annihilation ($q\overline{q} \to V$), which may be combined with a gluon ($q\overline{q} \to Vg$) or a photon ($q\overline{q} \to V\gamma$) radiation. Note that differently from the proton-antiproton machines, at LHC antiquarks must come from the sea, because only protons are colliding.

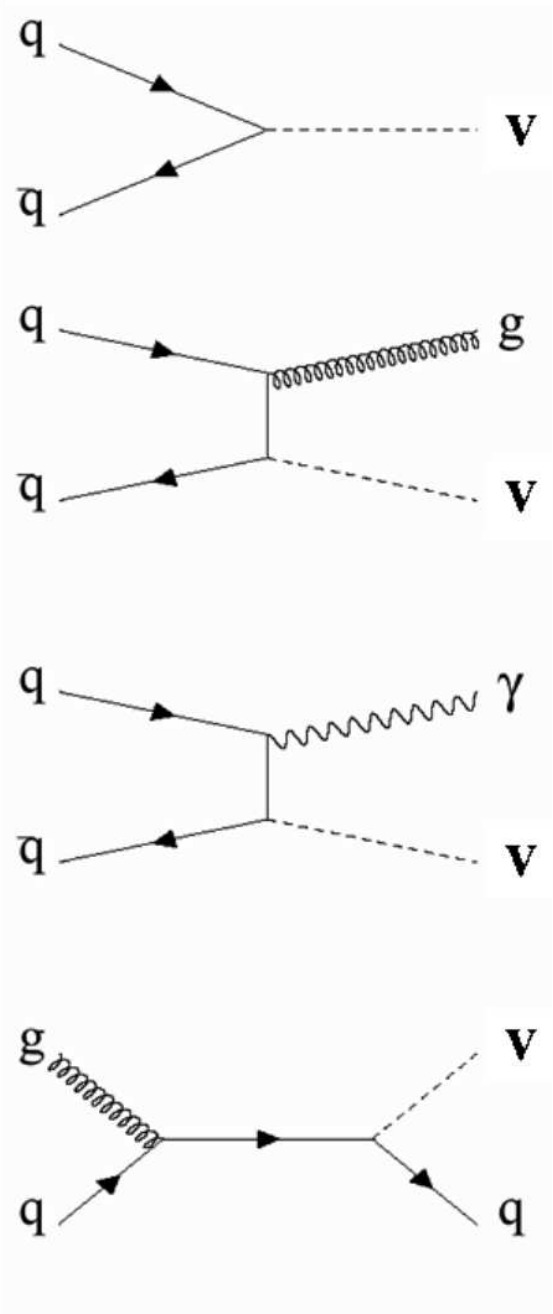

Figure 5.2: Tree level diagrams for the boson V production in a proton-proton collision. From top to bottom there are the quark-antiquark annihilation, the same process with a gluon or photon radiation, and the quark-gluon Compton scattering.

The other possible process is the Compton scattering between a quark and a gluon ($qg \rightarrow qV$). An example of a possible one loop correction diagram is also sketched in Fig. 5.3.

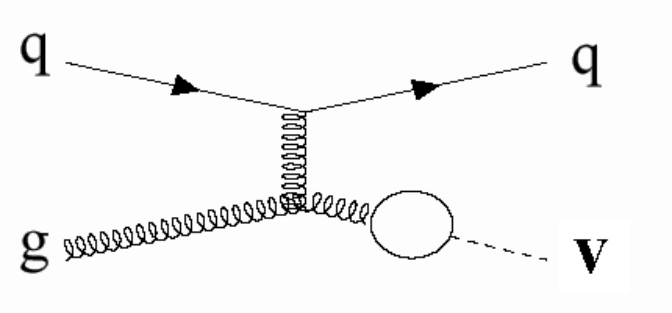

Figure 5.3: One loop correction to the quark-gluon scattering diagram.

Instead of x_1 and x_2 it is often customary to use the related variables τ and y:

$$\tau = x_1 x_2 = \frac{\widehat{s}}{s} \qquad y = \frac{1}{2} ln \frac{x_1}{x_2}$$

In case of W and Z^0, the first relation thus fixes the product of x_1 x_2 at LHC ($\sqrt{s}$ = 14 TeV) to $\tau_W = 3\times10^{-5}$ and $\tau_{Z^0} = 5\times10^{-5}$, respectively. It is effortless to demonstrate that the variable y is the rapidity of the massive boson V, so that the single fractional momenta of the quark and antiquark are directly related to the rapidity distribution of the boson:

$$x_1 = \sqrt{\frac{M_V^2}{s}} e^{y} \qquad x_2 = \sqrt{\frac{M_V^2}{s}} e^{-y}$$

For momenta much larger than this mass (p $\gg M_V$), y can be safely approximated by the pseudorapidity:

$$y \approx \eta = -\ln \tan(\theta/2)$$

5.3.1 Cross Section

The cross section for the $Z^0 \rightarrow \mu+\mu-$ process at the first order of approximation for the $q\overline{q}$ fusion is [78]:

$$\frac{d\sigma}{dm^2}(p_A p_B \rightarrow \mu+\mu-X) = (\frac{4\pi\alpha^2}{3m^2})\frac{1}{3}\sum_q e_q^2 \int_0^1 dx_1 \int_0^1 dx_2 \\ [f_A^q(x_1)f_B^{\overline{q}}(x_2) + f_A^{\overline{q}}(x_1)f_B^q(x_2)]\delta(m^2 - \widehat{s})$$

The first factor in brackets is the high energy QED cross section for $e^+e^- \rightarrow ll$, since the $q\overline{q} \rightarrow ll$ is the same apart from the quark charge. The extra factor 1/3 accounts for the fact that the three colors of q and $\overline{q}$ occur with equal probability, but only a q and $\overline{q}$ of the same color can annihilate to form a colorless boson. The $f^q(x)$ are the quark structure functions, which must be known at different values of fractional momenta x, in order to evaluate the integral.

The production cross sections of W and Z^0 bosons have been measured at the Tevatron collider, the proton-antiproton machine with $\sqrt{s}$ = 1.96 TeV.
In Fig. 5.4 the results for the cross-sections times branching ratios are shown for the various decay channels of the W and Z^0 measured by CDF and D0 experiments [79].
The results for $\sigma_W \times BR(W \rightarrow \mu\nu)$ and $\sigma_Z \times BR(Z \rightarrow \mu\mu)$ at Tevatron center of mass energy are $\sim$ 2800 pb and $\sim$ 250 pb, respectively. These measurements are consistent with the Next-to-Next-Leading-Order (NNLO) theoretical calculation as shown in Fig. 5.5.

At LHC energy, the production cross sections of W and Z^0 must be extrapolated and are foreseen to be almost an order of magnitude larger than that found at Tevatron energy (Fig. 5.6). Recently a NNLO estimation of the cross sections of these bosons have been done at $\sqrt{s}$ = 14 TeV as can be seen in Fig. 5.7, where the successive approximations are pointed out starting to Leading-Order (LO) [77].

The result of these studies is an error band, accounting for uncertainties in some deep inelastic functions and in $\alpha_S(M_Z^2)$, of about 1%. However the uncertainties in the input of the parton density functions (PDF) mean that the error could, conservatively, be large as $\pm$4% (Fig. 5.8). As a comparison at the Tevatron energy the theoretical uncertainty is $\pm$ 3%.

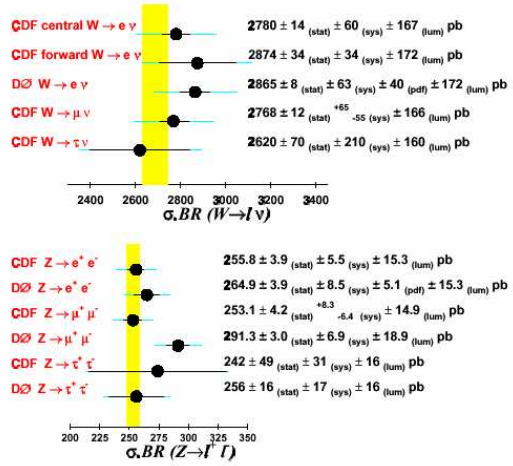

Figure 5.4: Measured cross sections time branching ratios for $p\overline{p} \rightarrow W$ and $p\overline{p} \rightarrow Z$ production at the Tevatron [79].

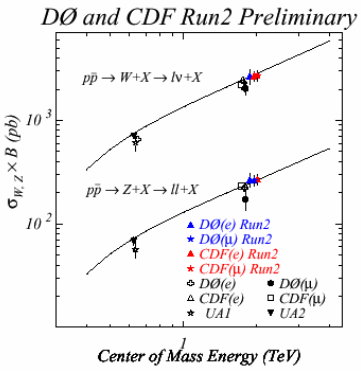

Figure 5.5: $W \rightarrow l\nu$ and $Z^0 \rightarrow ll$ cross sections measured by CDF and D0 at $\sqrt{s}$ = 1.96 TeV and UA1 and UA2 at $\sqrt{s}$ = 650 GeV [80]. The data match with the theoretical NNLO calculations represented by solid lines.

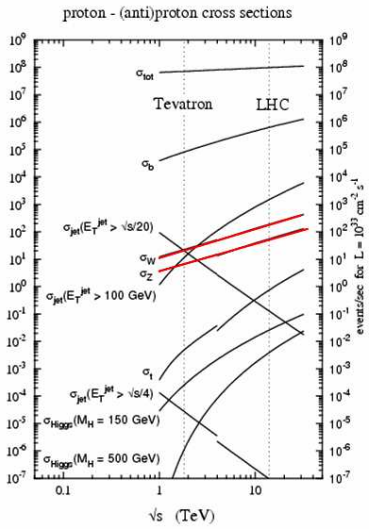

Figure 5.6: Total proton-(anti)proton cross sections as a function of $\sqrt{s}$. In particular, the trend of the production cross section of W and Z bosons are pointed out by the red lines. At $\sqrt{s}$ = 14 TeV the foreseen cross sections are: σ_Z = 55.5 nb and σ_W = 187 nb.

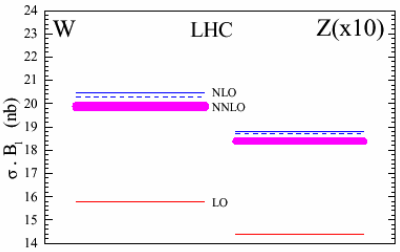

Figure 5.7: The predictions of the cross sections for W and Z^0 production including the leptonic decay branching ratios at LHC obtained from global analysis of the data set MRST00 [81] [82]. The band of the NNLO prediction takes into account the ambiguity in the corresponding splitting functions [83].

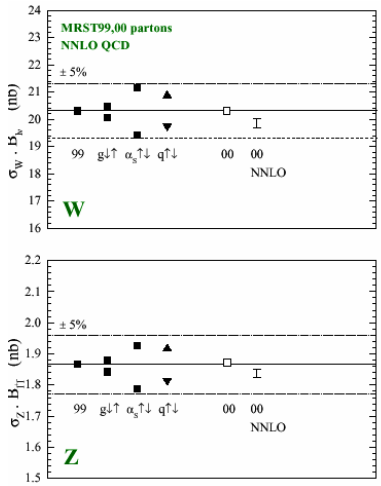

Figure 5.8: The solid squares and the triangles represent the prediction of the NNLO cross sections for Z and W production including the leptonic decay branching ratios at $\sqrt{s}$ =14 TeV obtained using various set of partons distribution functions [81] [82].

The detailed study of the uncertainty on the PDF set and the consequent theoretical accuracy on the Z^0 and W production cross sections are outside the aim of this thesis. Anyway, the theoretical cross section values, together with their uncertainty, will be used to compute the luminosity measurements within the LHCb experiment.

The evaluated NNLO production cross sections times lepton decay branching ratios for both weak bosons in 4π are:

- $\sigma_Z \times BR(Z \rightarrow \mu\mu)$= 1.86 $\pm$ 0.07 nb
- $\sigma_W \times BR(W \rightarrow \mu\nu)$= 20.27 $\pm$ 0.05 nb

Once the cross sections are known, the event rate for the two different physical channels can be computed:

$$S_{Z\rightarrow\mu\mu} = \mathcal{L} \times \sigma_Z \times BR_{Z\rightarrow\mu\mu} \times \varepsilon^{\mu\mu}_{tot} \quad ; \quad S_{1\mu} = \mathcal{L} \times (\sigma \times BR)_{1\mu} \times \varepsilon^{1\mu}_{tot} \tag{5.3}$$

where:

- $S_{Z\rightarrow\mu\mu}$ and $S_{1\mu}$ are respectively the events yield of Z^0 decaying in two muons and the single muon coming indifferently from Z^0 or W;
- $\sigma_Z \times BR_{Z\rightarrow\mu\mu} \simeq$2 nb and $(\sigma \times BR)_{1\mu} \simeq$ 22 nb. The latter is the sum of the production cross sections and muon decay branching ratios of the Z^0 and W processes;

- $\varepsilon_{tot}^{\mu\mu}$ and $\varepsilon_{tot}^{1\mu}$ are the total signal efficiencies on the dimuon and the single muon, respectively;

Since the Z^0 and W production cross sections are known with a theoretical uncertainty of 4%, the *single muon luminometer* is characterized by a larger theoretical error of about 6%, coming from the squared sum of the theoretical uncertainties of Z^0 and W production cross sections, with respect to the 4% of the *dimuon luminometer*.
To compare the performances of the two approaches, a statistical uncertainty below 4% will be consider. This means that $\sim$ 700 events must be collected.

5.4 Simulation framework

The LHCb software follows an architecture-centric approach based on Gaudi [84], which is a general Object Oriented framework. Typical phases of particle physics data processing have been encapsulated in four C++ based applications, which execute the following tasks:

1. generation of the event and tracking of particles through the detector (Gauss);
2. simulation of the detector response (Boole);
3. reconstruction of the event, including track finding and particle identification (Brunel);
4. trigger and offline selection of a specific process (DaVinci).

Each application is producer and/or consumer of data for the other stages, communicating via the LHCb Event model and making use of the LHCb unique detector description, as shown in Fig. 5.9. External programs such as Pythia [85] and Geant [86] may be used by the applications to perform specific purposes.

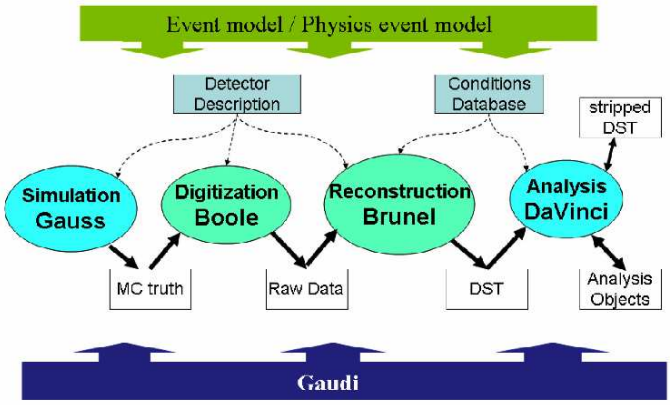

Figure 5.9: The LHCb data processing applications and data flow. Underlying all of the applications is the Gaudi framework and the event model describes the data expected. The arrows represent input/output data.

In the last two steps (Brunel and DaVinci), the simulated events are processed as if they were from real data, i.e. without using any information from the so-called Monte Carlo truth. This information can only be used to assess the performances of the different reconstruction and selection algorithms. Fig. 5.10 shows the various stored informations during the processing of an event, from the generation to the analysis phases.

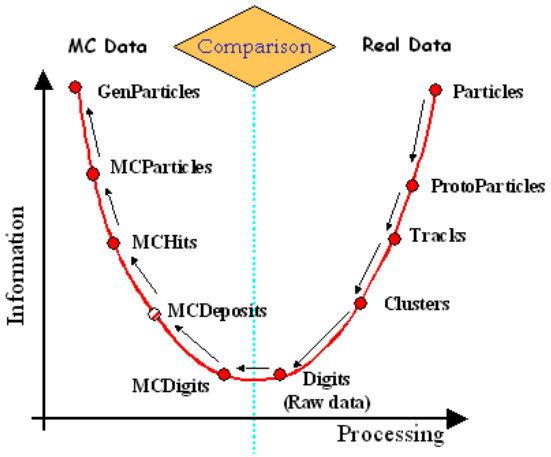

Figure 5.10: Sketch of the stored information during the processing of a event.

5.4.1 Event generation

The generation of the event is performed by the C++ program Gauss. It simulates the behavior of the spectrometer allowing to understand the experimental conditions and performances. It integrates two independent phases, *Generation* and *Simulation*, that can be run together or separately.
The first phase, provided by Pythia (the standard event generator in high energy physics), consists of the event generation of proton-proton collisions at $\sqrt{s}$ = 14 TeV.
In order to generate my MC samples, I have requested to Pythia to generate Z^0 or W bosons from the parton-parton interaction according to PDF CTEQ 5L [87]. Note that being interested only in real Z^0 bosons, the Z^0/γ^* interference structure has not been considered, just including the Z^0 matrix elements, so that only "on mass-shell" Z^0 are generated. All the tree level processes described in the previous section (Fig. 5.2) are included in the simulation.
To save CPU time and increase the event generation efficiency, the Z^0 or W bosons are forced to decay only in $\mu^+ \mu^-$ or $\mu^\pm \nu$.
Then the decay muons are required to have a polar angle less than 400 mrad, representing the limiting angle a track must have to leave hits in the last three VELO stations (see Sec. 1.2.1). Fig. 5.11 shows the Pythia setting for the Z^0 and W production together with the angular request.

This generator phase also handles the simulation of the running conditions such as the

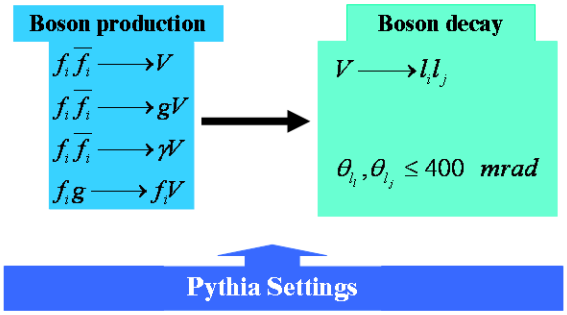

Figure 5.11: The Pythia settings for the production of the Z^0 or W bosons, and the relative decay constraints.

smearing of the interaction region due to the transverse and longitudinal size of the proton bunches and the changes of luminosity during a fill due to the finite beam lifetime.

The second phase of Gauss consists in the tracking in the LHCb detector of the particles produced by the generator phase. The simulation of the physics processes, which the particles undergo when travelling through the apparatus materials, is delegated to the Geant4 tool [86]. The detector geometry and materials are described in detail, including the active detection components and their front-end electronics, passive materials such as the beam-pipe, frames, supports and shielding elements. In this phase, all the hits of each particle traversing a sensitive detection layer are registered, together with its energy loss in that layer and its time-of-flight with respect to the primary interaction time. Low-energy particles, mainly produced in secondary interactions, are also traced, down to an energy cut-off of 10 MeV for hadrons and 1 MeV for electrons and photons.
After these two phases, Gauss produces a file that contains software classes called *MCParticles*, *MCVertices*, *MCHits* and *MCDeposits* (see Fig. 5.10).

5.4.2 Event digitization

The digitization of the event is performed by the C++ program Boole and represents the final stage of the LHCb simulation.
In this phase, the informations coming from Gauss are used to generate digitized hits, taking into account the details of the sensitivity and the response of each sub-detector, where detection efficiency, space and time resolution are adapted to the results from beam tests of

prototypes. In addition, the read-out electronics performances, such as noise, cross-talk effects and dead channels, as well as the L0 trigger hardware have been considered.
The Boole output has the same format as the real data coming from the detector during the data taking.

5.4.3 Event reconstruction

The reconstruction of the event is performed by C++ programm Brunel and is divided in two different steps:

1. track reconstruction;
2. particle identification;

In the track reconstruction phase, the registered hits of the VELO, the TT and T1-T3 detectors are combined to form particle trajectories from the VELO to the calorimeters. The program aims to find all tracks in the event which leave sufficient detector hits. After fitting the reconstructed trajectory a track is represented by state vectors (x, y, dx/dz, dy/dz, Q/p) which are specified at given z-positions in the experiment.
Depending on the generated trajectories inside the spectrometer the following classes of tracks are defined, illustrated in Fig. 5.12:

1. **Long tracks:** traverse the full tracking set-up from the VELO to the T1-T3 stations. They are the most important set of tracks for B-decay reconstruction.
2. **Upstream tracks:** traverse only the VELO and TT stations. They are in general lower momentum tracks that do not traverse the magnet. However, they pass through the RICH 1 detector and may generate Cherenkov photons. They are therefore used to understand backgrounds in the particle-identification algorithm of the RICH.
3. **Downstream tracks:** traverse only the TT and T1-T3 stations. The most relevant cases are the decay products of K^0_S and Λ that decay outside the VELO acceptance.
4. **VELO tracks:** are measured only in the VELO and are typically large angle or backward tracks, useful for the primary vertex reconstruction.
5. **T tracks:** are only measured in the T1-T3 stations. They are typically produced in secondary interactions, but are useful for the global pattern recognition in RICH 2.

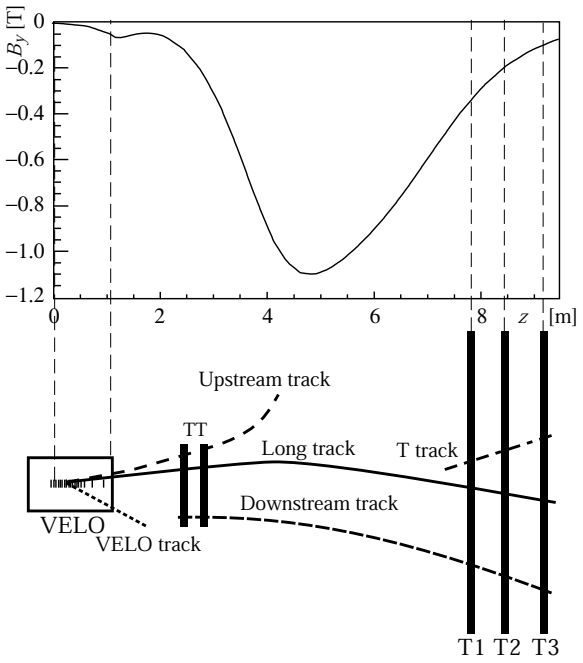

Figure 5.12: A schematic illustration of the various track types: long, upstream, downstream, VELO and T tracks. For reference the main B-field component (B_y) is plotted above as a function of the z coordinate.

As will be shown in the following, most of the muons decaying from Z^0 and W in the spectrometer acceptance are reconstructed as **Long tracks**.

The particle identification is provided by the two RICH detectors, the Calorimeter system and the Muon Detector. For the common charged particle types $(\mathrm{e}, \mu, \pi, \mathrm{K}, \mathrm{p})$, electrons are primarily identified using the electromagnetic calorimeter, muons with the muon detector, and the hadrons with the hadronic calorimeter and the RICH system, which provides a good separation between π, K ,p. However, the RICH detectors can also improve the lepton identification, so the informations from the various detectors are combined.
In general for decay muons, the most relevant source of misidentification is represented by the charged pions that succeed in traversing the muon filter, commonly called *punch-through*. To reject this background, a muon identification is performed cutting on the ratio of the likelihoods between the muon and pion hypotheses:

$$\begin{aligned} \Delta \ln \mathcal{L}_{\mu\pi} &= \ln \mathcal{L}(\mu) - \ln \mathcal{L}(\pi) \\ &= \ln \left[\mathcal{L}(\mu)/\mathcal{L}(\pi)\right] \end{aligned}$$

where the likelihoods from the various sub-detector are simply combined as follows:

$$\mathcal{L}(\mu) \;=\; \mathcal{L}^{\mathrm{RICH}}(\mu)\,\mathcal{L}^{\mathrm{CALO}}(\mathrm{non\,e})\,\mathcal{L}^{\mathrm{MUON}}(\mu)$$

In general, a $\Delta \ln \mathcal{L}_{\mu\pi} > -8$ allows to reduce the pion misidentification to 1%, whilst maintaining an efficiency of 93% for muons coming from B decay [4]. In the case of Z^0 and W processes, the decay muons have a transverse momentum much higher than that of *punch-through* particles, giving a misidentification practically negligible.

5.4.4 Analysis and Trigger

Finally the events are analyzed with the C++ program DaVinci, in order to select the interesting physics and reduce the background.
Unlike what is going to happen during real data taking, the trigger filter is also applied in DaVinci.
The L0, L1 and HLT algorithms however, just flag the triggered events, providing the complete on-line and off-line selections for any kind of study.

The general description of the three-level triggers at LHCb experiment are presented in the first chapter of this thesis.
I recall here that the L0 trigger is a hardware filter, where suitable cuts on the various physics parameters are performed and already fixed by a dedicated electronics called Off Detector Electronics. Its response is simulated in the Boole phase and no changes can be performed in the analysis. On the contrary, the L1 and HLT trigger are software filters and their algorithms can be developed before and during the data taking. Therefore, in the following sections the L1 and HLT triggers will be discussed in detail in order to show the present status.

L1 trigger

The L1 trigger will run at 1 MHz after the L0 trigger and will have an output rate of 40 kHz. It performs a decision looking for tracks in the VELO detector coming from a secondary vertex. At this level, the tracks are reconstructed in two dimensions ($r - z$). Those 2D tracks are then matched to the hits founded in the TT station and the Level-0 candidate, which can

be a muon, an electron or a hadron that has triggered at L0 filter. Only after the L1 decision, i.e. at the HLT level trigger, the tracks in the VELO are reconstructed in three dimensions.
The L1 decision algorithm [14] consists of two parts: in the first, called generic algorithm, a trigger variable is computed based on the properties of the two track with highest p_T and a suitable impact parameter (IP). This part is therefore sensitive to a very generic b-hadron signature.
In the second part, called specific algorithm, the trigger variable is weighted according to signatures involving L0 candidates, such as dimuons or high E_T electrons and photons, that are present in the event. This means that a good L0 signature have the effect of relaxing the generic requirements.
In Tab. 5.1 are summarized the suitable cuts adopted in the generic and specific algorithms and the relative bandwidths.

Algorithm		kinematical cat	geometrical cut	Bandwidth (kHz)
Generic		$\ln(p_{T_1})+\ln(p_{T_2}) > 13.55$	IPs > 0.15	30
Specific	Single muon	$p_T > 1.95$ GeV	$IP_\mu > 0.15$	8.8
	Dimuon general	$m_{\mu\mu} > 500$ MeV	$IP_{\mu\mu} > 0.15$	1.7
	Dimuon J/ψ	$m_{\mu\mu} > 2.6$ GeV	No $IP_{\mu\mu}$ cut	1.8
	Electron	$E_T > 3.45$ GeV		3.9
	Photon	$E_T > 3.15$ GeV		4.0

Table 5.1: Summary of the L1 performances. If not indicated the p_T are referred in MeV. The overlapping of the algorithm bandwidths is not taking into account.

It should be noted that all the algorithms, except the dimuon J/ψ specific algorithm, are optimized for the B-physics due to the high impact parameter requirement.
On the other hand, the dimuon J/ψ specific algorithm seems to be useful also for the $Z^0 \rightarrow \mu^+\mu^-$ process, while no algorithm presently exists for the single muon coming from the Z^0 or W.
Due to the low 2D track capability in the VELO and the high polar angles correlation of those muons, about 50% of $Z^0 \rightarrow \mu^+\mu^-$ decays do not pass the L1 trigger, as shown in a previous work presented at CERN [88]. This result is in agreement with that obtained with the $B_s^0 \rightarrow J/\psi(\mu^+\mu^-)\Phi$ [89]. In this case, the total efficiency of the L1 trigger reaches about 87% because the single muon specific algorithm, which looks for muons with high impact

parameter, helps to increase the L1 trigger efficiency.
In agreement with the LHCb trigger group, I developed within the L1 trigger a new specific algorithm which looks for single muons with a high transverse momentum, $p_T > 10$ GeV, requiring an impact parameter less than 0.15 mm. These cuts have been chosen in order to selects muons coming directly from the $p - p$ interaction region.
For the next I will refer to this new algorithm as *low IP muon*.
The aim of such a development is to achieve a good L1 efficiency on the $Z^0 \rightarrow \mu^+\mu^-$ decay and to add a new dedicated algorithm for the single muon coming from the Z^0 and W. Clearly, the addition of this algorithm requires a limited bandwidth in order to not upset the L1 streaming. In particular, the determination of the needed bandwidth for such an algorithm has been performed with the *single muon luminometer* analysis, which shows at most a bandwidth of about 50 Hz. This value is obviously negligible with respect to the bandwidth dedicated to the single muon specific algorithm ($\sim$ 9 kHz) thus the new algorithm could be easily included within the L1 trigger.

HLT trigger

The HLT trigger will run at 40 kHz after L1 trigger and will have an output rate of 2 kHz divided in four main streams:

- Exclusive B ($\sim$ 200 Hz): the core physics stream with exclusively reconstructed decays;
- D^* ($\sim$ 300 Hz): these events allow to measure the particle identification efficiency and mis-identification fraction and can also be used for CP measurements in D decays;
- Dimuon ($\sim$ 600 Hz): dimuons with a mass above 2.5 GeV. These events are used to measure the uncertainty on lifetime measurements.
- Inclusive B ($\sim$ 900 Hz): events with one high p_T and high impact parameter muon, used for systematic studies of the trigger efficiency.

The data flow of the HLT trigger with the various specific algorithms is sketched in Fig. 5.13.

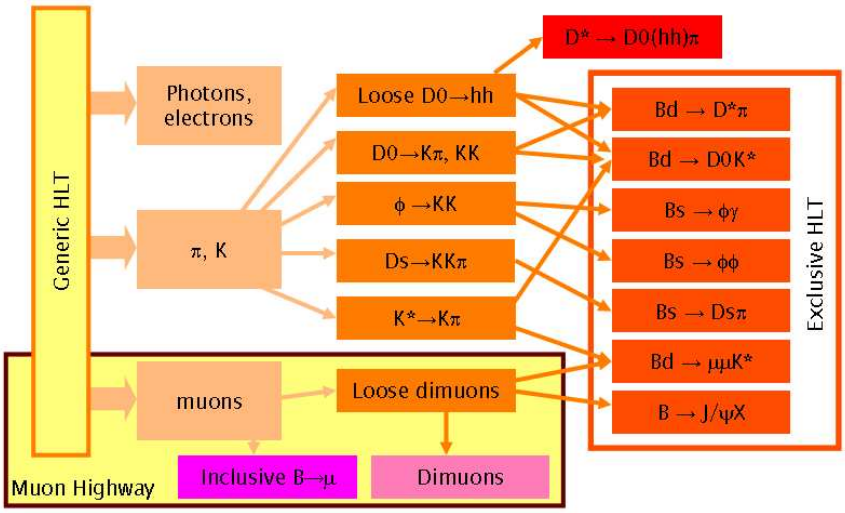

Figure 5.13: Simplified data flow in the HLT trigger. Each box is an algorithms (or a set of algorithms).

Presently, only the so called dimuon algorithm is designed to filter the $Z^0 \rightarrow \mu^+\mu^-$ events, while no dedicated algorithm is foreseen for the single muon decaying from Z^0 and W bosons. The addition of a new algorithm for such a process will be performed in future. Anyway, in order to compare the total efficiencies of the two luminosity measurements, the HLT efficiency of the *single muon luminometer* will be kept equal to that obtained with the *dimuon luminometer*.

5.5 Selection algorithms

In this section, the common features of the *dimuon* and *single muon luminometer* methods are shown, while the specific selection and the background on the signal will be discussed in Sec. 5.5.1 and Sec. 5.5.2, respectively.
To study the different *dimuon* and *single muon* processes, $\sim$ 25000 events of $pp \rightarrow Z^0 \rightarrow \mu^+\mu^-$ and $\sim$ 50000 events of $pp \rightarrow W^{\pm} \rightarrow \mu^{\pm}\nu$ has been generated in the LHCb angular acceptance.
The first number represents the sample of the *dimuon luminometer*, while the sample of the *single muon luminometer* is composed by 50000 events of W and 5000 events of Z^0 according to the ratio between their production cross sections times branching ratios. Note that in the latter study, the 5000 events has been extracted by the whole $Z^0 \rightarrow \mu^+\mu^-$ requiring only a reconstructed muon. In this way, the two luminometer studies are completely uncorrelated and their performances can be therefore compared.

Fig. 5.14 schematizes a generic leptonic decay from an electroweak boson, together with some properties of the reconstructed track used in the selection algorithms. Every track has its own impact parameter (IP) with respect to the primary vertex, i.e. the interaction point.
In the case of a Z^0 or W production, the interaction point should be the only vertex in the event, as it coincides with the secondary vertex, i.e. the common lepton decay vertex. To identify muons originating from the interaction point from those arising from long-lived particles (e.g. from semileptonic decay of B meson) a small impact parameter is required.

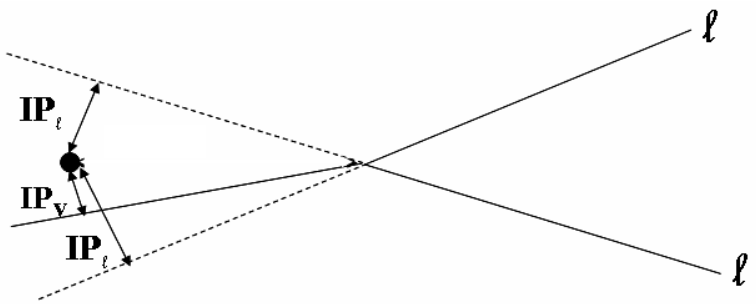

Figure 5.14: Schematic representation of a reconstructed V boson leptonic decay, where V generally denotes a Z or W. Some of the track parameters used for the selection are indicated.

The two selection algorithms start with the reconstruction of all primary vertices present in an event, determining the z coordinate of the primary collisions. Since at the nominal LHCb luminosity ($\mathcal{L}$=2$\times$10^{32} cm^{-2}s^{-1}) it is expected to have zero interactions in the 55% of the bunch crossings, a single interaction in the 35% and a multiple interaction in the other cases, almost all the simulated events have a single interaction. In case of multiple interaction, the analysis is also performed.
All tracks reconstructed in the VELO are used to identify the primary vertices in order to get the best resolution. The interaction region has a Gaussian distribution with σ_z = 5 cm around the nominal interaction point, while in the transverse plane the Gaussian distribution show σ_{x-y} of about 0.1 mm (Fig. 5.15).

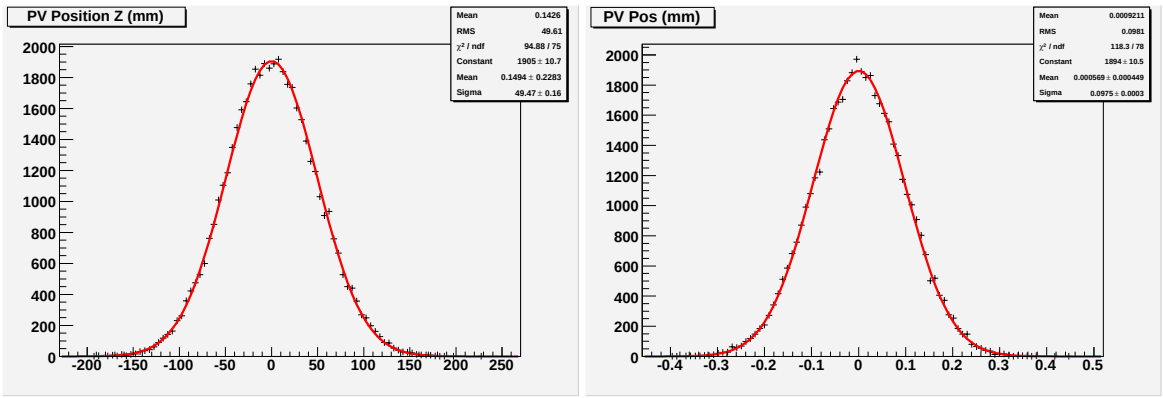

(a) Longitudinal plane.

(b) Transversal plane (r=$\sqrt{x^2+y^2}$).

Figure 5.15: Gaussian fit of the interaction point.

After the reconstruction of primary vertices, the two algorithms apply different cuts in order to optimize the ratio between the signal and the background.

5.5.1 Dimuon luminometer

In the *dimuon luminometer*, the signal is represented by a couple of muons with opposite charge and high transverse momenta. These and the large invariant mass of the Z^0 provide a clear selection strategy and ensures a good efficiency in the rejection of the combinatorial background.
Fig. 5.16 shows the selection cuts which allow to isolate the $Z^0 \to \mu^+\mu^-$ signal with respect to the background sources, summarized in Tab. 5.2.

Process	$\sigma \times BR$ (pb)
$Z^0 \to \tau^+\tau^- \to \mu^+\nu_\mu\overline{\nu}_\tau\mu^-\overline{\nu}_\mu\nu_\tau$	2
$t\bar{t} \to W^+bW^-b \to \mu^+\nu_\mu + \mu^-\overline{\nu}_\mu + X$	8
Minimum Bias events	80×10^9
$b\bar{b}$ inclusive	500×10^6

Table 5.2: Cross section for the most important background processes to the signal. The cross section times branching ratio should be compared with the 1.86 nb of the $Z^0 \to \mu^+\mu^-$ process. For the $b\bar{b}$ inclusive and the minimum bias events the leptonic branching ratio are not included. The production cross section of the $t\bar{t}$ process has been evaluated at NNLO [90].

To discriminate the signal from the background contributes, the following selection cuts are applied:

- a muon identification $\Delta \ln \mathcal{L}_{\mu\pi} >$ -8;
- a muon transverse momentum, $p_T^\mu > 10$ GeV/c;
- a muon impact parameter significance with respect to the primary vertex, $IP_\mu/\sigma_{IP} <5$;
- a vertex fit of the opposite charged muons with a $\chi^2 < 5$;
- a dimuon invariant mass of $\pm$ 30 GeV/c^2 around the nominal Z^0 mass.

An event surviving these cuts is tagged as aZ^0 candidate and it is required to have:

- a impact parameter significance with respect to the primary vertex, $IP_Z/\sigma_{IP} <5$.

Note that for a Gaussian error the significance indicates the displacement of a certain quantity from zero in units of standard deviation, and is therefore the most meaningful statistical variable. Requiring an impact parameter significance $IP/\sigma_{IP} < 5$ means that the impact

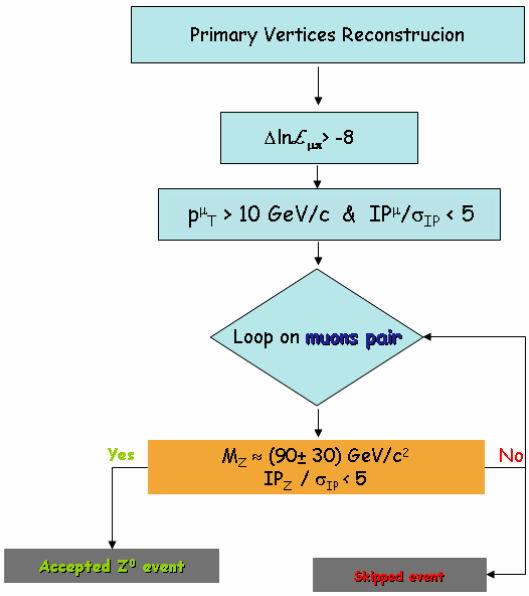

Figure 5.16: Sketch of the selection algorithm applied to the $Z^0 \rightarrow \mu^+\mu^-$ signal.

parameter must be compatible with zero within 5 standard deviations. This is no more true if the error is not Gaussian, which could happen in case of a bad reconstruction.

In this study only the minimum bias and $b\bar{b}$ inclusive events has been considered as a background because the $Z^0 \rightarrow \tau^+\tau^- \rightarrow \mu^+\nu_\mu\overline{\nu}_\tau\mu^-\overline{\nu}_\mu\nu_\tau$ and $t\bar{t} \rightarrow W^+bW^-b \rightarrow \mu^+\nu_\mu + \mu^-\overline{\nu}_\mu + X$ events have not been generated yet. Anyway their contribution can be estimated. Considering the sum of their cross sections times branching ratios, i.e 10 pb, a contribution to the signal could be at most of about 0.5% ($\Sigma_i\sigma_i \times B.R._i/\sigma_{Z^0} \times B.R.$) without considering the selection cuts.
The previous selection cuts are applied to 15×10^6 minimum bias and 8×10^6 $b\bar{b}$ inclusive events. The required low impact parameter significance and the high transverse momentum allow to reject about 99% of the minimum bias events and 70% of the $b\bar{b}$ inclusive before the muons combinatorial loop. The remaining is rejected by the large invariant mass cut and no event has been therefore selected as Z^0.

Events surviving the off-line selection are then passed through the L0, L1 and HLT trigger simulation algorithms. The complete off-line and on-line performance of the detector can be studied.

Analysis results

Single muon and Z^0 boson distributions are reported in the following figures for selected tracks.

Fig. 5.17 shows the momentum distribution of the decaying muons. It is interesting to note how the tail of the distribution reaches very high value, up to 2 TeV/c. This will result rather useful for calibration purposes.

The single muon transverse momentum spectrum is reported in Fig. 5.18. As expected, the transverse momentum spectrum shows a peak value at half the Z^0 boson mass. It should be noted the asymmetry of the distribution in particular stressed at $p_T < 45$ GeV/c. This asymmetry is reflected on the dimuon invariant mass and it is due to radiative effects in the final state of the Z^0 production and the momentum resolution of the LHCb apparatus. These effects will be discussed in the following when the dimuon invariant mass will be presented.

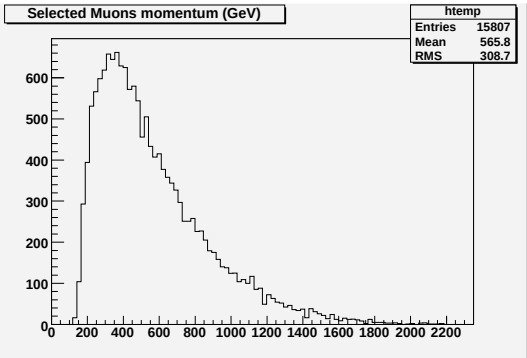

Figure 5.17: Momentum spectrum of the selected muons tracks.

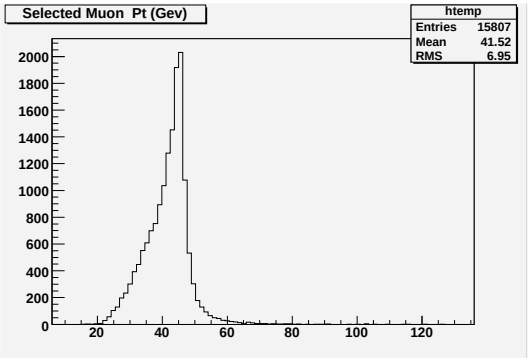

Figure 5.18: Transverse momentum spectrum of the selected muons tracks.

The muons impact parameter significance with respect to the primary vertex is shown in Fig. 19(a). As foreseen most of the muon tracks have an impact parameter within 2 standard deviations from zero. For comparison, a typical corresponding cut for $B^0 \to \pi^+\pi^-$ is between 5 and 10. Of course in that case the cut is on the lower values.

The impact parameter significance distribution of the Z^0 candidate (Fig. 19(b)) looks very similar to the single muon distribution, confirming that both particles are likely to be produced in the primary interaction vertex.

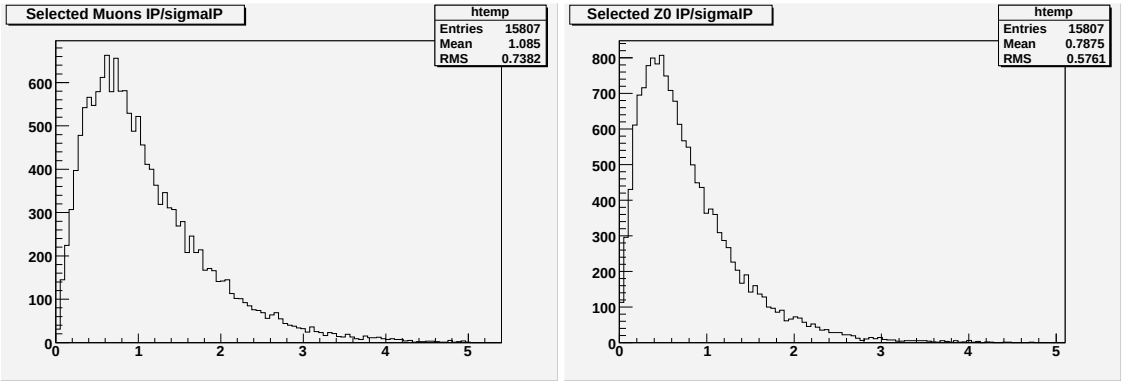

(a) Muons tracks.

(b) Z^0 boson.

Figure 5.19: Impact parameter significance with respect to the primary vertex.

Finally, the dimuon invariant mass is reported in Fig. 5.20. The spectrum has been fitted with the usual Breit-Weigner function

$$\sigma_{BW}(M) = N\frac{\Gamma_{tot}^2}{(M - M_R)^2 + \Gamma_{tot}^2/4}$$

and the fit results for the Z^0 mass and width are reported in Tab. 5.3 with the analogous PDG [91] published values. The mass of the Z^0 is determined with a relative error of $\Delta M/M \approx 2\times10^{-4}$ and it is perfectly compatible with the PDG value.

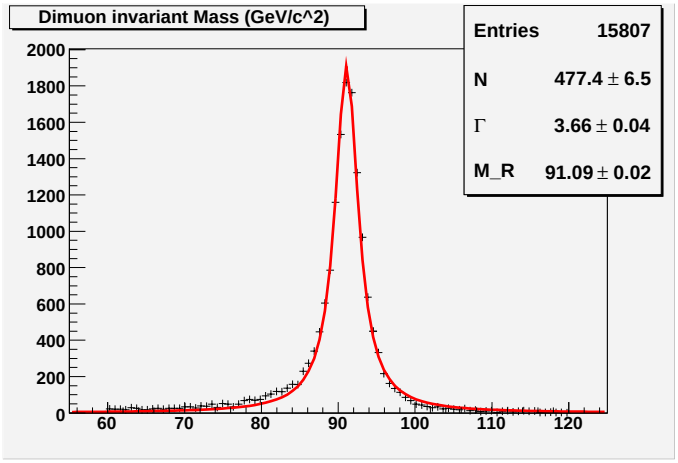

Figure 5.20: Invariant mass spectrum of the dimuon fitted with a Breit-Weigner function.

	Z^0 mass M_R (GeV/c^2)	Z^0 full width Γ_{tot} (GeV/c^2)
Fit	91.09 ± 0.02	3.66 ± 0.04
PDG	91.1876 ± 0.0021	2.4952 ± 0.0023

Table 5.3: Z^0 boson properties as fitted from dimuon invariant mass and as published on the PDG 2004.

The full width of the resonance results a $\sim$ 40% wider with respect to the PDG value. This broadening is due to the radiative effects introduced in the final state of Z^0 production, such as Z^0g, $Z^0\gamma$ and Z^0q which carry away part of the available momentum, and to the momentum resolution of LHCb spectrometer, not optimized to measure such high values. Moreover the relative error on the momentum measurement increases with the momentum itself, because higher momentum tracks are less bent by the magnet, and have smaller sagitta. For LHCb the relation is

$$\frac{\Delta p}{p} = 3.6 \times 10^{-5}\ (GeV/c)^{-1} \cdot p$$

which means for instance that a momentum of 600 GeV/c, corresponding to the mean value of Z^0 decaying muons distribution, is determined with a 2% error, and a momentum of 2 TeV/c with a 7% error.

Selection efficiency

The total signal efficiency, which appears in the Eq. 5.3, can now be calculated as the fraction of signal events that are reconstructed, selected with off-line selection cuts and triggered by L0, L1 and HLT triggers. It can be factorized as:

$$\varepsilon_{tot} = \varepsilon_{gen} \times \varepsilon_{rec} \times \varepsilon_{sel} \times \varepsilon_{trig} \tag{5.4}$$

where the different efficiencies for $Z^0 \to \mu^+\mu^-$ are discussed below and are summarized in Tab. 5.4.

	Number of event	Efficiency (%)
Generated in 4π	3780	
Found in 400 mrad	1090	28.8 ± 0.7
Generated in 400 mrad	25450	
Reconstruction	16541	65.0 ± 0.3
Selected	15807	95.6 ± 0.2
L0 passed	15180	96.0 ± 0.2
L1 passed	13249	87.3 ± 0.3
HLT passed	12639	95.4 ± 0.2
		Total Efficiency 14.3 $\pm$ 0.7

Table 5.4: Summary of signal efficiency for $Z^0 \to \mu^+\mu^-$. The number of processed events are reported as well. The error is statistical, while the error of the total efficiency is compute as squared sum in order to take into account the generation efficiency.

- generation efficiency (ε_{gen}). This is the efficiency to generate events with the required cut at 400 mrad with respect to those generated in the whole polar angle. To evaluate this generation efficiency, a small production of $\sim$ 4 thousand events of $Z^0 \to \mu^+\mu^-$ have been generated in the whole polar angle. Fig. 5.21 shows the theta distribution of the muons decaying from Z^0 with and without the cut at 400 mrad. The ratio between the two distributions gives a generation efficiency of 29%. Note that this ratio is much greater than the corresponding solid angle ratio $0.4/\pi$ = 13% because at the LHC energy the muons decaying from Z^0 are considerably forward boosted at lower polar angles, in spite of their large transverse momentum, as can be seen from Fig. 5.22, showing the theta distributions of the two decaying muons. It is also evident how the polar angles

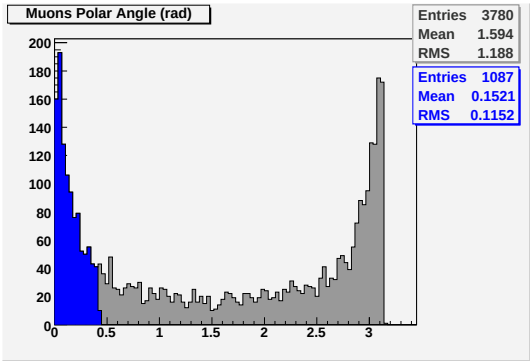

Figure 5.21: Polar distribution on muons decaying from Z^0 in the all solid angle (grey) and with the cut at 400 mrad (blu).

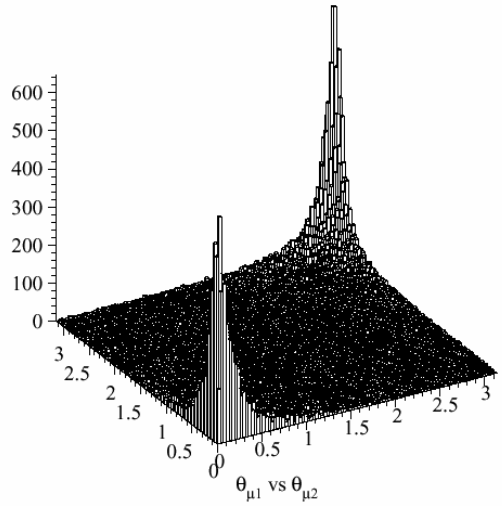

Figure 5.22: The polar angle of the two muons decaying from Z^0 boson in 4π.

of the two opposite charged muons are highly correlated.

- reconstruction efficiency(ε_{rec}). The events have been generated in a polar angle which is a little greater than the effective LHCb acceptance. This is done to study the track reconstruction capability of the apparatus, including any possible effects and the geometrical acceptance. This is evident by Fig. 5.23 where is shown the angles distribution of reconstructed muons. The white regions in the $\theta - \phi$ plane represents the areas which are not covered by the apparatus. Note that very low θ angles (< 16 mrad), are not covered by the apparatus but are assigned to the beam pipe. This plot gives an idea how is complicated the geometrical acceptance of LHCb.

  In case of a particle passing through the spectrometer, it can be reconstructed. A decay to be effectively reconstructed implies that all the final state particles are reconstructed. A charged particle is reconstructed if:

  Long tracks share at least 70% of the clusters in the VELO and 70% in the Tracking Stations with the MC Particle;

  Upstream tracks share at least 70% of the clusters in the Tracking Stations with the MC Particle and have no more than 1 different cluster in Trigger Tracker;

  VeloTT tracks share at least 70% of the clusters in the VELO with the MC Particle and

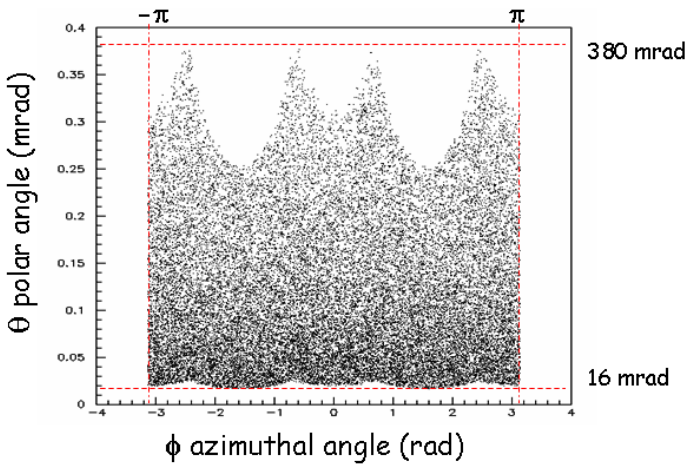

Figure 5.23: Reconstructed muon in the polar θ and azimuthal ϕ angles.

have no more than 1 different cluster in Trigger Tracker.

The reconstruction efficiency has been computed by a specific algorithm which matches MC particles and MC tracks with the reconstructed particles and tracks.
As already mentioned in Sec. 5.4.3, most of the muons decaying from Z^0 are reconstructed as *Long tracks* and show a good χ^2 track-fit (Fig. 5.24).

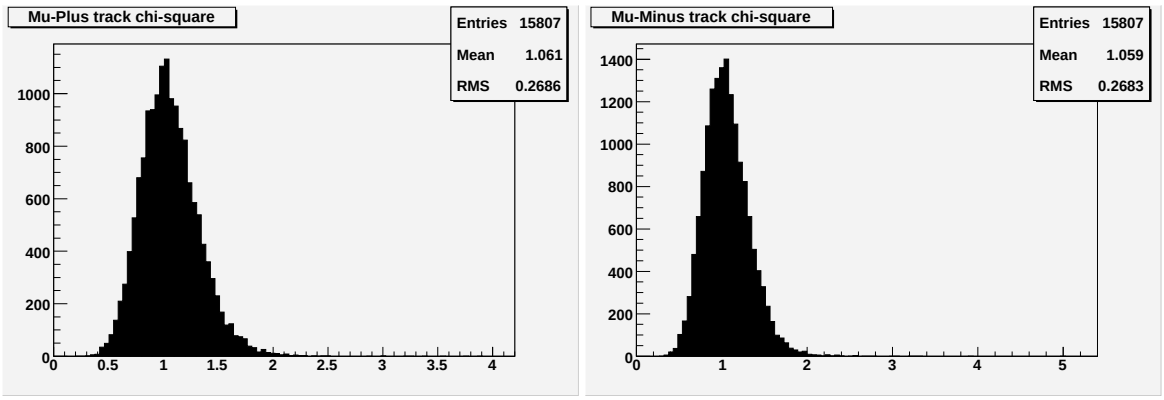

(a) μ^+ tracks.

(b) μ^- tracks.

Figure 5.24: The χ^2 fit of the reconstructed muon tracks.

- selection efficiency (ε_{sel}). The smooth selection cuts have provided a total rejection of the background events leaving almost unchanged the selection efficiency on the signal, which is above 95%.
- L0 trigger efficiency (ε_{L0}). The L0 algorithm selects the 8 highest p_T muons, 2 for each Muon station quadrant. It is hence straightforward for a $Z^0 \rightarrow \mu\mu$ event to pass the L0 trigger filter, as denoted by the very high efficiency.
- L1 trigger efficiency (ε_{L1}). The combination of the *low IP muon* and the pre-existing dimuon J/ψ algorithms allows to increase the L1 efficiency on $Z^0 \rightarrow \mu^+\mu^-$ events up to 80%.
- HLT trigger efficiency (ε_{HLT}). As expected, the HLT efficiency on $Z^0 \rightarrow \mu^+\mu^-$ events is high due to the presence of a dedicated dimuon algorithm in the HLT trigger.

Once both the production cross section and the total efficiency are known, the annual signal yield is final computed as

$$S_{Z\rightarrow\mu\mu} = \mathcal{L}_{int} \times \sigma_Z \times B.R._{Z\rightarrow\mu\mu} \times \varepsilon_{tot}^{\mu\mu} \tag{5.5}$$

where $\mathcal{L}_{int}$ = 2 fb^{-1} is the annual integrated luminosity, assuming 10^7 s as one year of data taking and $\mathcal{L}$ = 2$\times$ 10^{32} cm^{-2}s^{-1} as nominal average luminosity; $\sigma_Z \times BR_{Z^0\rightarrow\mu\mu}$ = 1.86 nb and $\varepsilon_{tot}^{\mu\mu}$ = 14.3%. The final annual yield of $\sim$ 5.3$\times$10^5 events per year means a bandwidth of 53 mHz, or 1 $Z^0 \rightarrow \mu^+\mu^-$ event every 20 s.

The necessary statistics to perform an absolute luminosity measurement, with an error below the theoretical limit of 4%, is $\sim$ 700 $Z^0 \rightarrow \mu^+\mu^-$ events, that means about 3 hours and a half of data taking.

5.5.2 Single muon luminometer

In the *single muon luminometer*, the signal is represented by a muon with high transverse momentum and small impact parameter with respect to the primary vertex. This muon can originate either from a W or from Z^0 with the other muon not reconstructed. The most important background contributes to the signal are summarized in Tab.5.5.

Process	$\sigma \times BR$ (pb)
$W \to \tau\nu_\tau \to \mu\nu_\mu\nu_\tau$	370
$Z^0 \to \tau^+\tau^- \to \mu + X$	10
$t\bar{t} \to W^+bW^-b \to \mu + X$	78
$b\bar{b}$ inclusive	500×10^6

Table 5.5: Cross section for the most important background processes to the signal. The cross section times branching ratio is computed considering only a single muon from the decay. The value should be compared with $\simeq$ 22 nb of the sum of $Z^0 \to \mu^+\mu^-$ and $W \to \mu\nu$ precesses. For the $b\bar{b}$ inclusive events are not included the leptonic branching ratio, while the $t\bar{t}$ production cross section has been evaluated at NNLO [90].

The minimum bias events are not reported as possible background to the signal because the previous study had shown that almost all the muons have been rejected requiring smooth cuts.
The $W \to \tau\nu_\tau \to \mu\nu_\mu\nu_\tau$, $Z^0 \to \tau^+\tau^- \to \mu + X$ and $t\bar{t} \to W^+bW^-b \to \mu + X$ have not been generated yet but their contribution can be estimated. As done in the previous section, a contribution to the signal of about 2% is obtained without selection cuts taking into account the sum of the cross sections times the branching ratios, i.e. $\sim$ 500 pb.

The selection cuts of *single muon luminometer* are sketched in Fig. 5.25 and have been applied to 8×10^6 $b\bar{b}$ inclusive events as background:

1. a muon identification $\Delta \ln \mathcal{L}_{\mu\pi} >$ -2 (Fig. 5.26);
2. a chi-square on the muon track fit $\chi^2 < 2.5$ (Fig. 5.27);
3. a small impact parameter significance with respect to the primary vertex $\mathrm{IP}_\mu/\sigma_{IP} < 3$ (Fig. 5.28);

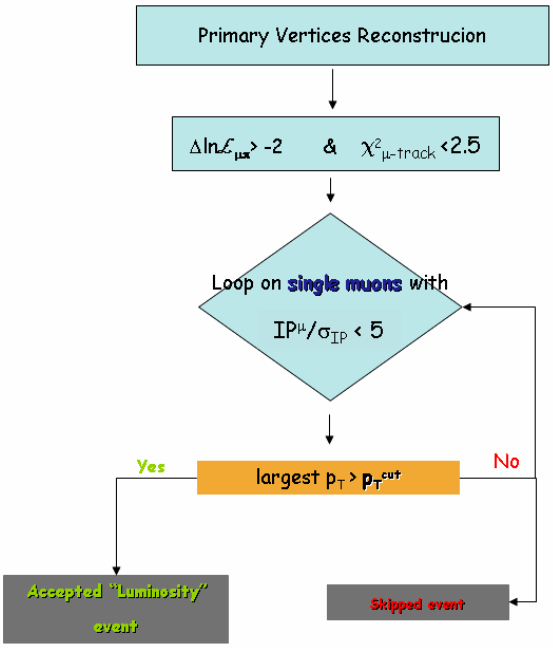

Figure 5.25: Sketch of the selection algorithm applied to a *single muon*.

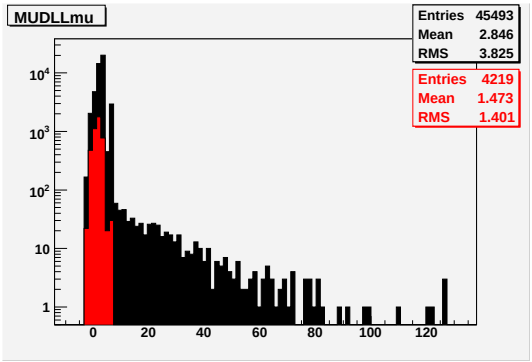

Figure 5.26: $\Delta \ln \mathcal{L}_{\mu\pi}$ distribution for signal (black) and backgrounds (red) events.

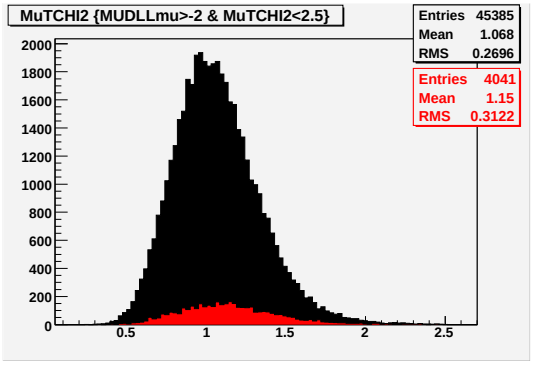

Figure 5.27: Muon track χ^2 for signal (black) and backgrounds (red) events.

After these selection cuts, the background contribution to the signal is not sufficiently reduced, as can be seen in Fig. 5.29 where the transverse momentum of the muons arising from signal and background are shown.
To avoid the background contribute, a suitable p_T cut is needed. Taking into account the cross section, the selection and trigger efficiencies [1] for the two processes, one can compute

[1] Contrarily to the previous measurement, a specific algorithm dedicated to a single muon at the HLT trigger does not exist.

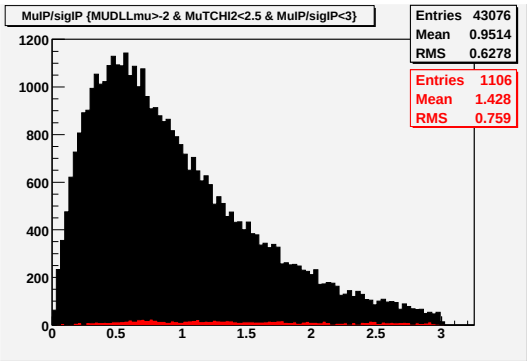

Figure 5.28: Muon impact parameter significance distribution for signal (black) and backgrounds (red) events.

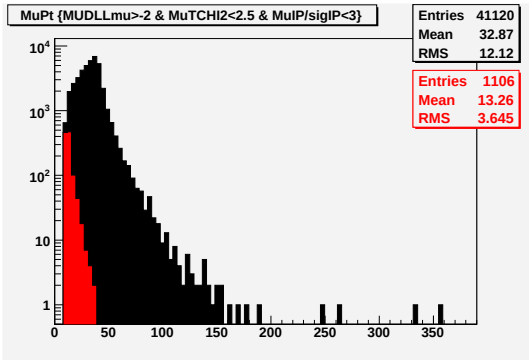

Figure 5.29: Transverse momentum distribution of the signal (black) and background (red).

the signal-background ratio:

$$\frac{S}{B} = \frac{(\sigma \times B.R.)_{1\mu}}{\sigma_b} \cdot \frac{\varepsilon^{1\mu}_{rec/sel/trig}}{\varepsilon^{b}_{rec/sel/trig}}$$

where $(\sigma \times BR)_{1\mu} \simeq 22$ nb, $\sigma_b = 5{\times}10^5$ nb; $55{\times}10^3$ is the total number of events from the $W - Z^0$ and $8{\times}10^6$ is the total number of events from $b\bar{b}$ inclusive sample.
In tab. 5.6 the S/B ratios are summarized as a function of the transverse momentum cut.

	$p_T^\mu > 20$ GeV/c	$p_T^\mu > 25$ GeV/c	$p_T^\mu > 30$ GeV/c	$p_T^\mu > 35$ GeV/c
Selected signal muon	17190	15071	12257	8264
Selected background muon	46	12	1	0
$\varepsilon^{1\mu}_{rec/sel/trig}$ (%)	31.3	27.4	22.3	15.0
$\varepsilon^{b}_{rec/sel/trig}$ (%)	$5.8{\times}10^{-4}$	$1.5{\times}10^{-4}$	$1.3{\times}10^{-5}$	
S/B	2.4	8.0	78.7	

Table 5.6: Signal-background ratios as a function of the transverse momentum cut.

Note that to achieve a systematic uncertainty below the 4%, which corresponds to the inverse of the S/B value, a signal-background ratio of 25 is needed. A conservative p_T cut could be 30 GeV/c.

Selection efficiency

The total signal efficiency on the *single muon luminometer* can be computed as the fraction of signal events that are reconstructed, selected with off-line selection cuts and the triggers. The various efficiencies are discussed in the next and are summarized in Tab. 5.7.

	Number of event	Efficiency (%)	W muons	Efficiency (%)	Z^0 muons	Efficiency (%)
Generated in 4π	3780					
Found in 400 mrad	1090	28.8 ± 0.7				
Generated in 400 mrad	55000		50000		5000	
Reconstruction	46748	85.0 ± 0.2	42488	85.0 ± 0.2	4260	85.2 ± 0.5
Selected	43076	92.1 ± 0.1	39117	92.1 ± 0.1	3959	92.9 ± 0.4
p_T cut > 30 GeV/c	25111	58.3 ± 0.2	22781	58.2 ± 0.2	2330	58.8 ± 0.8
L0 passed	23666	94.2 ± 0.3	21477	94.3 ± 0.2	2184	93.7 ± 0.5
L1 passed	12257	51.8 ± 0.3	11092	51.6 ± 0.3	1165	53 ± 1
HLT passed		95.4 ± 0.2				
Total Efficiency 6.1 $\pm$ 0.8						

Table 5.7: Summary of signal efficiency for the *single muon luminometer*. It also reported for each efficiency, the number of muons coming from W and Z^0. The error of the various efficiency is statistical, while the error of the total efficiency is compute as squared sum in order to take into account the generation and HLT efficiencies.

- generation efficiency (ε_{gen}). Since the kinematics of the Z^0 and W processes are similar and the two decaying leptons have polar angles highly correlated, the generation efficiency of the *single muon luminometer* has been considered the same of the $Z^0 \rightarrow \mu^+\mu^-$ process. However, the real generation efficiency of such processes will be evaluated with future studies;
- reconstruction efficiency (ε_{rec}). This includes the geometrical efficiency as well. Since only one muon per event is expected, the efficiency is grater than that obtained with *dimuon luminometer*. Note that a full efficiency is not reached due to the effective geometrical acceptance of the LHCb apparatus.
- selection efficiency (ε_{sel}). The tight cuts, before the p_T cut, allow to reduce the $b\bar{b}$ inclusive background, leaving the selection efficiency on the signal above 90%. On the other hand, the p_T cut reduces this efficiency down to 50% but allows to reach a systematic uncertainty below 4%, i.e. S/B > 25. Note that the selection cuts do not favour a muon decaying from the W with respect to that decaying from the Z^0.

- L0 trigger efficiency (ε_{L0}). As expected, it is straightforward for these events to pass the L0 trigger filter and the resulting efficiency is comparable to that found with the *dimuon luminometer*. Once again, the ratio between muons decaying from the W and from the Z^0 remains unchanged after the L0 trigger;
- L1 trigger efficiency (ε_{L1}). This efficiency is relatively lower than that obtained with the *dimuon luminometer*. The reason is that for a dimuon event two specific algorithms are available, while only one is available for the single muon. Therefore, when only a Z^0 muon is reconstructed, the L1 trigger does not favour the Z^0 decay with respect to W one.
- HLT trigger efficiency (ε_{HLT}). Since no specific algorithm exits for such kind of events, the HLT efficiency is kept equal to that obtained with the *dimuon luminometer* in order to compare the corresponding total efficiencies.

Finally, we can compute the annual signal yield of this luminosity measurement:

$$S_{1\mu} = \mathcal{L}_{int} \times (\sigma \times B.R.)_{1\mu} \times \varepsilon_{tot}^{1\mu} \tag{5.6}$$

where $\mathcal{L}_{int}$ = 2 fb^{-1} is the annual integrated luminosity, $(\sigma \times B.R.)_{1\mu}$ = 22.13 nb and $\varepsilon_{tot}^{1\mu}$ = 6.1%.
The final annual yield of $\sim 2.7\times10^6$ events per year means a bandwidth of 270 mHz, or 1 single muon decaying from Z^0 or W every 4 s.
In order to collect $\sim$ 700 events less than 1 hour of data taking is necessary.

The study of the $b\bar{b}$ inclusive events, as background source to the *single muon luminometer* signal, allows to determine the needed bandwidth for the *low IP muon* algorithm within L1 trigger. The necessary bandwidth can be computed looking at the muons coming from the $b\bar{b}$ inclusive events which pass L0&L1 filters without any selection cuts. The number of $b\bar{b}$ events is about 3×10^3, leading to an efficiency of $\sim 4\times10^{-2}$. Considering the above integrated luminosity and the $b\bar{b}$ cross section, a bandwidth of about 40 Hz is obtained. This value is obviously negligible with respect to the L1 single muon bandwidth ($\sim$ 9 kHz) and therefore the *low IP muon* algorithm could be included in the L1 trigger.

5.6 Conclusions

The *dimuon* and the *single muon* luminometers studies have demonstrated the possibility to perform luminosity measurements in few hours at the LHCb experiment with a good accuracy.
700 events allow to obtain a statistical error below the 4%, comparable with the theoretical uncertainty. This amount is collected in about four and one hours of data taking respectively for the *dimuon* and the *single muon* luminometers.
The error due to not considered background sources can be estimated to be at most 0.5% and 2% respectively for the two methods. However it needs further studies on copious samples.
Currently, the estimated total uncertainty, computed as the squared sum of the above errors, is anyway less than 8% for both the methods.

The addition of the new specific algorithm, *low IP muon*, has shown that a good efficiency can be achieved in L1 filter even for processes outside the main physics program of the experiment. In fact the *low IP muon* has allowed to reach a L1 efficiency up to 80%, comparable to that obtained with other dimuon processes, such as the $B_s^0 \rightarrow J/\psi(\mu^+\mu^-)\Phi$.
The needed bandwidth for this algorithm results to be negligible with respect to total streaming bandwidth and others developments can be performed.
Certainly the definition of a specific algorithm in the HLT trigger, which looks for muons coming from the Z^0 and W massive bosons, will be one of the future works.

Conclusions

The work of this thesis concerned both the development of a triple-GEM detector for the LHCb muon system and the study of luminosity measurements through the decay of the Z^0 and $W^{\pm}$ bosons into muon channels.

The triple-GEM detectors will equip the innermost and forward region (M1R1) of Muon system, where a harsh environment around the beam pipe does not allow the use of the Multi Wire Proportional Chambers.
The requirements for detectors in M1R1 are:

- a particle rate capability up to $\sim$ 500 kHz/cm^2;
- each station, made up of two independent detector layers logically OR-ed pad by pad, must have an efficiency in 20 ns time window higher than 96%;
- a pad cluster size, i.e. the number of adjacent detectors pads fired when a track crosses the detector, should not be larger than 1.2 for 10×25 cm^2 pad size;
- the detector must tolerate, without damages or large performance losses, an integrated charge of $\sim$ 1.8 C/cm^2 in 10 years of operation at a gain of $\sim$ 6000 and an average particle flux of 184 kHz/cm^2 for an average machine luminosity of 2×10^{32} cm^{-2}s^{-1}.

Three years of R&D activity, performed with a triple-GEM prototype of 10×10 cm^2 active area, have spent to optimize the GEM detectors in term of time performance and efficiency as well as the discharge probability per incident particle. Very interesting and unique results have been obtained: rate capability is well above 50 MHz/cm^2; time resolutions better than 5 ns are achieved with fast and high yield CF_4 and iso-C_4H_{10} based gas mixtures, considerably improving the results obtained in the past with the standard Ar/CO_2 (70/30) gas mixture ($\sim$ 10 ns).

With such fast gas mixtures, an efficiency in 20 ns time window above the 96% is achieved by our detector station.
The results with the high intensity pion/proton beams at PSI and the local X-ray irradiation have shown that the triple-GEM detector is very robust and able to tolerate more than 10 years of operation at LHCb without damages or large performance losses.
The full size detector, with an active area of 20×24 cm^2, has been extensively and successfully tested at the T11-PS CERN facility, confirming the results obtained in the R&D phase.
The large irradiation test, performed with a high intensity 1.25 MeV γ from a ^{60}Co source, have shown that even after a severe irradiation in very bad conditions, the detectors still exhibit good performances.
Moreover these tests gave us useful informations to qualify the materials used for the detector construction, allowing to finalize the detector design and its construction procedures together with the definition of quality checks.
The construction of the twenty-four triple-GEM detectors has been started and it will be completed in summer 2006. The installation of the detectors is foreseen by the end of 2006.

In the second part of the thesis the processes $pp \rightarrow Z^0 \rightarrow \mu^+\mu^-$ and $pp \rightarrow W \rightarrow \mu\nu$ have been studied in order to perform an absolute luminosity measurements. The theoretical cross-sections for these processes have recently been calculated at Next to Next Leading Order (NNLO), and at LHC energy (14 TeV) are foreseen to be $\sigma_Z \simeq 56$ nb and $\sigma_W \simeq 190$ nb.
Despite of the limited angular acceptance and the optimization for the B-physics of the LHCb experiment, these cross-sections are sufficiently high to detect a large number of $Z^0 \rightarrow \mu^+\mu^-$ and $W \rightarrow \mu\nu$ events enabling to perform luminosity measurements with a high accuracy.
Large samples of events, 25000 of $Z^0 \rightarrow \mu^+\mu^-$ and 50000 of $W \rightarrow \mu\nu$, have been generated and the detection efficiency of the apparatus have been extensively simulated, including the reconstruction, the off-line and the trigger selections.
Background sources have been also included in the analysis in order to determine their effects on the signal. The high transverse momentum and the low impact parameter of the muons decaying from Z^0 and W bosons allow to provide a clear selection strategy ensuring a good efficiency in the rejection of the background processes.
In conclusion, the two studies have demonstrated the possibility to perform luminosity measurements in few hours of data taking at the LHCb experiment with an accuracy of $\sim 8\%$, including statistics, systematics and theoretical uncertainty.

Conclusions

Bibliography

[1] The LHC Study Group., ”The Large Hadron Collider, Conceptual Design”, CERN/AC/95-05 (LHC).

[2] P. Nason *et al.*, Bottom production. In Proceedings of the 1999 Workshop on Standard Model Physics at the LHC, volume CERN 2000-04. CERN, 1999, hep-ph/0003142.

[3] LHCb collaboration, ”LHCb Technical Proposal”, CERN/LHCC 04 (1998).

[4] LHCb collaboration, ”LHCb Reoptimized Detector Design Report”, CERN/LHCC 030 (2003).

[5] LHCb collaboration, ”LHCb VELO Technical Design Report”, CERN/LHCC 011 (2001).

[6] LHCb collaboration, ”LHCb RICH Technical Design Report”, CERN/LHCC 037 (2000).

[7] LHCb collaboration, ”LHCb Magnet Technical Design Report”, CERN/LHCC 007 (2000).

[8] LHCb collaboration, ”LHCb Inner Tracker Technical Design Report”, CERN/LHCC 029 (2002).

[9] LHCb collaboration, ”LHCb Outer Tracker Technical Design Report”, CERN/LHCC 026 (2001).

[10] LHCb collaboration, ”LHCb Calorimiters Technical Design Report”, CERN/LHCC 036 (2000).

[11] LHCb collaboration, ”LHCb Muon System Technical Design Report”, CERN/LHCC 010 (2001).

[12] LHCb collaboration, ”LHCb Trigger System Technical Design Report”, CERN/LHCC 010 (2003).

[13] E. Rodrigues, ”Level-0 Trigger Bandwith Decision”, LHCb note 048 (2003).

[14] C. Jacoby and T.Schietinger, ”Level-1 decision algorithm and bandwith division”, LHCb note 111 (2003).

[15] P. Koppernburg and L. Fernandez, ”HLT Exclusive Selections Design and Implementation”, LHCb note 011 (2005).

[16] M. Battaglia *et al.*, ”The CKM matrix and the Unitary Triangle”, hep-hp/0303132.

[17] UTFIT Home page, www.utfit.org.

[18] ATLAS muon collaboration, “ATLAS muon spectrometer, Technical Design Report”, CERN/LHCC 97–22.

[19] CMS muon collaboration, ”CMS The muon project, Technical Design Report”, CERN/LHCC 97–32.

[20] A. Ali, Nucl. Instr. and Meth. **A 384** (1996) 8.

[21] N. Harnew, ”B Physics at the LHC”, Frascati Physics Series Vol. XXXI 289 (2003).

[22] C. Zeitnitz and T.A. Gabriel, The Geant-Calor interface User’s Guide (1999), `http://www.physik.uni-mainz.de/zeitnitz/gcalor/gcalor.html`

[23] I. Azhgirey, I. Kurochkin and V. Talanov, “Development of MARS Code Package for Radiation Problems Solution of Electro-Nuclear Installation Design”, in: Proc. of XV Conference on Charged Particles Accelerators, Protvino, October 22–24 (1996)

[24] N. Saguidova *et al.*, “GCALOR Studies of Backgrond in the LHCb Muon chambers”, LHCb 1998-059 Expt;
A. Tsaregorodtsev, “Muon System parameterised background – algorithm and implementation”, LHCb 2000–011 Muon.

[25] P. Colrain, “Upgrade of the Muon System background parameterisation”, LHCb 2001–029 Muon.

[26] LHCb collaboration, ”Addendum to the LHCb Muon System Techical Design Report”, CERN/LHCC 002 (2003).

[27] LHCb collaboration, ”Second Addendum to Muon System Technical Design Report”, CERN/LHCC 012 (2005).

[28] M. Anelli *et al.*, ”Test of MWPC prototypes for Region 3 of Station 3 of the LHCb Muon System”, LHCb 2004-74 Muon.

[29] M. Anelli *et al.*, ”Aging test of a prototype for the region 3 of the LHCb muon system”, LHCb 2003–040 Muon.

[30] J. Christiansen, ”Requirements for the L0 front-end electronics”, LHCb 1999-029 Trigger.

[31] W. Bonivento *et al.*, Nucl. Instr. and Meth. **A 491** (2002) 233.
The main characteristic of the CARIOCA chip can be found in: http://www.cern.ch/riegler/.

[32] G. Charpak *et al.*, Nucl. Instr. and Meth. **A 62** (1968) 262.

[33] F. Sauli, ”Principle of operation of multiwire proportional and drift chamber”, Yellow Report, CERN 77-09, 1977.

[34] A. Oed *et al.*, Nucl. Instr. and Meth. **A 263** (1988) 351.

[35] F. Angelini *et al.*, Nucl. Instr. and Meth. **A 283** (1989) 755.

[36] F. Angelini *et al.*, Nucl. Instr. and Meth. **A 382** (1996) 461.

[37] R. Bouclier *et al.*, Nucl. Instr. and Meth. **A 369** (1996) 328.

[38] R. Bouclier *et al.*, Nucl. Instr. and Meth. **A 381** (1996) 289.

[39] F. Angelini *et al.*, Nucl. Instr. and Meth. **A 335** (1993) 69.

[40] S. Biagi et al., Nucl. Instr. and Meth. **A 361** (1995) 72.

[41] F. Bartol *et al.*, J. Phys. III France 6 (1996) 337.

[42] I. Giomataris *et al.*, Nucl. Instr. and Meth. **A 376** (1996) 29.

[43] R. Bellazzini *et al.*, Nucl. Instr. and Meth. **A 424** (1999) 444.

[44] R. Bellazzini *et al.*, Nucl. Instr. and Meth. **A 423** (1999) 125.

[45] F. Sauli, Nucl. Instr. and Meth. **A 386** (1987) 531.

[46] A. Breessan *et al.*, Nucl. Instr. and Meth. **A 425** (1999) 262.

[47] J. Benlloch *et al.*, Nucl. Instr. and Meth. **A 419** (1998) 410.

[48] A. Gandi,*Laboratory of Photomechanical Technique and Printed Circuites*, EST-SM-CI Section, CERN, Geneva, Switzerland.

[49] M. Inuzuka *et al.*, Nucl. Instr. and Meth. **A 525** (2004) 529.

[50] J. Benlloch *et al.*, *"Development of the Gas Electron Multiplier (GEM)"*, CERN-PPE/97-146.

[51] S. Bachmann *et al.*, Nucl. Instr. and Meth. **A 438** (1999) 376.

[52] Maxwell 3D Field Smulator. User's refence. Ansoft Corporation.

[53] R. Veenhof, Nucl. Instr. and Meth. **A 419** (1998) 726.

[54] C. Richter *et al.*, Nucl. Instrum.Meth. **A 461** (2001) 38.

[55] J. Townsend, *"Electron in gases"*, Hutchinson, Londra 1947.

[56] G. Bencivenni *et al.*, Nucl. Instrum.Meth. **A 488** (2002) 493.

[57] M. Poli Lener Degree Thesis, "Studio e sviluppo di un rivelatore a GEM per la zona centrale delle camere a muoni di LHCb", (2002).
www.lnf.infn.it/esperimenti/thes/tesipoli.pdf

[58] G. Bencivenni *et al.*, Nucl.Instrum.Meth. **A 494** (2002) 156.

[59] D. Pinci PhD. Thesis, "A triple-GEM detector for the muon system of the LHCb experiment", (2002).

[60] R.J. Yarema *et al.*, IEEE Trans. Nucl. Sci. **NS-39** (1992) 742.

[61] B. Ketzer *et al.*,J.*"Triple GEM Tracking Detectors for COMPASS"*, submitt to IEEE Transactions on Nuclear Scienze.

[62] S. Ramo, "Currents induced in electron motion", Proc. IRE 27 (1934) 584.

[63] G. F. Knoll, ”Radiation detection and measuremt”, John Wiley and Sons (1989).

[64] A. Alfonsi *et al.*, Nucl.Instrum.Meth. **A 518** (2004) 106.

[65] S. Backmann *et al.*, Nucl.Instrum.Meth. **A 479** (2002) 294.

[66] H. Raether, ”Electron Avalanches and Breakdown in Gases”, Butterworth, London (1964).

[67] F.E. Taylor, Nucl. Instrum. Meth. **A289** (1989) 283.

[68] F. Sauli, Nucl. Instrum. Meth. **A 515** (2003) 249.

[69] M. Hohlmann *et al.*, Nucl. Instrum. Meth. **A 494** (2002) 179.

[70] C. Altunbas *et al.*, Nucl. Instrum. Meth. **A 490** (2002) 177.

[71] E. Amaldi, R. Bizzari, G. Pizzella, ”Fisica Generale”, Zanichelli editore (1995).

[72] R.O. Ritchie, ”Mechanical Behavior of Materilas Lecture Notes ”, University of California, Berkeley, Fall 1993.

[73] A. Alfonsi *et al.*, presented at Puerto Rico 2005 IEEE conference (Oct. 23-29) and submitted to Transaction on Nuclear Science.

[74] TOTEM Collaboration, Technical Proposal, CERN/LHCC/99-7.

[75] K.Piotrzkowski, ATLAS Physics Note ATL-PHYS-96-077 (1996).

[76] A. Maslennikov, ”Photon Physics in Novosibirsk”, Workshop on Photon Interactions and Photon Structure, Lund (1998) 347.

[77] V.A. Khoze *et al.*, Eur. Phys. J. **C19** (2001) 313.

[78] P.D.B. Collins & A.D. Martin, ”Hadron Interaction” ADAM HILGER LTD, BRISTOL.

[79] V. Martin, ”Inclusive W and Z cross section measurements at the Fermilab Tevatron”, submitted to Internationl Journal of Modern Physics A (2004).

[80] T. Doringo, ”W and Z Cross Sections at the Tevatron”, hep-ex/0306008 (2003).

[81] W.J. Stirling *et al.*, Eur. Phys. J. **C18** (2000) 117.

[82] W.J. Stirling *et al.*, Eur. Phys. J. **C14** (2000) 133.

[83] W.L. van Neerven and A. Vogt, Nucl. Phys. **B382** (2000) 11.

[84] G.Barrand *et al.*, "Gaudi - a software architecture and framework for building HEP data processing applications", Comp. Phys. Comm. 140 (2001).

[85] T. Sjostrand *et al.*, "High Energy physics event generation with Pythia", Comp. Phys. Comm., 135 (2001) 238.

[86] S. Agostinelli *et al.*, Nucl. Inst. Meth. **A 506** (203) 250.

[87] H.Plothow Besch, Computer Physics Commun.75 (1993)396, Int. J. Mod. Phys. **A10** (1995) 2901, http://consult.cern.ch/writeup/pdflib/

[88] M. Poli Lener, "Luminosity measurements with Z^0 and W decays into muons", presented at production and decay WG, June 30 (2005).
https://uimon.cern.ch/twiki/bin/view/LHCb/LuminosityMeasurements

[89] T. Schietinger, "L1 efficiencies and Plans", presented at the LHCb trigger meeting, October (2004).
http://agenda.cern.ch/askArchive.php?base=agenda&categ=a044522&id=a044522s1t0/transparencies.

[90] N. Kidonanakis *et al.*, "Theoretical status of the top quark cross section", (2004) hep-ph/0410367

[91] Review of Particle Physics 2004

Ringraziamenti

Primi fra tutti ringrazio la mia famiglia, babbo, mamma e Claudia, per la serenetità e la tranquilità che mi hanno trasmesso in questi ultimi anni e soprattutto durante il periodo snervante della stesura di questa tesi.

Ringrazio tutto il gruppone di S. Giovanni: Eli e l' "albanese" (Laura), Paolo & Mary, Simona, Matteo, Tommy, Andrea, "i ciccioni" (Leo & Fra), Rodolfo, Giovanni & Francesca, Cristina, Giuditta, Noemi, le inseparabili Miriam & Debora, Marco, Emanuele e Luca, ecc.

Infine ho l' obbligo morale di ringraziare le persone con cui lavoro: il mio relatore, Gianni, perchè ha fatto una faticaccia enorme a correggere l' inglese di questa benedetta tesi, perchè rileggiendola si è comportato come la celebre scena dell' avvocato interpretato da Giggi Proietti, e infine perchè nei momenti più buii mi ha sempre ricordato che ero in "ritardo" su tutto.
Poi Matteo per le illuminanti discussioni fatte in ufficio ed ai pubs di Barcellona. Lo ringrazio per l' aiuto che mi ha dato nella prima fase degli studi di simulazione e per avermi insegnato ad usare ROOT.
Ringrazio Patty, Danilo, Marco, Fabrizio e Chiara per i consigli e l' approfondimento di alcune delle parti di questa tesi. Poi sono grato alla "Totta" (Flavia) e a "ciosbetta" (Silvia) sempre pronte a fare dei break dal lavoro. E quindi il gruppo delle camere a fili, Giulietto, Davide, Emiliano, Carlo & Gaia e Alessio. Quest' ultimo è stato fondamentale nella fase iniziale del mio lavoro di simulazione.

Non posso non ringraziare tutti coloro che mi hanno dato un grandissimo aiuto nell' ultimo capitolo di questa tesi: Vincenzo, che con i suoi suggerimenti e chiarimenti mi ha permesso di comprendere la fisica di LHC, ed Angelo per il tempo speso a trasferire tutti i

file che richiedevo. Poi Marco, Thomas e Gloria per i controlli e i consigli nella scrittura del codice dell’ analisi.